

**A CURE PROCESS MODEL FOR RESIN TRANSFER MOLDING  
OF ADVANCED COMPOSITES**

by

Steven J. Claus

Thesis submitted to the Faculty of the  
Virginia Polytechnic Institute and State University  
in partial fulfillment of the requirements for the degree of  
Master of Science  
in  
Engineering Mechanics

APPROVED:

Alfred C. Loos, Chairman

Hayden Griffin Jr.

Thangavelu Kuppusamy

April 14, 1989

Blacksburg, Virginia

**A CURE PROCESS MODEL FOR RESIN TRANSFER MOLDING  
OF ADVANCED COMPOSITES**

by

Steven J. Claus

Alfred C. Loos, Chairman

Engineering Science and Mechanics

(ABSTRACT)

The resin transfer molding (RTM) process has been identified as a cost-effective fabrication technique for producing composite materials from geometrically complex reinforcements. Processing models can be used to determine the temperature and pressure cycles which will produce a finished part with the best properties in the shortest time. This work involved the development and verification of a processing model for RTM.

The processing model is based on the assumption that infiltration can be described as flow through a porous medium. Flow through porous media, as governed by D'Arcy's law, depends on the viscosity of the fluid and the microstructure of the interconnected pores. Infiltration by thermosetting resin systems is assumed to behave as a Newtonian fluid with a time and temperature dependent viscosity. The kinetics of the resin can be described by mathematical expressions determined from standard thermal analysis techniques. The reinforcement is assumed to be a homogenous, anisotropic material which exhibits strain stiffening, hysteresis and plastic deformation. D'Arcy's law describes the porous material in terms of the material permeability. Kozeny-Carman's relationship is used to relate the porosity to the permeability. Solution of D'Arcy's law is accomplished in a quasi-steady state manner by an evolving mesh finite element technique.

After infiltration is completed, the model continues to predict the temperature, degree of cure and viscosity of the resin. The equations governing the unsteady heat transfer are solved with an existing cure model by the finite difference method. Results of the processing model include estimates of infiltration, gel and cure times as well as the cured thickness and fiber volume fraction. Test laminates were fabricated, mechanically tested, and compared to prepegged laminate results. Construction of one of the test laminates was simulated with the processing model to verify the accuracy of the simulation.

## Acknowledgements

The author would like to express his gratitude to Professor A. C. Loos for his guidance and encouragement throughout the course of this research and thesis. He would also like to thank Professors O. H. Griffin and T. Kuppusamy for their advice in the numerical implementation. This work was supported by the NASA-Virginia Tech Composites Program through grant number NAG1-343. The author wishes to express his thanks to [redacted] for his support and encouragement during his residency at NASA-Langley; to Dr. E. Long and [redacted] for their support; and to the Engineering Science and Mechanics students for their encouragement and fruitful discussions.

# Table of Contents

<b>1.0 INTRODUCTION .....</b>	<b>1</b>
<b>2.0 LITERATURE REVIEW .....</b>	<b>5</b>
<b>2.1 INFILTRATION .....</b>	<b>5</b>
<b>2.1.1 Flow .....</b>	<b>6</b>
<b>2.1.2 Compaction .....</b>	<b>7</b>
<b>2.1.3 Porosity-Permeability .....</b>	<b>13</b>
<b>2.2 CURE .....</b>	<b>15</b>
<b>3.0 INFILTRATION MODEL .....</b>	<b>17</b>
<b>3.1 FLOW SUB-MODEL .....</b>	<b>18</b>
<b>3.2 DEFORMATION SUB-MODEL .....</b>	<b>24</b>
<b>3.2.1 Compaction .....</b>	<b>27</b>
<b>3.2.2 Porosity .....</b>	<b>29</b>
<b>3.2.3 Permeability .....</b>	<b>31</b>
<b>4.0 CURE MODEL .....</b>	<b>34</b>

4.1 HEAT TRANSFER SUB-MODEL .....	35
4.2 KINETICS SUB-MODEL .....	38
4.3 VISCOSITY SUB-MODEL .....	40
<b>5.0 NUMERICAL SOLUTION PROCEDURES .....</b>	<b>42</b>
5.1 GOVERNING EQUATIONS .....	43
5.2 INITIAL AND BOUNDARY CONDITIONS .....	45
5.3 FINITE ELEMENT FORMULATION .....	49
5.4 FINITE DIFFERENCE FORMULATION .....	56
5.5 COMPUTER PROGRAM INFIL .....	61
<b>6.0 EXPERIMENTAL METHODS .....</b>	<b>64</b>
6.1 MATERIALS .....	64
6.2 COMPACTION EXPERIMENTS .....	67
6.2.1 Test Equipment .....	67
6.2.2 Sample Preparation .....	70
6.2.3 Procedure .....	70
6.2.4 Data Analysis .....	72
6.2.5 Wet Compaction .....	73
6.3 PERMEABILITY EXPERIMENTS .....	74
6.3.1 Test Equipment .....	74
6.3.2 Sample Preparation .....	76
6.3.3 Procedure .....	76
6.3.4 Data Analysis .....	78
6.3.5 In-Plane Permeability .....	81
6.4 MECHANICAL PROPERTIES .....	81
6.4.1 Test Equipment .....	83
6.4.2 Sample Preparation .....	83

6.4.3	Testing Procedures .....	88
6.4.4	Data Analysis .....	88
<b>7.0</b>	<b>EXPERIMENTAL RESULTS AND DISCUSSION .....</b>	<b>89</b>
7.1	COMPACTION .....	90
7.1.1	Dry Compaction Preliminaries .....	90
7.1.2	Dry Compaction .....	92
7.1.3	Wet Compaction .....	100
7.2	PERMEABILITY .....	106
7.2.1	Experiment Preliminaries .....	109
7.2.2	Transverse Permeability Results .....	111
7.2.3	Transverse Permeability Verification .....	116
7.2.4	In-Plane Permeability Results .....	118
7.2.5	In-Plane Permeability Verification .....	120
7.3	MECHANICAL CHARACTERIZATION .....	124
7.3.1	Nondestructive Evaluation .....	125
7.3.2	Volume Fraction Determination .....	134
7.3.3	Porosity Model Verification .....	136
7.3.4	Mechanical Characterization Results .....	136
<b>8.0</b>	<b>RTM PROCESS SIMULATION .....</b>	<b>149</b>
8.1	PARAMETRIC STUDY: AUTOCLAVE PRESSURE .....	150
8.2	PARAMETRIC STUDY: ISOTHERMAL INFILTRATION .....	152
8.3	PARAMETRIC STUDY: HEATING RATE .....	157
8.4	THICK LAMINATE STUDY .....	160
8.5	MODEL VERIFICATION .....	163
<b>9.0</b>	<b>CONCLUSIONS AND FUTURE WORK .....</b>	<b>168</b>

9.1 CONCLUSIONS .....	168
9.2 FUTURE WORK .....	170
10.0 BIBLIOGRAPHY .....	171

# List of Illustrations

Figure 1.	Gutowski, Kingery and Boucher [5] representative volume element for fiber deformation. ....	9
Figure 2.	Deformation of a dry porous material with impermeable boundaries. ....	19
Figure 3.	Deformation and flow of a partially saturated porous material with impermeable boundaries. ....	20
Figure 4.	Aligned flow through a system of aligned fibers. ....	25
Figure 5.	General flow through a system of aligned fibers. ....	26
Figure 6.	Vacuum bag schematic used to model heat transfer during RTM. ....	36
Figure 7.	Vacuum bag schematic for discussion of the boundary conditions. ....	47
Figure 8.	Eight-node quadrilateral element with the Gaussian integration points and the local nodal numbering scheme. ....	53
Figure 9.	Logic diagram for the quasi-steady state infiltration process. ....	55
Figure 10.	Finite difference grid for numerical solution of the heat transfer problem. ....	57
Figure 11.	Logic diagram for computer program INFIL. ....	63
Figure 12.	Schematic representation of the test fixture used for the compaction experiments. ....	68
Figure 13.	Test fixture mounted in the Instron model 1321 multi-axis testing machine. ....	69
Figure 14.	Fabric geometry and directions used for sample preparation. ....	71
Figure 15.	Cross-sectional view of the test fixture configured for through-the-thickness permeability experiments. ....	75
Figure 16.	Plumbing schematic of equipment used for the permeability tests. ....	77

Figure 17. Test fixture configured for the in-plane permeability tests. ....	82
Figure 18. Typical vacuum bag infiltration schematic for production of cured laminates. ....	85
Figure 19. Cutting Diagram for the cured laminates. ....	87
Figure 20. Experimental fixture data and Equation 7.1.1. ....	93
Figure 21. First load cycle of five plies of C3k/8HS fabric and the test fixture. ....	94
Figure 22. Effect of the fixture on the first loading cycle of C3k/8HS. ....	95
Figure 23. First loading cycle of adjusted, five ply, C3k/8HS data with Equation 7.1.2. ....	97
Figure 24. Variation between five ply specimens of C3k/8HS and mean response. .	98
Figure 25. Initial loading curves of multi-ply specimens. ....	99
Figure 26. Normalized initial loading curves for multi-ply specimens. ....	101
Figure 27. Normalized, four cycle behavior of IM7/8HS fabric. ....	104
Figure 28. Compaction characteristics of the first three compaction cycles of wet IM7/8HS fabric. ....	107
Figure 29. Comparison of wet and dry compaction behavior of the IM7/8HS fabric. ....	108
Figure 30. Flow meter calibration data and Equation 6.3.1. ....	110
Figure 31. Selected flow data for the empty fixture and Equation 7.2.1. ....	112
Figure 32. Experimental data and Equation 6.3.7 for IM7/8HS fabric sample Number 3. ....	113
Figure 33. Measured through-the-thickness permeability of five plies of IM7/8HS fabric. ....	115
Figure 34. Through-the-thickness permeability comparison with literature values. ....	117
Figure 35. Through-the-thickness fabric permeabilities and the Kozeny-Carman model. ....	119
Figure 36. In-Plane flow data and Equation 6.3.7 for sample Number 2. ....	121
Figure 37. In-Plane permeability comparison with literature values. ....	122
Figure 38. Schematic of gap in fixture. ....	123

Figure 39. Ultrasonic, gray-scale C-scan of Laminate 4228. . . . .	126
Figure 40. Photomicrograph of Laminate 4228 (10.6 X). . . . .	127
Figure 41. Ultrasonic, gray-scale C-scan of Laminate 4268. . . . .	128
Figure 42. Photomicrograph of Laminate 4268 (9.4 X). . . . .	129
Figure 43. Ultrasonic, gray-scale C-scan of Laminate 5118. . . . .	131
Figure 44. Photomicrograph of Laminate 5118 (8.8 X). . . . .	132
Figure 45. Photomicrograph of Laminate 5238 (14.9 X). . . . .	133
Figure 46. Pressure-porosity model verification. . . . .	137
Figure 47. Elastic modulus for tensile loading. . . . .	140
Figure 48. Ultimate tensile stress. . . . .	142
Figure 49. Ultimate tensile strain. . . . .	143
Figure 50. Elastic modulus for compressive loading. . . . .	145
Figure 51. Ultimate compressive stress. . . . .	147
Figure 52. Ultimate compressive strain. . . . .	148
Figure 53. Selected infiltration profiles used for the pressure parametric study. . . . .	151
Figure 54. Results from the pressure parametric study. . . . .	154
Figure 55. Selected infiltration profiles used for the isothermal infiltration parametric study. . . . .	155
Figure 56. Results from the isothermal temperature parametric study. . . . .	158
Figure 57. Selected infiltration profiles used for the heating rate parametric study. . . . .	159
Figure 58. Results from the heating rate parametric study. . . . .	162
Figure 59. Infiltration profile for the simulation of Laminate 4268. . . . .	165
Figure 60. Temperature, viscosity and degree of cure profiles for the simulation of Laminate 4268. . . . .	166

# List of Tables

Table 1. Fabric Properties. . . . .	66
Table 2. Dry Compression Test Matrix. . . . .	91
Table 3. Normalized Compaction Coefficients for Dry C3k/8HS Fabric. . . . .	102
Table 4. Normalized Compaction Coefficients for Dry IM7/8HS Fabric. . . . .	103
Table 5. Normalized Compaction Coefficients for Wet IM7/8HS Fabric. . . . .	105
Table 6. Volume Fraction of Cured Laminates. . . . .	135
Table 7. Mechanical Test Results - Tension . . . . .	139
Table 8. Mechanical Test Results - Compression . . . . .	144
Table 9. Selected Results from the Pressure Parametric Study. . . . .	153
Table 10. Selected Results from the Isothermal Infiltration Parametric Study. . . .	156
Table 11. Selected Results from the Heating Rate Parametric Study. . . . .	161
Table 12. Selected Results from the Thick Laminate Parametric Study. . . . .	164
Table 13. RTM Processing Model Verification Study. . . . .	167

# **1.0 INTRODUCTION**

The use of composite materials in the aerospace and transportation industries has grown quickly in the last decade. Along with this growth has been an increase in the problems associated with implementing these materials into new and existing designs in a cost effective manner. The most common method of manufacturing composite structures is to use aligned fiber systems which have been preimpregnated with a thermosetting epoxy resin (prepreg). New materials are being developed to replace unidirectional prepregs in order to exploit the unique multi-directional characteristics of woven, knitted, and braided textile preforms. These materials offer additional advantages over aligned fiber systems for their adaptability to automated production and materials handling.

The manufacture of aligned fiber prepreg begins with untwisted bundles of filaments called tows. The tows are fed through a device which separates and collimates the fibers. The fibers are then dipped into a bath of resin at elevated temperature. Spreading the tows allows the resin to completely penetrate and wet the filaments. Often the tows travel through a series of rollers in the resin bath to aid in impregnation and to remove any trapped air. As the fibers are pulled out of the resin, a final set of rollers removes

excess resin and consolidates the material. The wet material is applied to a sheet of backing paper and allowed to cool. The material is generally stored in this form until just before the final construction of the composite laminate.

Individual prepreg plies are cut from the unidirectional sheets, and placed in a specified orientation (laid-up) by hand. If a part with complex geometry is desired, the plies are often placed directly onto the tooling. The material is then cured in an autoclave, or a matched metal mold, by applying elevated temperature and pressure. After two to six hours, the part is removed from the tooling for final machining and assembly.

Three major disadvantages exist for this method of composite manufacture; prepreg storage requires an environment which is cool and dry, large amounts of time are required to place the raw material in the proper configuration, and interlaminar fracture toughness of the cured laminate is low. One solution to these problems is to use a material with a three-dimensional fiber orientation which is infiltrated and cured in one step. Often these materials are fabricated near net-shape by automated machines, thus reducing the number of fabrication steps after cure and reducing the total number of parts.

One example of how this technology can be used is in stiffened panel fabrication. With prepreg, the stiffeners are often constructed separately and then bonded to a composite skin with an adhesive. The bonded stiffeners are often riveted or bolted to the outer panel to prevent stiffener/skin delamination. This adds several costly fabrication steps, causes stress concentrations around the holes, and increases the overall complexity of the part. With a woven preform, the same part could be automatically constructed from individual tows and contain through-the-thickness reinforcement within the part and between the stiffener and the skin. For example, the skin and stiffener could be con-

structed from woven fabric. Several layers of fabric could be stitched together to form the skin and other layers for the stiffener. The stiffener could then be stitched to the panel to prevent debonding. The stitching material will increase the through-the-thickness strength and will act as crack arresters in the event of interlaminar damage.

In general, it would be difficult to prepreg a three-dimensional preform with currently available prepreg technology due to the complex geometry. An alternative method is to place the dry preform in a mold and inject it with a liquid resin. This process is called resin transfer molding (RTM). The process is quite complex; the resin must be heated to lower its viscosity, the material must be compressed to hold it in place during infiltration and increase its volume fraction, the resin must displace all of the entrapped air, and it must completely fill the preform before it gels. An analytical model can help identify the significant parameters in the processing cycle which will lead to a better understanding of the physical problem. The model can also eliminate the trial-and-error approach to process development and eventually lead to optimal procedures for infiltration and cure. Consequently, the objective of this research is to develop and test an analytical processing model to simulate the infiltration and cure of advanced composite materials via the resin transfer molding process.

The development and testing of the processing model is discussed in the following chapters. First, the current literature which pertains to this work is discussed. Chapters 3 and 4 outline the infiltration and cure sub-models which compose the processing model. Numerical solution of the governing equations is discussed in Chapter 5. Experimental methods for testing individual parts of the model and cured laminate experiments are discussed in Chapter 6. Experimental results and conclusions are discussed in Chapter 7. Chapter 8 contains the process model verification and several parametric

studies of infiltration. Finally, Chapter 9 contains the major conclusions of this work and suggests several possible areas for future work.

## **2.0 LITERATURE REVIEW**

Previous studies of composite process modeling have dealt with the use of pre-impregnated, unidirectional materials. Consolidation of the reinforcing material and flow of resin are typically assumed to behave similarly to a saturated porous media. The RTM process is slightly different because the reinforcement is initially unsaturated. The material is compressed when dry and then infiltrated with a reactive resin. The infiltrated preform is then cured in a manner similar to pre-impregnated materials. This literature review is divided into two sections, infiltration and cure, to mimic the RTM process.

### **2.1 INFILTRATION**

Infiltration is the process by which one material permeates another. In RTM, a reactive resin permeates a network of fibers. Two approaches have been used to describe this process, a microscopic lubrication theory proposed by Lindt [1], and macroscopic flow theories which assume the fibrous network to behave as an elastic porous medium.

Lindt's work has not been used widely to model composites processing. If the porous media approach is adopted, orientation and distribution of fibers can be quantified by the porosity and permeability of the material. Motion of fibers due to consolidation or applied pressure can be described by the changes in these parameters. The permeability is primarily dependant on the interstitial microstructure of the porous material. As the pore volume decreases, the permeability will increase and slow the fluid. The following is a brief review of current theories pertaining to infiltration of an anisotropic, homogenous, elastic, porous medium.

### 2.1.1 Flow

If inertial effects are ignored, the flow of a Newtonian viscous fluid into a porous medium is governed by D'Arcy's law. In a saturated, three-dimensional material, Rice, Fontugne, Latini, and Barduhn [2] express D'Arcy's law in the following form,

$$v_i = \frac{1}{\mu} K_{ij} \phi_{,j} \quad (2.1.1)$$

where  $v_i$  is the velocity vector,  $\mu$  is the fluid viscosity,  $K_{ij}$  is the permeability tensor, and  $\phi$  represents the hydrodynamic potential. The hydrodynamic potential is the sum of the forces from the applied pressure acting on the fluid and gravity. This form of D'Arcy's law ignores surface effects between the solid material and the saturating fluid. Flow in directions other than the applied pressure gradient are possible due to the off-diagonal terms in the permeability tensor.

Coulter, Smith, and Güçeri [3] attempt to simulate infiltration by uncoupling D'Arcy's law for two-dimensional flow. A stream function,  $\psi$ , is introduced and Equation 2.1.1 becomes,

$$\mu \left[ \frac{\partial^2 \psi}{\partial x^2} + \left( \frac{K_y}{K_x} \right) \frac{\partial^2 \psi}{\partial y^2} \right] = 0 \quad (2.1.2)$$

which is solved using a quasi-steady state approach. A computational technique using a boundary fitted coordinate system is used to solve the Equation 2.1.2 and obtain the position of the advancing resin front as a function of time. The permeabilities  $K_x$  and  $K_y$  and the viscosity are assumed to be known constants. A flow simulation is performed for a rectangular mold geometry with the fluid entry and exit points at diagonal corners. Correlation between experiment and simulation is good away from the mold boundaries.

Martin and Son [4] approach the infiltration process in a similar fashion. A finite element routine is used in a quasi-steady state procedure to calculate the position of the resin front. Permeabilities are obtained from the material porosity. Results of a two-dimensional, constant viscosity simulation from a point source to a line sink compare favorably with experimental results.

## 2.1.2 Compaction

The porosity is defined as the volume of the interstitial spaces which can be saturated with fluid, divided by the bulk volume. If the material is completely saturated, the porosity  $\phi$ , resin volume fraction  $v_r$ , and the solid volume fraction  $v_s$ , are related as follows,

$$\phi = v_r = 1 - v_f \quad (2.1.3)$$

When a compressive load is applied to the porous material, the porosity will decrease. The porosity can be related to the applied compaction pressure in several ways. Three approaches have been used for composite process modeling: a strength of materials approach, an empirical approach, and a relationship based on the bulk density of the material.

Gutowski, Kingery, and Boucher [5] relate the compaction of dry, unidirectional, prepreg plies to the stiffness of a representative element. The element is composed of a curved section of fiber within a specific volume of material as shown in Figure 1. Curved beam theory is used to model the pressure-deflection characteristics of the wavy fiber with generic end conditions. The pressure-deflection relationship is given in the following expression,

$$P = \frac{\pi}{64} \frac{Ed^4}{\alpha DL^4} \delta \quad (2.1.4)$$

where  $P$  is the applied pressure,  $\delta$  is the deflection of the fiber,  $E$  is Young's modulus,  $L$  is the length of the curved beam element,  $D$  is the depth of representative volume element,  $d$  is the fiber diameter, and  $\alpha$  is a constant which is related to the end conditions.

Two cases are considered for the deformation of the representative volume element. Case 1 assumes the element depth to be equal to the height throughout the deformation. In Case 2, the depth of the representative volume element is fixed, thus the material can deform in only one direction. The relationship between the pressure applied to the fibers and the changes in the solid volume fraction can be stated by the following expressions,

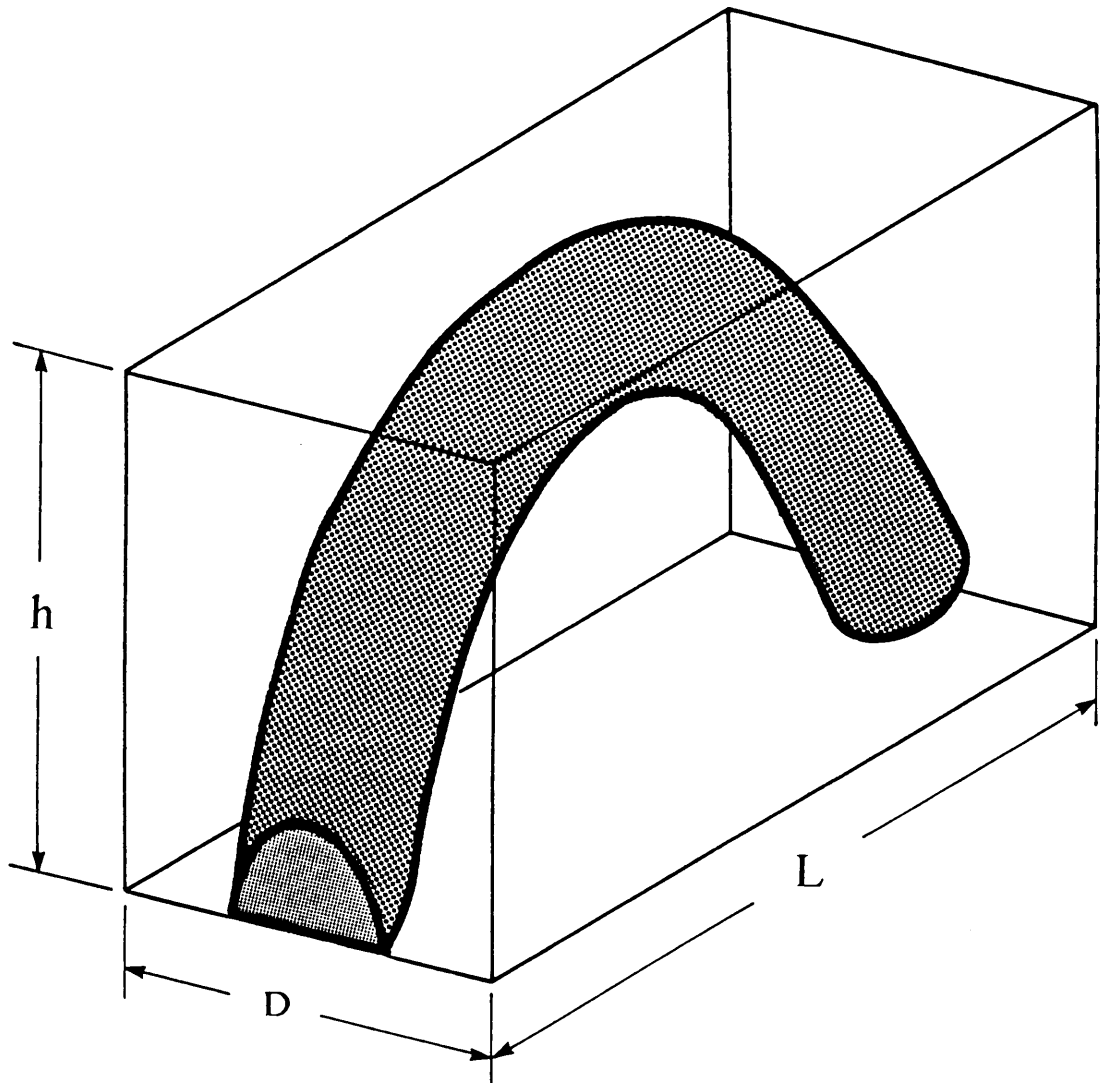


Figure 1. Gutowski, Kingery and Boucher [5] representative volume element for fiber deformation.

Case 1:

$$P = \frac{\pi}{64} \frac{E}{\alpha \beta^4} \frac{\sqrt{\frac{v_f}{v_o}} - 1}{\left( \sqrt{\frac{v_a}{v_f}} - 1 \right)^4} \quad (2.1.5)$$

Case 2:

$$P = \frac{\pi}{64} \frac{E}{\alpha \beta^4} \frac{1 - \frac{v_o}{v_f}}{\left( \frac{v_a^*}{v_f} - 1 \right)^4} \quad (2.1.6)$$

where  $v_o$  and  $v_a^*$  represent the minimum possible volume fraction for Case 1 and Case 2, respectively,  $v_o$  represents the maximum volume fraction (ie.  $P = 0$ ), and  $\beta$  is related to the waviness of the fiber. Pressure versus volume fraction data for Hysol-Grafil XA-S, Hercules AS-4, and S-2 glass fibers is reported by Gutowski *et al.* [5] for compaction pressures from 0 to 4200 kPa. Excellent correlation is achieved with Case 1 and Case 2 expressions.

A macroscopic stiffness formulation is used by Hou [6]. The behavior of a bundle of dry aligned fibers is simulated by a finite length, nonlinear stiffening spring. The form of the relationship is,

$$P = \frac{K}{A} \frac{h_o - h}{\left( 1 - \frac{h_o - h}{h_f} \right)^n} \quad (2.1.7)$$

where  $K$  is the stiffness of the fiber bed,  $A$  is the area,  $h$  is the thickness of the sample, and  $n$  is an empirical constant which accounts for material non-linearities. The quanti-

ties  $h_o$  and  $h$ , represent the bed thickness when  $P = 0$  and as  $P \rightarrow \infty$  respectively. Sample thickness can be related to the volume fraction with the following expression,

$$\frac{v_f}{v_f^o} = \frac{h_o}{h} \quad (2.1.8)$$

where  $v_f^o$  is the volume fraction at zero pressure. Using Equation 2.1.8, the pressure-deflection relationship becomes,

$$P = K_f \left[ \frac{\frac{v_f - v_f^o}{v_f}}{1 - \frac{\frac{v_f - v_f^o}{v_f}}{\frac{v_f^o - v_f^o}{v_f}}} \right]^n \quad (2.1.9)$$

where,

$$K_f = \frac{Kh_o}{A} \quad (2.1.10)$$

and  $v_f^o$  is the volume fraction as  $P \rightarrow \infty$ . Hou uses Equations 2.1.9 and 2.1.10 with the values of,  $v_f^o = 0.5$ ,  $v_f = 0.8$ ,  $K = 50$ , and  $n = 1.475$  to achieve excellent correlation with data reported by Gutowski [7].

The second modeling approach used in the current literature is empirically based. Dave, Kardos and Duduković [8] relate the effective stress applied to a fiber preform,  $P$ , to the void ratio,  $e$ , by the non-linear compaction law from Davis and Raymond [9]. Davis and Raymond developed the following three parameter relationship for normally consolidated clay soils,

$$e = e_1 - C_c \log_{10}(\frac{P}{P_1}) \quad (2.1.11)$$

where Dave *et al.* [8] relates the void ratio in terms of the resin volume fraction by,

$$e = \frac{v_f}{1 - v_f} \quad (2.1.12)$$

The void ratio  $e_1$  is measured at a specified effective stress of  $P_1$ . The parameter  $C_c$ , is called the compression index and is determined by experimentation.

Williams, Donnellan and Trabocco [10] introduce a “bed compressibility factor”,  $E$ , to obtain the following relationship,

$$P = E \left( \frac{1}{v_r - v_{r\infty}} - \frac{1}{v_{ro} - v_{r\infty}} \right) \quad (2.1.13)$$

where  $v_r$  is the resin volume fraction, and  $v_{ro}$ ,  $v_{r\infty}$  are the resin volume fractions when  $P = 0$  and as  $P \rightarrow \infty$  respectively. Williams, Donnellan, and Trabocco [11] report data values for a plain weave, glass fiber cloth and unidirectional graphite fibers. Equation 2.1.13 is used with modest results for the graphite fibers. Appreciable scatter is observed for the glass cloth when compared to either the graphite fibers or the data reported by Gutowski *et al.* [5]. Deviations between Equation 2.1.13 and the glass data are attributed to drift in the displacement transducer used to measure fabric thickness.

The bulk density concept is used by Gauvin, Chabani, and LaFontaine [12] and Adams, Miller, and Rebenfeld [13]. If the saturating fluid is assumed to be much less dense than the solid constituents, the total mass of the material,  $M_{total}$ , can be written as,

$$M_{\text{total}} = \rho_{\text{Bulk}} V_{\text{Bulk}} = \rho_s V_s \quad (2.1.14)$$

where  $\rho_{\text{Bulk}}$  and  $\rho_s$  represent the bulk and solid densities, and  $V_{\text{Bulk}}$  and  $V_s$  are the bulk and solid volumes. The bulk density of the material is related to the thickness and the areal weight, where the areal weight  $\xi$ , is defined as the mass of material per unit surface area. Using the definition of the solid volume fraction, the following expression is obtained,

$$\nu_f = \frac{\xi}{t \rho_s} \quad (2.1.15)$$

where  $t$  is the material thickness. Additional knowledge of how the thickness changes with the applied load is necessary for characterization of the pressure-porosity behavior of the material.

### 2.1.3 Porosity-Permeability

Two major approaches have been used to relate the material porosity to the permeability. Early work by Springer [14,15], Loos and Springer [16], and Hou [6] use D'Arcy's law to model the saturated flow of resin through aligned fiber prepreg normal to the plane of the plies. Halpin, Kardos and Duduković [17] use a quasi-three dimensional form of D'Arcy's law, and Coulter *et al.* [3] use a quasi-two dimensional form, to simulate the resin flow. Each of these approaches assumes the permeability to be independent of the compaction pressure during the manufacturing cycle.

To account for the permeability changes in the fibrous preform during processing, Williams *et al.* [10] and Martin and Son [4] use the Kozeny theory. Kozeny's expression

is an example of a hydraulic radius theory for flow through porous media. The permeability is related to the porosity as follows,

$$K = \frac{C\phi^3}{S^2} \quad (2.1.16)$$

where  $C$  is a constant based on the cross-sectional shape of an idealized stream tube,  $\phi$  represents the material porosity, and  $S$  is the surface area per unit volume. For complex geometries, the Kozeny constant,  $C$ , is often empirically determined since the fluid channel does not have a constant cross-section, and is not straight.

The majority of the current processing models use a modification of Kozeny's theory attributed to Carman [7,13,17-22]. When the porous medium is composed of fibers of diameter  $d_f$ , the Kozeny-Carman can be expressed as,

$$K = \frac{d_f^2}{\kappa} \frac{\phi^3}{(1 - \phi)^2} \quad (2.1.17)$$

where  $\kappa$  is constant for a particular material and is usually determined by experiment.

Gutowski, Cai, Bauer, Boucher, Kingery, and Wineman [23] use Kozeny's original theory to develop a slight modification of the Kozeny-Carman expression. The curved fiber geometry and a Case 1 deformation behavior discussed in Section 2.1.2 are used to obtain,

$$K = \frac{d_f^2}{16\kappa} \frac{\left(\sqrt{\frac{v_a}{v_f}} - 1\right)^3}{\left(\frac{v_a}{v_f} - 1\right)} \quad (2.1.18)$$

where  $v_c$  is “the volume fraction for which all flow is essentially shut off”. Equation 2.1.18 and experimental data correlate well for the simulation of prepreg composite manufacture.

## 2.2 CURE

The cure of epoxy resins is a thermo-chemical process which promotes the cross linking of adjacent polymer chains. This process is dependent on the time-temperature history during cure and the resin composition. Literature models for the cure of epoxy resins are composed of two major sub-models; a heat transfer model to obtain the temperature distribution in the resin and a chemical model to describe changes in polymer chemistry. The temperature distribution is dependent on the tooling used to contain the resin/fiber mixture and the internal heat generation due to exothermic chemical reactions. An unsteady heat conduction equation of the following form is often used to model the heat transfer.

$$\rho_c C_c \frac{\partial T}{\partial t} = \frac{\partial}{\partial z} \left( K_c \frac{\partial T}{\partial z} \right) + \rho_c \dot{H}_c \quad (2.2.1)$$

In this expression,  $\rho$  represents the density,  $C$  is the specific heat,  $K$  is the thermal conductivity,  $\dot{H}_c$  represents the rate of heat generation, and the subscript  $c$  refers to the properties of the composite.

Many methods have been used to describe the changes in resin chemistry with time and temperature. Lee, Loos and Springer [24] define the degree of cure,  $\alpha$ , to be the ratio of the heat generated at time  $t$ , to the ultimate heat of reaction  $H_{Tr}$ , ie.

$$\alpha = \frac{H_r(t)}{H_{Tr}} \quad (2.2.2)$$

In general, the viscosity and the rate of change of the degree of cure are nonlinear functions of temperature and degree of cure. The functional form of these expressions is dependent on the resin being modeled. Lee *et al.* [24] describe the reaction rate of Hercules 3501-6 with the following expression,

$$\frac{\partial \alpha}{\partial t} = (K_1 + K_2\alpha)(1 - \alpha)(B - \alpha) \quad \text{for } \alpha \leq 0.3 \quad (2.2.3)$$

$$\frac{\partial \alpha}{\partial t} = K_3(1 - \alpha) \quad \text{for } \alpha > 0.3 \quad (2.2.4)$$

where the rate constants  $K_i$  are expressed with Arrhenius type expressions of the form,

$$K_i = A_i \exp\left(\frac{-\Delta E_i}{RT}\right) \quad i = 1, 2, 3 \quad (2.2.5)$$

where  $R$  is the universal gas constant and  $\Delta E_i$  are the activation energies. Constants  $A_i$  and  $\Delta E_i$  are determined by differential scanning calorimetry (DSC) experiments. The viscosity can then be expressed by,

$$\mu = \mu_\infty \exp\left(\frac{U}{RT} + K_\mu \alpha\right) \quad (2.2.6)$$

where  $U$  is the activation energy with respect to the viscosity. The values of  $\mu_\infty$ ,  $U$ , and  $K_\mu$  are determined from isothermal viscosity tests.

## **3.0 INFILTRATION MODEL**

Resin transfer molding is unique compared to other composite manufacturing methods because the infiltration and cure of the resin can be accomplished in one step. The resin infiltrates the fiber preform due to a differential between the internal resin pressure and the externally applied pressure. Prepregging depends on gravitational, roller, and surface forces for infiltration. After infiltration, additional heat and pressure is applied to completely cure the resin.

The infiltration model was used to analytically simulate flow of a reactive resin into a fibrous reinforcement. Two fundamental assumptions have been used to develop the model; the reinforcing material was assumed to behave as an anisotropic, homogenous, elastic, porous medium and the resin was assumed to behave as a Newtonian viscous fluid. Infiltration depends on the interstitial microstructure of the material and the fluid viscosity. Changes in the material due to the compaction pressure have been described by the deformation sub-model. The fluid viscosity depends on the time-temperature history of the resin. The infiltration model will yield the position of the resin front versus

time and the fiber volume fraction as functions of the compaction pressure, resin pressure and the infiltration temperature.

### 3.1 FLOW SUB-MODEL

In some cases, material deformation can cause flow. Flow through a rigid porous material is dependent on pressure gradients in the fluid, while a deforming material can also develop flow due to a decrease in pore volume in the saturated region. Three combinations of deformation and flow will be discussed; dry compaction, deformation of a material completely saturated with fluid, and a material partially saturated with fluid.

Consider a porous material surrounded by an impermeable boundary. If a compaction pressure is applied to a dry material, the solid will deform and the porosity will decrease as shown in Figure 2. This process is called compaction. If the same material is completely saturated with a viscous fluid, the compaction pressure will be divided between the solid and the liquid. Since the liquid is incompressible and cannot flow through the boundaries, the system will not deform.

A partially saturated material will react very differently to an applied compaction pressure. The interface between the saturated and unsaturated regions can be considered to be a free surface and is labeled in Figure 3. Above the free surface, the system will behave as a dry material. Below the free surface, the system will behave as a completely saturated material. A pressure gradient will develop in the liquid due to load transfer from the solid material to the fluid. The resulting deformation of the saturated material will decrease the porosity and cause fluid to flow into the dry region. The liquid will

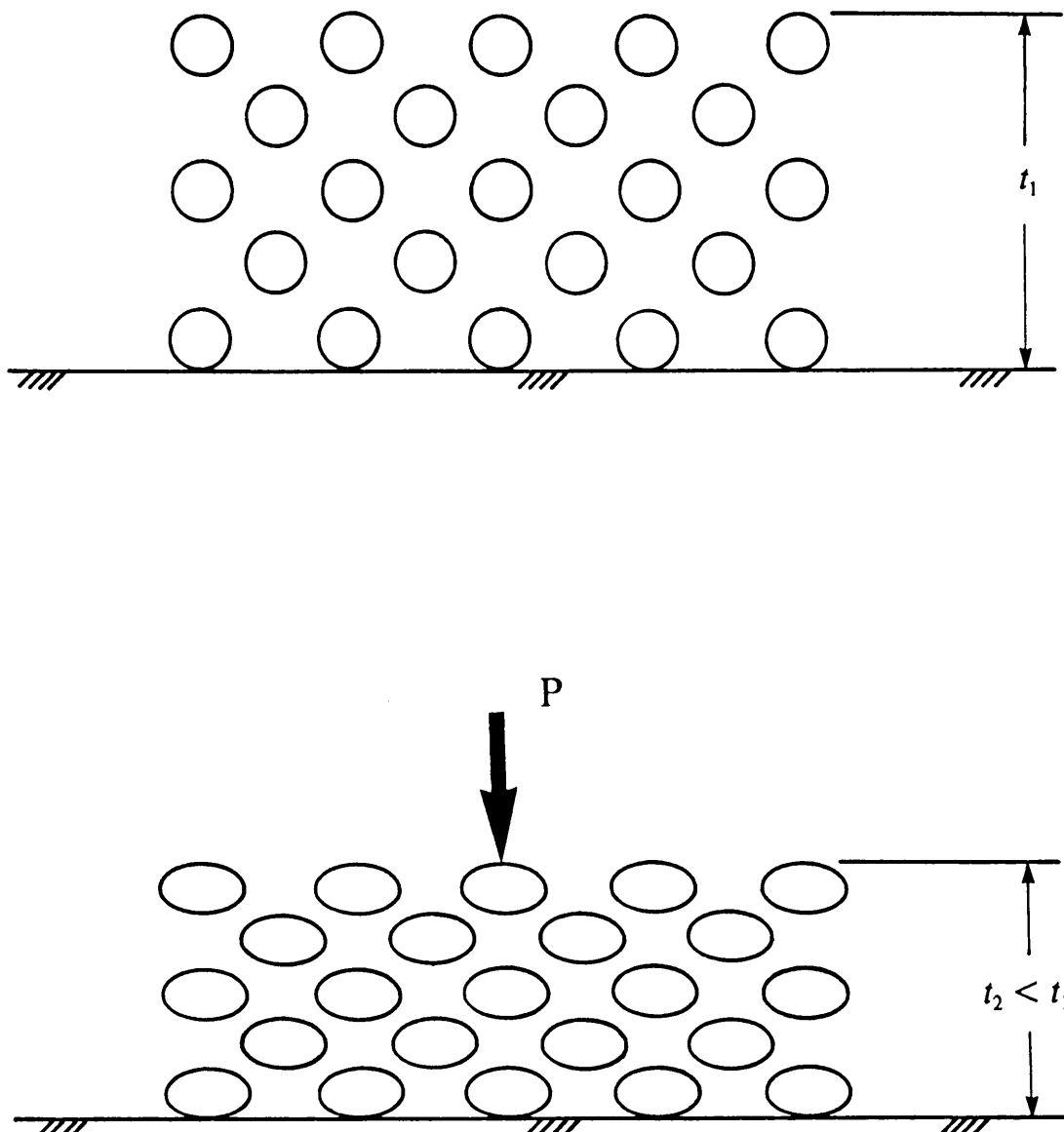


Figure 2. Deformation of a dry porous material with impermeable boundaries.

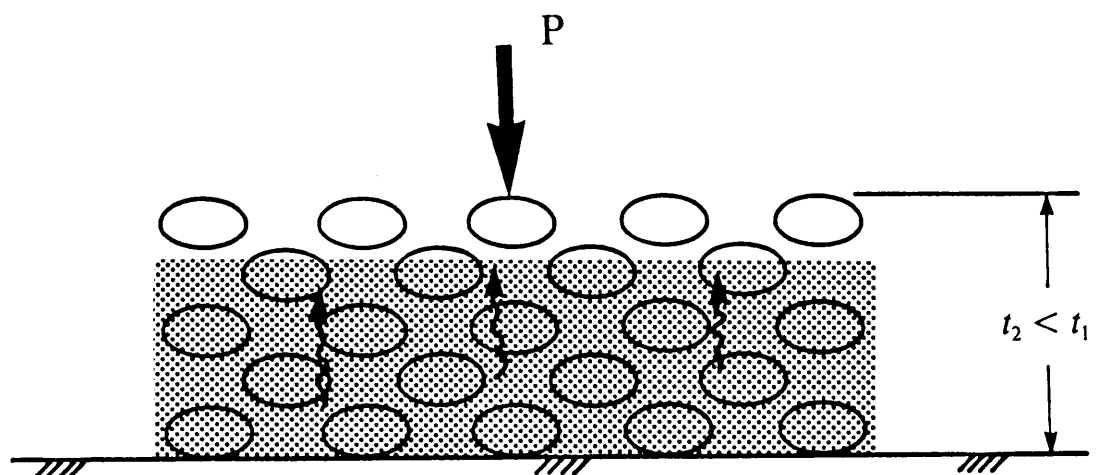
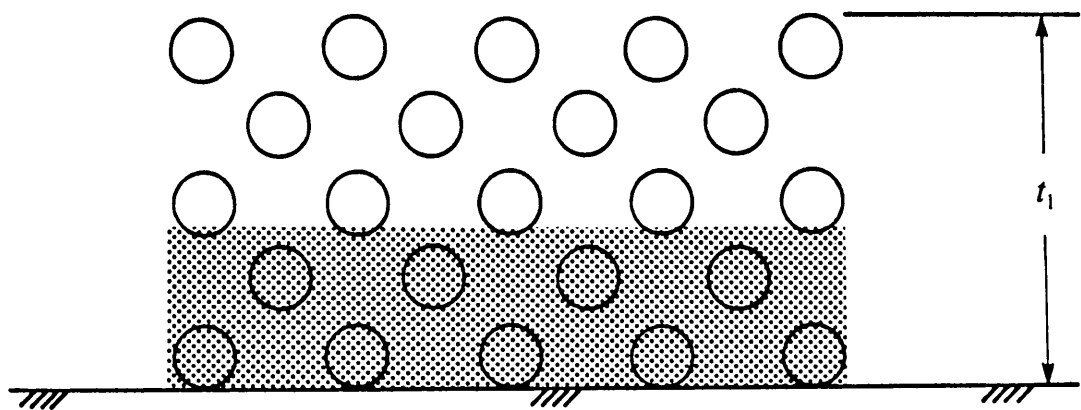


Figure 3. Deformation and flow of a partially saturated porous material with impermeable boundaries.

continue to flow until a new equilibrium point is reached. When the compaction and flow are coupled, the process is called consolidation.

To simplify the infiltration occurring in RTM, this study will not involve consolidation. Pressure on the dry material will cause compaction. However, the reinforcement will not deform during flow.

Fluid motion in a porous material is best described by D'Arcy's law, which states that the velocity of the fluid  $v_i$ , is directly proportional to the hydrodynamic potential  $\psi$ , ie.

$$v_i \propto \psi \quad (3.1.1)$$

where the constant of proportionality is the resistance to flow. If the pressures applied to the liquid are much larger than the pressure distribution developed by gravitational forces, the hydrodynamic potential is equivalent to the gradient of the applied fluid pressures. In this case, D'Arcy's law can be written as follows,

$$v_i = - \frac{K_{ij}}{\mu} P_{,j} \quad (3.1.2)$$

where  $P$  represents the fluid pressure,  $\mu$  represents the viscosity, and  $K_{ij}$  represents the permeability tensor. An adoption of Equation 3.1.2 implies four assumptions for the flow; the effect of surface tension between the solid and the saturating fluid is ignored, viscous forces are much larger than inertial forces, the fluid must behave according to Newton's viscosity law, and the material system must behave as a continuum.

Stresses due to intra-molecular attraction will develop near the interface between a solid and one or more liquids. The resultant force developed in the free surface of the fluid is called the surface tension. Surface tension is very important when trying to coat a fi-

ber with resin. If the tension is large, the resin will not spread easily and will produce uneven resin distributions and trap air within the resin. If the surface tension is low, the resin will coat the fiber evenly. Surface forces could be important if a static fluid supports pressures of the same order of magnitude as the pressures used in processing.

The Reynolds number is defined as the ratio of the inertial forces to the viscous forces in a moving fluid. For flow through a collection of fibers the Reynolds number is,

$$R = \frac{\rho_f d_f v}{\mu} \quad (3.1.3)$$

where  $\rho_f$  represents the density of the fluid, and  $d_f$  represents the diameter of the fibers. When the velocity of the fluid becomes large enough for inertial effects to dominate, the Reynolds number is called the critical Reynolds number. Philip [25] states that the flow changes character near the critical Reynolds number from a linear laminar regime to a nonlinear laminar regime. For porous materials, the critical Reynolds number is not well established. The best estimate for fibrous materials is for Stokes (creeping) flow around a cylinder in a uniform flow field. The critical Reynolds number in this case, is approximately one as shown by White [26].

Equation 3.1.2 is valid for Newtonian viscous fluids. Newtonian fluids are those which obey the following constitutive relationship,

$$\tau = \mu \frac{\partial v}{\partial n} \quad (3.1.4)$$

where  $\tau$  is the shear stress, and  $\frac{\partial v}{\partial n}$  is the velocity gradient in a direction normal to the flow. Polymeric resins are usually non-Newtonian fluids. Often a power law expression is used to describe the constitutive behavior of these materials as follows,

$$\tau = \mu \left( \frac{\partial v}{\partial n} \right)^p \quad (3.1.5)$$

where  $p$  represents the slope of the  $\log\left(\frac{\tau}{\mu}\right)$  versus  $\log\left(\frac{\partial v}{\partial n}\right)$  curve and is considered to be a material parameter.

During infiltration there are two distinct regions in the material; one is completely saturated with liquid resin and the other is saturated with air. Infiltration is usually performed by attaching a vacuum pump to the dry material and applying an external pressure to the system. The energy required to move a volume of air through the porous material is much less than the energy needed to move an equal volume of resin, thus, the air in front of the free surface will not affect infiltration.

The permeability of an anisotropic material can be described by a second order, symmetric, Cartesian tensor which obeys the tensor transformation law,

$$K'_{st} = a_{si} a_{tj} K_{ij} \quad (3.1.6)$$

where  $a_{si}$ ,  $a_{tj}$  represent the direction cosines between the primed and unprimed coordinate systems. Since the permeability is a Cartesian tensor, there exists a system of coordinates for which  $K_{ij} = 0$  for all  $i \neq j$ . This system is called the principal system of coordinates.

Each term in the permeability tensor is important when trying to understand the physical problem. For simplicity consider a two-dimensional, porous material composed of a collection of straight, aligned fibers. The permeability tensor can be written as,

$$\begin{bmatrix} K_{11} & K_{12} \\ K_{12} & K_{22} \end{bmatrix} \quad (3.1.7)$$

If a pressure gradient is applied along the axis of the fibers, the resulting velocity vector will be aligned with the fibers as shown in Figure 4. If a pressure gradient is applied in a direction transverse to the fibers, the flow will also be transverse. Since there is no velocity normal to the pressure gradient in either case,  $K_{12} = 0$ , and the coordinate system is a principal coordinate system. If  $K_{11} = K_{22}$ , the flow characteristics in the axial and transverse directions will be the same, thus the material will be isotropic to the flow. If the values of  $K_{11}$  and  $K_{22}$  are different, the material will be orthotropic to the flow.

Consider the same material with the fibers rotated an angle  $\theta$  from the applied pressure gradient as shown in Figure 5. Transforming the permeability tensor from the principal directions with Equation 3.1.6, the off-diagonal terms will become non-zero. The resulting velocity vector will no longer be aligned with the pressure gradient. This flow situation will be called a coupled flow and the off-diagonal terms of the permeability tensor will be called coupling terms.

## 3.2 DEFORMATION SUB-MODEL

The permeability is dependent on the volume, shape, and orientation of the interconnected pores in the solid material. To describe the resistance to flow as a function of the applied pressure, the permeability must be related to the compaction pressure. Discussion of the changing permeability will be separated into three categories; the com-

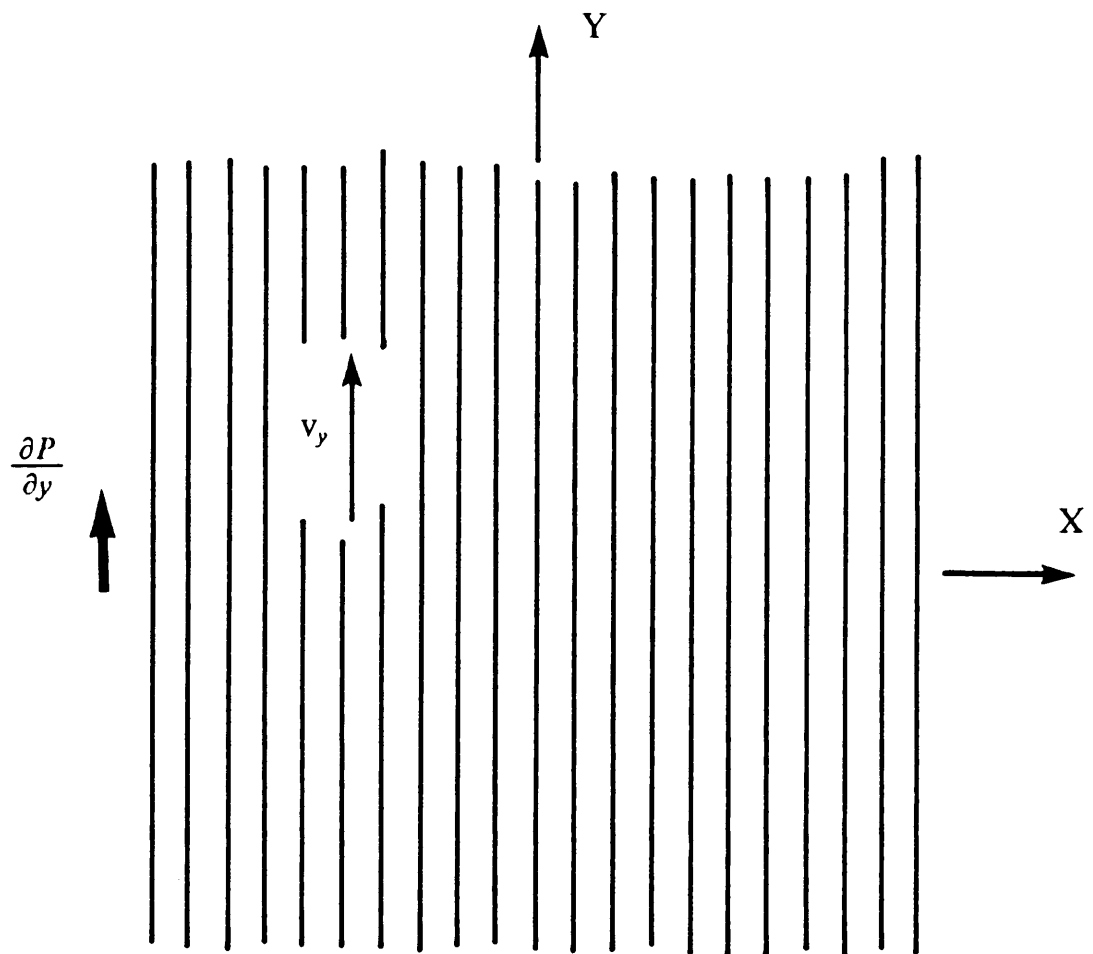


Figure 4. Aligned flow through a system of aligned fibers.

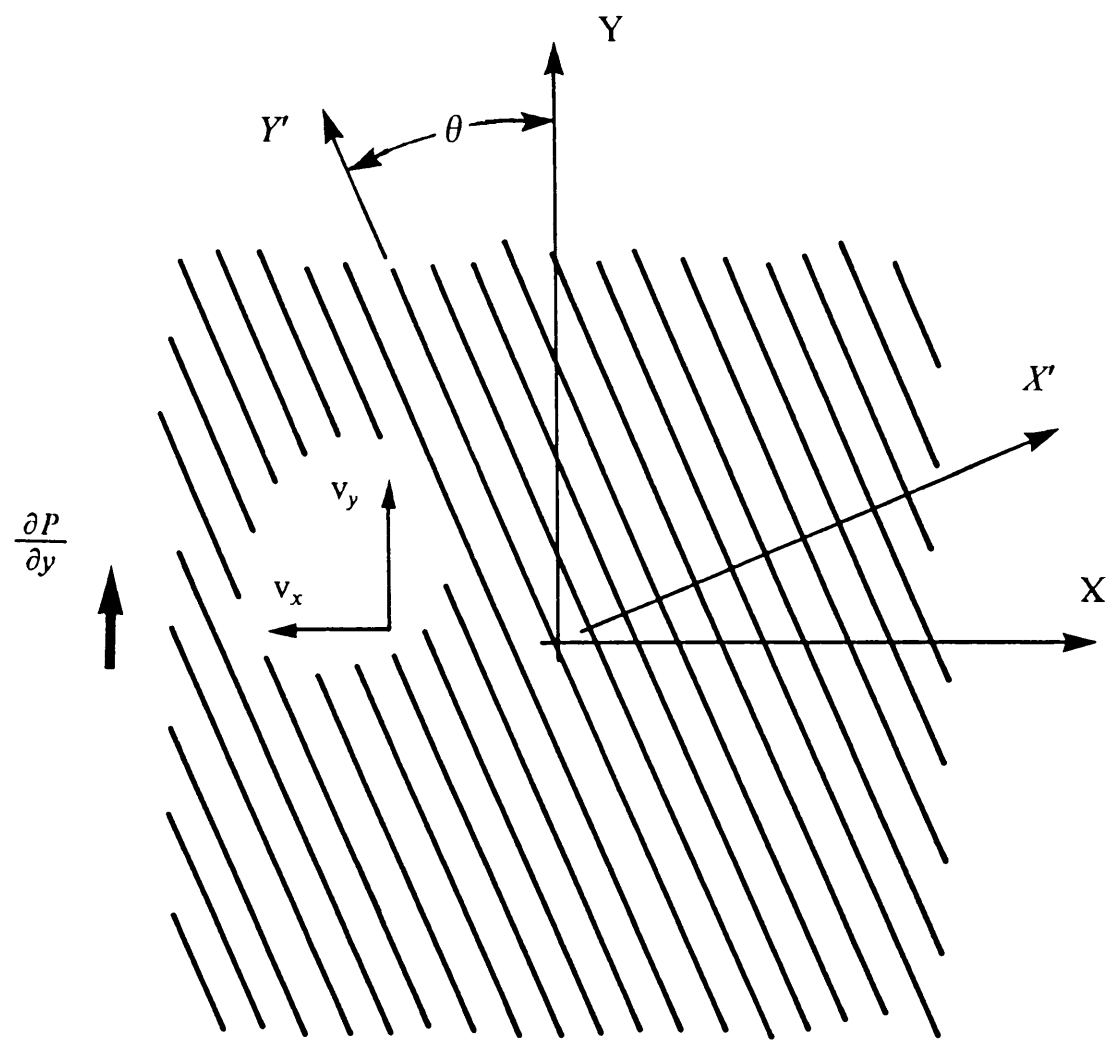


Figure 5. General flow through a system of aligned fibers.

paction of the dry material, the relationship between the material thickness and porosity, and the changes in permeability due to changes in porosity.

### 3.2.1 Compaction

The objective of the compaction model is to describe the thickness of the porous material as a function of the applied compaction pressure. Systems of fibers exhibit a dramatic amount of stiffening [5-13]. Previous approaches to describe this behavior include empirical methods, spring analogies, and curved beam theory. An empirical approach was chosen for this study.

The stiffening behavior of fibrous reinforcements can be described as a nonlinear function of the applied compaction load as follows,

$$d'' = a_0 + a_1(\ln P) + a_2(\ln P)^2 + a_3(\ln P)^3 + \dots \quad (3.2.1)$$

where  $d''$  represents the total deflection of the material, and  $P$  represents the compaction load applied to the material. The polynomial coefficients  $a_i$ , are determined by a least squares curve fit to the measured data. The order of the polynomial was chosen so that the correlation coefficient between the Equation 3.2.1 and the data was at least 95 percent.

Two disadvantages exist with this expression. First, the natural logarithm is not defined for an argument of zero. If a small, finite value of load is assumed to yield zero deflection, Equation 3.2.1 can be modified as follows,

$$d = -d''(P_{\text{zero}}) + a_0 + a_1(\ln P) + a_2(\ln P)^2 + a_3(\ln P)^3 + \dots \quad (3.2.2)$$

where  $P_{\text{zero}}$  is the load for zero deflection.

The second disadvantage is the difficulty to describe path dependent behavior. Path dependency exists when the material behaves differently during loading than during unloading. To account for this behavior, the loading and unloading data were fit separately to Equation 3.2.1. The loading curve was adjusted as in Equation 3.2.2 to obtain the following expression for loading,

$$d_L = -d'(P_{\text{zero}}) + a_0 + a_1 \ln(P_L) + a_2(\ln P_L)^2 + a_3(\ln P_L)^3 + \dots \quad (3.2.3)$$

and for unloading,

$$d'_U = b_0 + b_1 \ln(P_U) + b_2(\ln P_U)^2 + b_3(\ln P_U)^3 + \dots \quad (3.2.4)$$

where the deflection  $d'_U$  is dependent on the value of the load reversal point used during testing. The unloading expression must be modified for any value of the load reversal. For continuous load-deflection behavior,

$$d_L(P_{\text{max}}) = d_U(P_{\text{max}}) \quad (3.2.5)$$

where  $P_{\text{max}}$  represents the load reversal point and  $d_U$  is the corrected deflection for unloading. If

$$d_L(P_{\text{max}}) < d_U(P_{\text{max}}) \quad (3.2.6)$$

then the unloading expression becomes

$$d_U = -d'_U(P_{\text{max}}) + d_L(P_{\text{max}}) + b_0 + b_1(\ln P) + b_2(\ln P)^2 + b_3(\ln P)^3 + \dots \quad (3.2.7)$$

A similar procedure can be used to modify multiple loading/unloading cycles for any set of load reversal values. If the uncompressed thickness is known and several compression tests are conducted, the thickness of the material can be determined for any load history.

### 3.2.2 Porosity

The porosity of a material is defined as the volume of interconnected pores divided by the total volume. The volume of solid divided by the total volume is called the solid volume fraction or the fiber volume fraction and is related to the porosity by Equation 2.1.3. A compaction load will cause the thickness and pore volume of the material to decrease. Gauvin *et al.* [12] approach has been used to determine the relationship between compaction pressure and porosity.

Gauvin *et al.* [12] consider a porous material completely saturated with a fluid. The mass of the solid-fluid mixture is

$$M_{tot} = \rho_s V_s + \rho_f V_f = \rho_{bulk} V_{tot} \quad (3.2.8)$$

where  $\rho_s$  and  $V_s$  represent the density and volume, respectively, of the solid and  $\rho_f$  and  $V_f$  represent the density and volume of the fluid. The bulk density, which is defined as the density of the solid-fluid mixture, can be written as follows,

$$\rho_{bulk} = \rho_s \frac{V_s}{V_{tot}} + \rho_f \frac{V_f}{V_{tot}} \quad (3.2.9)$$

Since Equation 3.2.8 is valid for any fluid, assume the density of the fluid is much smaller than the density of the solid. Using Equations 2.1.3 and 3.2.9, the fiber volume fraction can be written as,

$$v_f = 1 - \phi = \frac{\rho_{bulk}}{\rho_s} \quad (3.2.10)$$

The bulk density can be described in terms of material parameters. The areal weight, or the surface density, is defined as the mass of material divided by the macroscopic surface area. This quantity is usually specified by textile manufacturers to describe the “weight” of a material.

Consider  $n$  plies of material with an areal weight  $\xi$ . The bulk density can be written as,

$$\rho_{bulk} = \frac{n \xi}{t} \quad (3.2.11)$$

where  $t$  is the thickness of  $n$  plies. If more than one type of material is used, the bulk density becomes,

$$\rho_{bulk} = \sum_{i=1}^N \frac{n_i \xi_i}{t_i} \quad (3.2.12)$$

where  $N$  represents the total number of different materials. Combing Equations 3.2.10, and 3.2.12, the fiber volume fraction can be written as,

$$\nu_f = 1 - \phi = \sum_{l=1}^N \frac{n_l \xi_l}{t_l \rho_{st}} \quad (3.2.13)$$

With this expression the solid volume fraction can be determined for any applied compaction pressure provided the density of the solid material, areal weight, and the compaction coefficients are known.

### 3.2.3 Permeability

The final relationship required to model the infiltration process is an expression for the permeability as a function of material porosity. This section describes the permeability of a network of fibers by the hydraulic radius theory as described by Scheidegger [27]. This approach is attributed to Kozeny who describes the porous medium as a collection of channels. Kozeny defines the hydraulic radius as the ratio of the total volume of material to the exposed surface area. This description assumes that the distribution of similar sized pores in the material is random, the porosity is not excessively high, no diffusion is present (ie. the fluid motion occurs due to applied pressures and not due to surface effects), and the flow through the porous material is similar to flow through a capillary.

From dimensional analysis, Kozeny assumes the permeability can be written as,

$$K = \frac{c' m^2}{f_\phi} \quad (3.2.14)$$

where  $m$  is the hydraulic radius, and  $\frac{c'}{f_\phi}$  represents a nondimensional factor related to the porosity of the material. Navier-Stokes equation is solved for a collection of stream tubes normal to the flow to determine the form of this nondimensional factor.

D'Arcy's law is adapted by Kozeny to account for the actual distance a fluid particle travels within the porous material by modifying the pressure gradient as follows,

$$P'_{,j} = \frac{1}{T} P_{,j} \quad (3.2.15)$$

where  $P_{,j}$  represents the pressure gradient assuming a straight flow path,  $P'_{,j}$  represents the adjusted gradient, and  $T$  represents the "tortuosity", defined as the actual path length divided by the apparent length through the material.

Comparing the solution of Navier-Stokes equation with the adjusted form of D'Arcy's law, Kozeny obtains

$$K = \frac{c \phi^3}{T S^2} \quad (3.2.16)$$

where  $c$  is related to the cross-sectional shape of an idealized stream tube, and  $S$  represents the specific surface. Kozeny defines the specific surface as the surface area exposed to the flow divided by the total volume.

Carman extends Kozeny's original work by selecting the value of  $c$  to match experimental data. Carman also redefines the specific surface to be the surface area exposed to the flow divided by the solid volume and obtains,

$$K = \frac{1}{5 T S_o^2} \frac{\phi^3}{(1 - \phi)^2} \quad (3.2.17)$$

were  $S_o$  represents Carman's specific surface.

To extend Equation 3.2.17 to systems of fibers, an empirical constant,  $\kappa$ , is typically introduced to obtain

$$K = \frac{d_f^2}{\kappa} \frac{\phi^3}{(1 - \phi)^2} \quad (3.2.18)$$

where  $\kappa$  is called the Kozeny-Carman constant. The Kozeny-Carman constant accounts for the shape of the stream tube and the tortuosity.

To extend Equation 3.2.18 to include anisotropy, the Kozeny-Carman constant is assumed to be directionally dependent, ie.

$$K_{ij} = \frac{d_f^2}{\kappa_{ij}} \frac{\phi^3}{(1 - \phi)^2} \quad (3.2.19)$$

To use this expression with D'Arcy's law, an experimental investigation would be needed to determine the six unknown Kozeny-Carman constants.

## 4.0 CURE MODEL

To effectively simulate the RTM manufacturing method, the characteristics of the resin system need to be known during infiltration and cure. The approach developed by Loos and Springer [28] for the cure of graphite-epoxy prepgs was used to describe the heat transfer through the saturated reinforcement and cure of the resin. Changes in viscosity must be characterized so that D'Arcy's law can be used to describe the flow of resin. Other characteristics which need to be known include the progression of the chemical reactions and the heat generated by these reactions. The viscosity and extent of cure depend on the time-temperature history of the system and the resin chemistry. The resin temperature is assumed to be uniform during the infiltration process, neglecting the temperature lag due to conduction through the tooling and the heat generated by the curing resin. For thin laminates and slow heating-cooling rates, these effects will be negligible. The cure model will be discussed in three sections; heat transfer, resin kinetics and viscosity sub-models.

## 4.1 HEAT TRANSFER SUB-MODEL

Heat is typically transferred to the composite from an autoclave or heated platen press. In the autoclave the outer surface of the tooling is heated by forced convection from a uniform environment and is transferred to the composite by conduction through the tool plate and the breather plies. Due to changes in the environment and the chemical reactions occurring within the resin, the temperature within the reinforcement will vary with time and position, ie.

$$T = T(z, t) \quad (4.1.1)$$

A schematic of the tooling surrounding the composite is shown in Figure 6.

The equations governing the heat transfer are derived from a one-dimensional form of the conservation of energy. Conduction of heat within the tooling and breather plies is governed by the following expression,

$$\rho_i C_i \frac{\partial T}{\partial t} = \frac{\partial}{\partial z} \left( K_i \frac{\partial T}{\partial z} \right) \quad (4.1.2)$$

where  $\rho$  is the density of the material,  $C$  is the specific heat, and  $K$  represents the thermal conductivity. The subscript  $i$  in this equation refers to either the tool plate or the bleeder plies.

This form of the conservation of energy must be altered slightly before it can be applied to the composite laminate since heat is produced within the resin due to exothermic chemical reactions. To account for the additional energy, Equation 4.1.2 can be modified by introducing a heat generation term as follows,

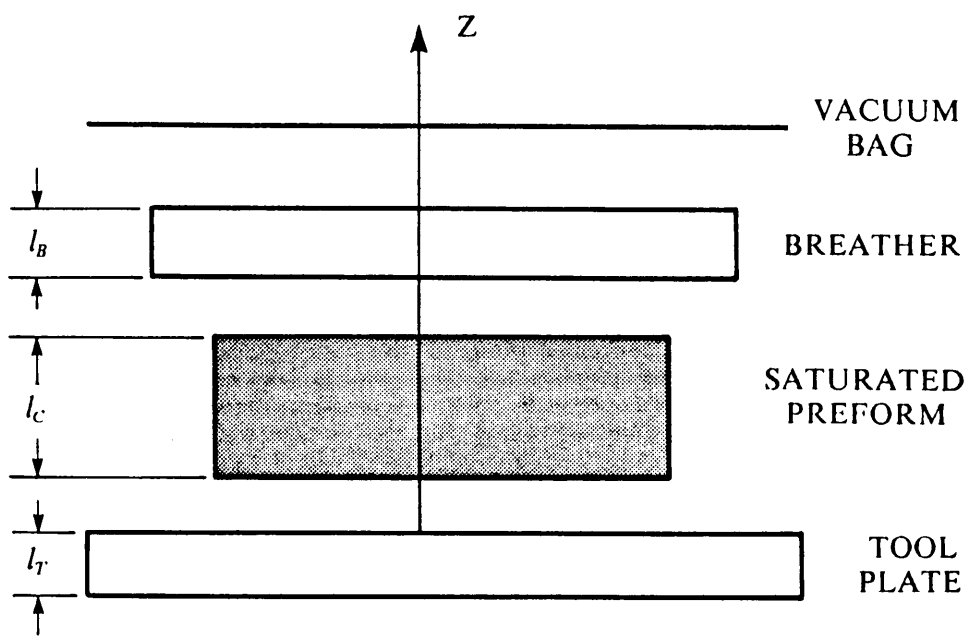


Figure 6. Vacuum bag schematic used to model heat transfer during RTM.

$$\rho_c C_c \frac{\partial T}{\partial t} = -\frac{\partial}{\partial z} \left( K_c \frac{\partial T}{\partial z} \right) + \rho_c \dot{H}_c \quad (4.1.3)$$

where  $\dot{H}_c$  represents the rate of heat generation, and the subscript  $c$  refers to the properties of the composite.

To determine the effective thermal properties of the composite, Loos and Springer [28] develop relationships for the composite material properties in terms of the properties of the fiber and resin. Using a ‘rule of mixtures’ approach, the specific heat, density and heat generation for the composite can be written as,

$$C_c = C_f + (C_r - C_f)m_r \quad (4.1.4)$$

$$\rho_c = \rho_f + (\rho_r - \rho_f)v_r \quad (4.1.5)$$

$$H_c = \frac{\rho_r}{\rho_c} v_r H_r \quad (4.1.6)$$

where  $m_r$  represents the mass fraction of resin,  $H_r$  is the heat generated within the resin, and  $H_c$  is the heat generated within the composite. The values denoted with subscripts  $f$  and  $r$  refer to the fiber and resin, respectively. Springer and Tsai [29] express the thermal conductivity of the composite for unidirectional fibers systems as follows,

$$K_c = \left( 1 - 2\sqrt{\frac{v_f}{\pi}} \right) K_r + \frac{K_r}{B_f} \left[ \pi - \frac{4}{\sqrt{1 - \frac{B_f^2 v_f}{\pi}}} \tan^{-1} \left( \frac{\sqrt{1 - \frac{B_f^2 v_f}{\pi}}}{1 + B_f \sqrt{\frac{v_f}{\pi}}} \right) \right] \quad (4.1.7)$$

where,

$$B_f = 2 \left( \frac{K_r}{K_f} - 1 \right) \quad (4.1.8)$$

If the heat of reaction of the resin is known, Equations 4.1.2 and 4.1.3 can be solved for the temperature distribution within the composite. Heat generation in the saturated reinforcement is difficult to describe since it also depends on the time-temperature history of the resin. To describe the heat generation it is necessary to examine the chemistry of the resin system.

## 4.2 KINETICS SUB-MODEL

The purpose of the kinetics sub-model is to describe the rate of heat generated within the resin as a function of temperature and time. Assuming the heat liberated at time  $t$ ,  $H_r(T, t)$ , is proportional to the total heat generated during the cure of the resin, the degree of cure can be defined as,

$$\alpha = \frac{H_r(T, t)}{H_{Tr}} \quad (4.2.1)$$

where  $H_{Tr}$  represents the total heat of reaction such that  $H_r \rightarrow H_{Tr}$  as  $t \rightarrow \infty$ . The degree of cure  $\alpha$ , varies from 0 to 1 and is related to the extent of the chemical reactions. If Equation 4.2.1 is differentiated with respect to time, the rate of heat generation can be written as,

$$\dot{H}_r(T, t) = H_{Tr} \frac{\partial \alpha}{\partial t} \quad (4.2.2)$$

where  $\frac{\partial\alpha}{\partial t}$  is called the reaction rate or the cure rate.

The reaction rate and total heat of reaction are dependent on the chemical formulation of the resin system and must be determined from experiments. Since the total heat of reaction is assumed to be constant, the reaction rate can be expressed as,

$$\frac{\partial\alpha}{\partial t} = f(T, t) \quad (4.2.3)$$

Lee, *et al.* [24] describe the functional expression of the reaction rate for Hercules 3501-6 with expressions of the form,

$$\frac{\partial\alpha}{\partial t} = (K_1 - K_2\alpha)(1 - \alpha)(B - \alpha) \quad \text{for } \alpha \leq 0.3 \quad (4.2.4)$$

$$\frac{\partial\alpha}{\partial t} = K_3(1 - \alpha) \quad \text{for } \alpha > 0.3 \quad (4.2.5)$$

where  $K_i$  can be expressed as,

$$K_i = A_i \exp\left(-\frac{\Delta E_i}{RT}\right) \quad i = 1, 2, 3 \quad (4.2.6)$$

where  $R$  represents the universal gas constant. The activation energies,  $\Delta E_i$ , and the pre-exponential factors,  $A_i$ , are determined from differential scanning calorimetry (DSC) experiments.

Assuming no diffusion of chemical species, the degree of cure can be determined for any reaction rate by,

$$\alpha = \int_0^t \frac{\partial \alpha}{\partial t} dt \quad (4.2.7)$$

which must be numerically integrated to estimate the progression of the chemical reactions within the composite.

### 4.3 VISCOSITY SUB-MODEL

To apply D'Arcy's law to the infiltration of a reactive resin, the viscosity must be known. In general, the viscosity depends on the time-temperature history and the shear rate of the resin. Since the resin was assumed to be a Newtonian fluid, the viscosity is independent of the shear rate and can be written functionally as,

$$\mu = f(T, t) \quad (4.3.1)$$

or in terms of the degree of cure,

$$\mu = f(T, \alpha) \quad (4.3.2)$$

As with the resin kinetics, the functional form of the viscosity depends on the resin system being considered. Lee *et al.* [24] describe the viscosity of Hercules 3501-6 with the following expression,

$$\mu = \mu_\infty \exp\left(-\frac{U}{RT} + K_\mu \alpha\right) \quad (4.3.3)$$

where the degree of cure is determined from the kinetics sub-model and constants  $\mu_\infty$ ,  $U$ , and  $K_u$  are determined from isothermal viscosity experiments.

## 5.0 NUMERICAL SOLUTION PROCEDURES

The RTM manufacturing method has been modeled in two parts: infiltration and cure of the resin. From the infiltration model, D'Arcy's law governs the motion of the resin within the porous reinforcement. The viscosity is determined from the temperature within the composite and the resin kinetics. Once infiltration is completed, the transient heat transfer and the kinetics models are used to describe the thermo-chemical changes within the composite.

A quasi-steady state solution of the governing equations has been attempted for the infiltration and cure models. The finite element method was used to determine the position of the resin within the reinforcement. Motion of the infiltration front was simulated by adding an element to the computational mesh at each time step. Heat transfer during final cure was modeled using a one-dimensional, finite difference method. Both solution methodologies will be outlined in the following sections.

## 5.1 GOVERNING EQUATIONS

This section contains a review of the governing differential equations for the RTM process simulation model. Development of these equations has been described in detail in Chapters 3 and 4.

Infiltration is governed by D'Arcy's law for flow of a viscous fluid through an anisotropic, homogenous, porous medium as follows,

$$v_i = - \frac{K_{ij}}{\mu} P_j \quad (3.1.2)$$

The permeability tensor can be related to the applied compaction pressure by the compaction coefficients, pressure-porosity relationship, and the Kozeny-Carman relation as follows,

$$d = -d'(P_{\text{zero}}) + a_0 + a_1 \ln P + a_2 (\ln P)^2 + a_3 (\ln P)^3 + \dots \quad (3.2.2)$$

$$v_f = 1 - \phi = \sum_{i=1}^N \frac{n_i \xi_i}{t_i \rho_{sl}} \quad (3.2.13)$$

$$K_{ij} = \frac{d_f^2}{\kappa_{ij}} \frac{\phi^3}{(1-\phi)^2} \quad (3.2.19)$$

To describe the changes in viscosity of the resin with temperature and time, the viscosity and kinetics sub-models were used. For Hercules 3501-6 the viscosity can be written as,

$$\mu = \mu_\infty \exp\left(-\frac{U}{RT} + K_\mu \alpha\right) \quad (4.3.3)$$

were the degree of cure can be obtained by numerical integration of the following expressions,

$$\frac{\partial \alpha}{\partial t} = (K_1 + K_2 \alpha)(1 - \alpha)(B - \alpha) \quad \text{for } \alpha \leq 0.3 \quad (4.2.4)$$

$$\frac{\partial \alpha}{\partial t} = K_3(1 - \alpha) \quad \text{for } \alpha > 0.3 \quad (4.2.5)$$

where,

$$K_i = A_i \exp\left(-\frac{\Delta E_i}{RT}\right) \quad i = 1, 2, 3 \quad (4.2.6)$$

Heat transfer into the composite can be simulated with the following system of equations: for the composite,

$$\rho_c C_c \frac{\partial T}{\partial t} = \frac{\partial}{\partial z} \left( K_c \frac{\partial T}{\partial z} \right) + \rho_c \dot{H}_c \quad (4.1.3)$$

and for the breather plies and the tool plate,

$$\rho_i C_i \frac{\partial T}{\partial t} = \frac{\partial}{\partial z} \left( K_i \frac{\partial T}{\partial z} \right) \quad (4.1.2)$$

The material constants  $C_c$ ,  $\rho_c$ ,  $H_c$ , and  $K_c$  are related to the constituent material properties by the following expressions,

$$C_c = C_f + (C_r - C_f)m_r \quad (4.1.4)$$

$$\rho_c = \rho_f + (\rho_r - \rho_f)v_r \quad (4.1.5)$$

$$H_c = \frac{\rho_r}{\rho_c} v_r H_r \quad (4.1.6)$$

$$K_c = \left(1 - 2\sqrt{\frac{v_f}{\pi}}\right) K_r + \frac{K_r}{B_f} \left[ \pi - \frac{4}{\sqrt{1 - \frac{B_f^2 v_f}{\pi}}} \tan^{-1} \left( \frac{\sqrt{1 - \frac{B_f^2 v_f}{\pi}}}{1 + B_f \sqrt{\frac{v_f}{\pi}}} \right) \right] \quad (4.1.7)$$

where,

$$B_f = 2 \left( \frac{K_r}{K_f} - 1 \right) \quad (4.1.8)$$

## 5.2 INITIAL AND BOUNDARY CONDITIONS

The governing differential equations are subjected to certain initial and boundary conditions. Several of these conditions have been discussed in previous sections, but will be restated here, in proper mathematical form, for completeness.

Infiltration of a resin into a rigid preform was assumed to occur at a uniform temperature. Assuming  $t = 0$  at the beginning of the flow, these conditions can be written as,

$$\alpha(T, t) = 0 \quad \text{at } t = 0 \quad (5.2.1)$$

$$P = const \quad \text{for } t \geq 0 \quad (5.2.2)$$

$$T(z, t) = T(t) \quad \text{for } 0 \leq t \leq t_{full} \quad (5.2.3)$$

were  $T(t)$  represents the temperature as a function of time, and  $t_{full}$  is the time required to completely infiltrate the material.

Pressures applied to the resin and the dry preform depend on the tooling and environment surrounding the system. Consider the vacuum bag infiltration technique shown schematically in Figure 7. Resin is placed on a tool surface and the reinforcement is placed on top of the resin. A vacuum bag and several breather plies cover the resin and the reinforcement. During autoclave processing, a vacuum pressure is established and held inside the bag while an autoclave pressure is applied to the outside of the bag.

The compaction pressure applied to the dry material is a combination of the autoclave pressure and the vacuum pressure. The pressure differential which forces the resin into the dry reinforcement is also a combination of the vacuum and autoclave pressures. Pressure at the advancing resin front is the same as the pressure in the pores of the dry material, which in this case, is the vacuum pressure. The pressure in the neat resin is equivalent to the pressure on the outside of the system. Pressure gradients will not exist in the resin outside the reinforcement.

In the RTM processing model, the temperature and degree of cure are assumed to be uniform at time  $t = t_{full}$ . The degree of cure can be determined from the time-temperature history during infiltration and the kinetics model.

Boundary conditions for the heat transfer analysis consist of two types; conduction boundary conditions at  $z = 0$  and  $z = l_c$ , and convection boundary conditions at  $z = -l_T$  and  $z = l_b + l_c$  where the boundary positions  $l_c$ ,  $l_T$ , and  $l_b$  are shown in Figure 6. The conduction boundary conditions require equality of the heat flux and temperature

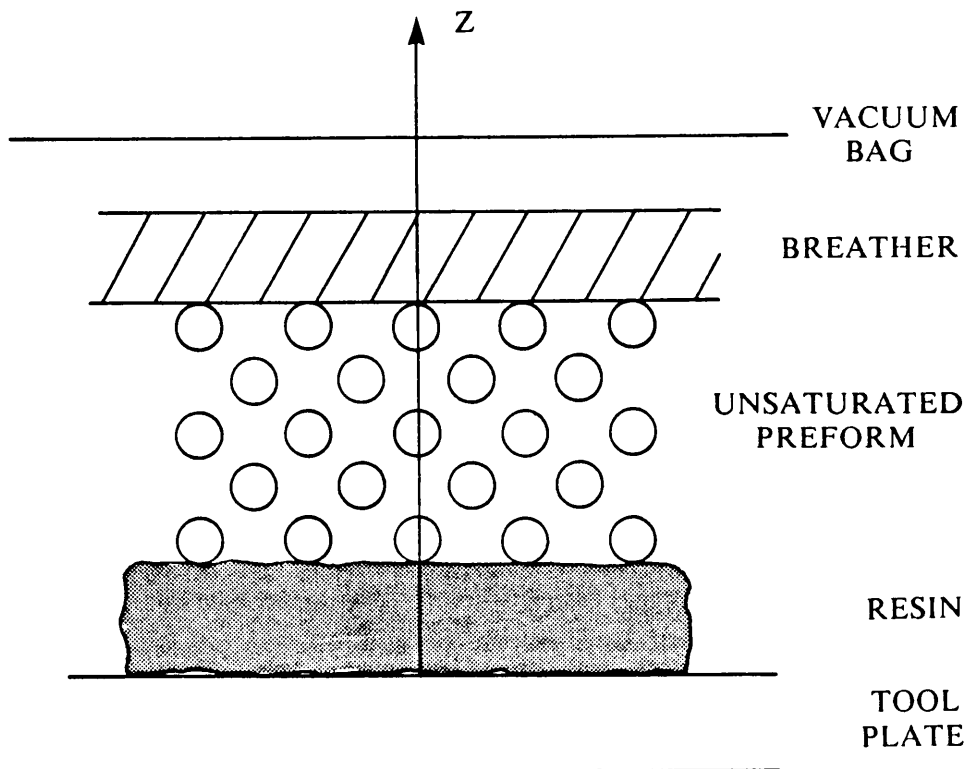


Figure 7. Vacuum bag schematic for discussion of the boundary conditions.

across the interface. For the tool-plate/composite interface ( $z = 0$ ), these conditions can be written as,

$$K_T \frac{\partial T_T}{\partial z} = K_c \frac{\partial T_c}{\partial z} \quad (5.2.4)$$

$$T_T = T_c \quad (5.2.5)$$

where the subscripts  $T$  and  $c$  refer to the tool plate and the composite respectively. For the composite-breather interface ( $z = l_c$ ) these conditions can be written as,

$$K_c \frac{\partial T_c}{\partial z} = K_b \frac{\partial T_b}{\partial z} \quad (5.2.6)$$

$$T_c = T_b \quad (5.2.7)$$

where the subscript  $b$  refers to the breather material.

When an autoclave is used to apply heat and pressure to the composite, the outer surfaces of the tool plate and the vacuum bag are subjected to forced convection from an environment which is at a uniform temperature  $T_a$ . Introducing the convective heat transfer coefficients  $h_T$  and  $h_O$  for the tool plate and the vacuum bag surfaces respectively, the boundary conditions can be written as follows,

$$K_T \frac{\partial T_T}{\partial z} = h_T (T_a - T_T) \quad \text{at } z = -l_T \quad (5.2.8)$$

$$K_O \frac{\partial T_O}{\partial z} = h_O (T_a - T_b) \quad \text{at } z = l_c + l_b \quad (5.2.9)$$

If a platen press is used to process the composite, the temperature at the boundaries  $z = -l_T$  and  $z = l_c + l_b$  will be equal to the applied cure temperature  $T_a$ .

Solution of D'Arcy's law (Equation 3.1.2) with the kinetics and viscosity models (Equations 4.2.4 - 4.2.6 and 4.3.3) subjected to proper the boundary conditions (Equations 5.2.1 - 5.2.3) will yield the position, viscosity, degree of cure, pressure, and velocity of the resin during infiltration. Solution for the transient heat transfer (Equations 4.1.2 and 4.1.3), subjected to convective and conductive boundary conditions (Equations 5.2.4 - 5.2.9) will yield the temperature, viscosity and degree of cure of the resin after infiltration.

### 5.3 FINITE ELEMENT FORMULATION

A finite element technique has been used to solve the infiltration problem in a quasi-steady state fashion. An analogy with the standard linear-elastic stress formulation can be used by defining a gradient vector  $\{g\}$  as follows,

$$\{g\} = \begin{bmatrix} \frac{\partial P}{\partial x} \\ \frac{\partial P}{\partial y} \end{bmatrix} \quad (5.3.1)$$

Incorporating this vector into D'Arcy's law, Equation 3.1.2 becomes,

$$\{v\} = [K] \{g\} \quad (5.3.2)$$

Hooke's law for elastic deformation can be written as,

$$\{\sigma\} = [C] \{\varepsilon\} \quad (5.3.3)$$

where  $\{\sigma\}$  represents the stress vector,  $\{\varepsilon\}$  represents the strain vector and  $[C]$  is a tensor of elastic coefficients. Equations 5.3.2 and 5.3.3 are the constitutive equations for the viscous flow and the elastic stress problems, respectively. If Equations 5.3.2 and 5.3.3 are written in terms of nodal values, the constitutive equations become,

$$\{v_i\} = [K][B]\{g_i\} \quad (5.3.4)$$

$$\{\sigma_i\} = [C][B]\{r_i\} \quad (5.3.5)$$

where  $[B]$  represents derivatives of the element interpolation functions,  $\{g_i\}$  represents the pressure gradients at the nodal points and  $\{r_i\}$  represents the nodal displacements. Since these equations are identical, the formulation of the finite element procedure is the same for the porous flow problem as for the linear elasticity problem.

Using the principal of minimum potential energy, the functional for the porous flow problem can be written as,

$$\chi = \frac{1}{2} \int_{\mathcal{V}} \{g\}^T \{v\} d\mathcal{V} - \int_S q \{N\}^T dS \quad (5.3.6)$$

where  $\{N\}$  represents a vector of the shape functions and  $q$  represents the externally applied loads on the surface  $S$ . Using the constitutive equation the functional becomes,

$$\chi = \frac{1}{2} \int_{\mathcal{V}} \{P_i\}^T [B]^T [K] [B] \{P_i\} d\mathcal{V} - \int_S q \{N\}^T \{P_i\} dS \quad (5.3.7)$$

where  $\{P_i\}$  represents a vector of nodal pressures.

Minimizing the functional results in the following system of simultaneous algebraic equations,

$$[\mathbb{Z}] \{P_l\} = \{Q\} \quad (5.3.8)$$

The global stiffness matrix  $[\mathbb{Z}]$ , and global load vector  $\{Q\}$ , are defined as follows,

$$[\mathbb{Z}] = \int_V [B]^T [K] [B] dV \quad (5.3.9)$$

$$\{Q\} = \int_S q \{N\}^T dS \quad (5.3.10)$$

The solution of this system of equations will yield the pressure at each node. A two-dimensional form of Equations 5.3.9 and 5.3.10 can be written in terms of a transformed coordinate system  $s$  and  $t$  ( $-1 \leq s, t \leq 1$ ) as follows,

$$[\mathbb{Z}] = \int_{-1}^1 \int_{-1}^1 [B]^T [K] [B] |J| ds dt \quad (5.3.11)$$

$$\{Q\} = \int_{-1}^1 \int_{-1}^1 q \{N\}^T |J| ds dt \quad (5.3.12)$$

where  $|J|$  is the determinant of the Jacobian transformation matrix which can be written in terms of the interpolation functions as follows,

$$|J| = x_i y_j (N_{i,s} N_{j,t} - N_{i,t} N_{j,s}) \quad (5.3.13)$$

where  $(x_i, y_i)$  are the global coordinates of the  $i^{\text{th}}$  node and  $\{N\}$  is written in terms of the transformed coordinates  $s$  and  $t$ .

A Gaussian integration technique was used to numerically integrate the system of governing equations. Gauss quadrature approximates an integral in the following manner,

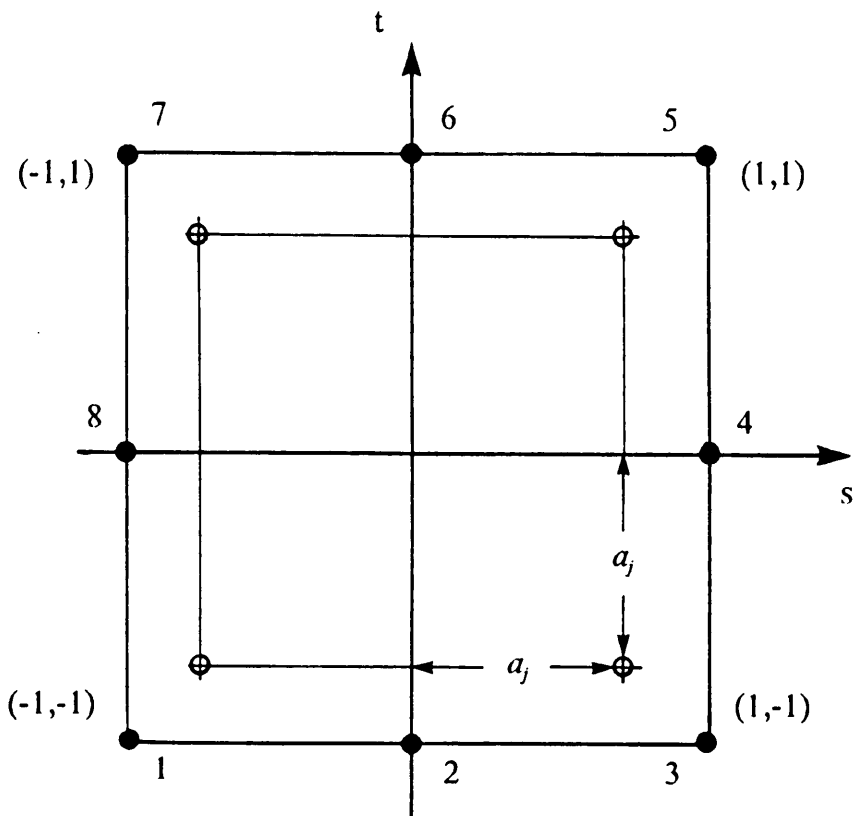
$$\int_{-1}^1 f(x) dx \doteq \sum_{j=1}^n H_j f(a_j) \quad (5.3.14)$$

where  $n$  is the total number of Gauss points (points at which the Gaussian integration technique is applied),  $H_j$  represents the weighting functions and  $f(a_j)$  is the integrand  $f(x)$  evaluated at Gauss point  $a_j$ . Finally, the stiffness matrix and load vector can be approximated as follows,

$$[Z] \doteq \sum_{i=1}^n \sum_{j=1}^n H_i H_j [B]^T [K] [B] |J| \quad (5.3.15)$$

$$\{Q\} \doteq \sum_{i=1}^n H_i q \{N\}^T |J| \quad (5.3.16)$$

An eight-node quadrilateral element was chosen for the solution of D'Arcy's law. The local nodal numbering scheme and the location of the integration points is shown in Figure 8. The interpolation functions for this element are as follows,



$$a_j = 0.57735$$

**Figure 8.** Eight-node quadrilateral element with the Gaussian integration points and the local nodal numbering scheme.

$$N_i = \frac{1}{4} (1 + ss_i) (1 + tt_i) (ss_i + tt_i - 1) \quad \text{for } i = 1, 3, 5, \text{ and } 7 \quad (5.3.17)$$

$$N_i = \frac{1}{2} (1 - s^2) (1 + tt_i) \quad \text{for } i = 2 \text{ and } 6 \quad (5.3.18)$$

$$N_i = \frac{1}{2} (1 - t^2) (1 + ss_i) \quad \text{for } i = 4 \text{ and } 8 \quad (5.3.19)$$

where  $s_i$  and  $t_i$  are the coordinates of the  $i^{th}$  node in the transformed space.

A two point Gaussian quadrature method was used to approximate the integration of the global stiffness matrix and the global load vector. In this case, the weighting functions are,

$$H_i = 1.0 \quad \text{for } 1 \leq i \leq n \quad (5.3.20)$$

To simulate the motion of the infiltration front, an element is added to the computational mesh at the end of each time step in the following manner,

$$\Delta z_{resin}(t_{i+1}) = \Delta t_i v_z(z_{resin}(t_i)) \quad (5.3.21)$$

where  $\Delta z_{resin}$  is the length of the element,  $\Delta t_i$  is the time step, and  $v_z(z_{resin}(t_i))$  is the velocity of the resin front at time  $t_i$ . Figure 9 is a logic diagram for the step-wise solution of the infiltration model.

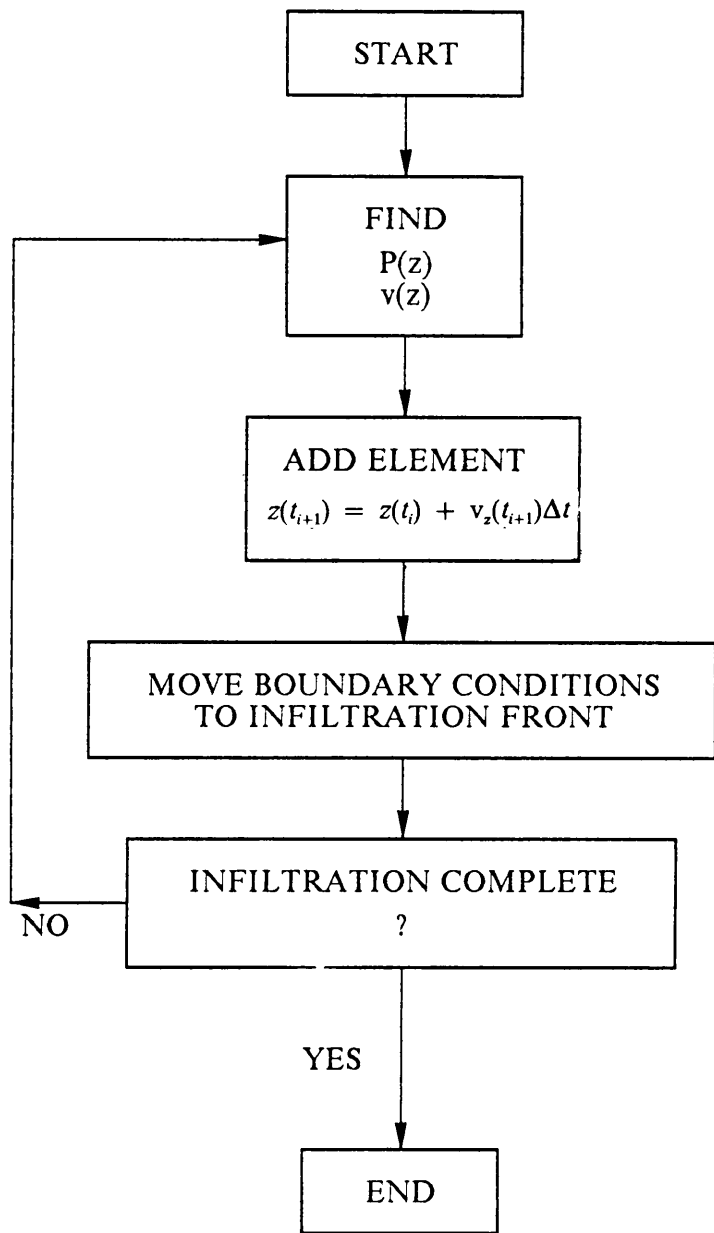


Figure 9. Logic diagram for the quasi-steady state infiltration process.

## 5.4 FINITE DIFFERENCE FORMULATION

A finite difference technique developed by Loos [30] was used to solve for the temperature in the composite during cure. A schematic of a typical finite difference grid is shown in Figure 10.

The heat transfer model requires the approximation of the three differential terms in Equation 4.1.3. The first time derivative is approximated by a forward difference technique and can be expressed as,

$$\rho C \frac{\partial T}{\partial t} \doteq \rho C \frac{T_j(t + \Delta t) - T_j(t)}{\Delta t} \quad (5.4.1)$$

for any node away from the boundaries  $z = -l_T$ ,  $z = 0$ ,  $z = l_c$  and  $z = l_c + l_b$ . The subscript  $j$  refers to the temperature at the  $j^{\text{th}}$  node. The density and specific heat of each material are assumed to be constant in space and time.

The space derivative in Equations 4.1.3 and 4.1.2 can be approximated by the following expression,

$$\begin{aligned} \frac{\partial}{\partial z} \frac{\partial T}{\partial z} &\doteq \frac{2T_{j+1}(t + \Delta t)}{\Delta z_n [\Delta z_n + \Delta z_{n-1}]} - \frac{2T_j(t + \Delta t)}{\Delta z_n \Delta z_{n-1}} \\ &+ \frac{2T_{j-1}(t + \Delta t)}{\Delta z_{n-1} [\Delta z_n + \Delta z_{n-1}]} \end{aligned} \quad (5.4.2)$$

where  $\Delta z_n$  is the distance between nodes  $j$  and  $j + 1$ .

In general, the last term in Equation 4.1.3 can be written as,

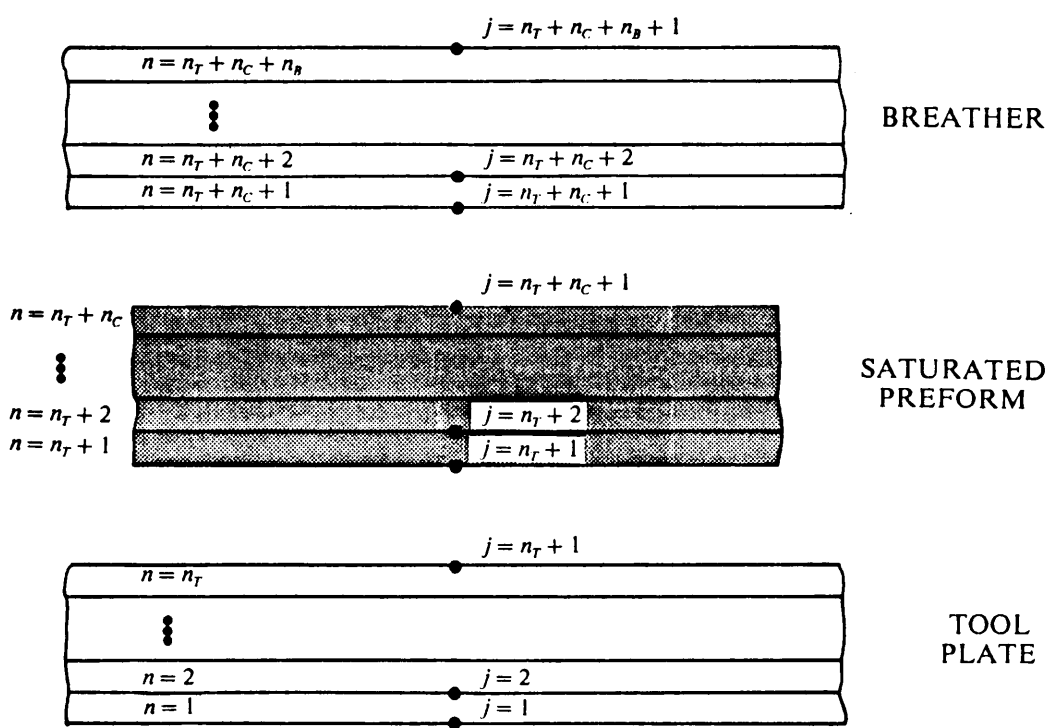


Figure 10. Finite difference grid for numerical solution of the heat transfer problem.

$$\rho_c \dot{H}_c = \rho_r v_r H_{Tr} \frac{\partial \alpha}{\partial t} \quad (5.4.3)$$

and in forward, finite difference notation as,

$$\rho_c \dot{H}_c \doteq \rho_r v_r H_{Tr} \frac{\alpha_j(t + \Delta t) - \alpha_j(t)}{\Delta t} \quad (5.4.4)$$

For Hercules 3501-6, the degree of cure at  $t + \Delta t$  can be determined by the following expressions

$$\begin{aligned} \alpha_j(t + \Delta t) &= \alpha_j(t) + [K_1(t + \Delta t) + K_2(t + \Delta t)\alpha_j(t)] \\ &\quad [1 - \alpha_j(t)] [B - \alpha_j(t)] \Delta t \end{aligned} \quad \text{for } \alpha_j(t) \leq 0.3 \quad (5.4.5)$$

$$\alpha_j(t + \Delta t) = \alpha_j(t) + K_3(t + \Delta t)[1 - \alpha_j(t)] \Delta t \quad \text{for } \alpha_j(t) > 0.3 \quad (5.4.6)$$

$$K_i(t + \Delta t) = A_i \exp\left(\frac{-\Delta E_i}{RT(t + \Delta t)}\right) \quad i = 1, 2, 3 \quad (5.4.7)$$

Equations 5.4.1, 5.4.2 and 5.4.3 can be combined to yield a system of  $n_c + n_t + n_b - 1$  equations in terms of the nodal temperatures as follows

$$\begin{aligned} \frac{\rho_i C_i}{K_i} \frac{T_j(t + \Delta t) - T_j(t)}{\Delta t} &= \frac{2T_{j+1}(t + \Delta t)}{\Delta z_n [\Delta z_n + \Delta z_{n-1}]} - \frac{2T_j(t + \Delta t)}{\Delta z_n \Delta z_{n-1}} \\ &+ \frac{2T_{j-1}(t + \Delta t)}{\Delta z_{n-1} [\Delta z_n + \Delta z_{n-1}]} \end{aligned} \quad (5.4.8)$$

for the tool plate and breather plies, and

$$\begin{aligned}
\frac{\rho_c C_c}{K_c} \frac{T_j(t + \Delta t) - T_j(t)}{\Delta t} &= \frac{2T_{j+1}(t + \Delta t)}{\Delta z_n [\Delta z_n + \Delta z_{n-1}]} - \frac{2T_j(t + \Delta t)}{\Delta z_n \Delta z_{n-1}} \\
&+ \frac{2T_{j-1}(t + \Delta t)}{\Delta z_{n-1} [\Delta z_n + \Delta z_{n-1}]} \\
&+ \frac{\rho_r v_r H_T}{K_c} \frac{\alpha_j(t + \Delta t) - \alpha_j(t)}{\Delta t}
\end{aligned} \tag{5.4.9}$$

for the composite.

The boundary conditions must be satisfied at the top and bottom of the tooling and at each interface where material properties change. Expressing the boundary conditions in finite difference notation, Equation 5.2.4 becomes,

$$\begin{aligned}
-\frac{K_T}{\Delta z_{n-1}} T_{j-1}(t + \Delta t) + \left[ \frac{K_T(1 + 2\alpha_{n-1}\lambda_{n-1})}{2\alpha_{n-1}\lambda_{n-1}\Delta z_{n-1}} + \frac{K_C(1 + 2\alpha_n\lambda_n)}{2\alpha_n\lambda_n\Delta z_n} \right] T_j(t + \Delta t) \\
-\frac{K_c}{\Delta z_n} T_{j+1}(t + \Delta t) = \left[ \frac{K_T}{2\alpha_{n-1}\lambda_{n-1}\Delta z_{n-1}} + \frac{K_c}{2\alpha_n\lambda_n\Delta z_n} \right] T_j(t) \\
+ \frac{K_c U_n(t + \Delta t) \Delta t}{2\alpha_n\lambda_n\Delta z_n}
\end{aligned} \tag{5.4.10}$$

where,

$$U_n(t + \Delta t) = \frac{\rho_r v_r h_r}{\rho_T C_p T} R(t + \Delta t)$$

$$n = n_T + 1 \quad j = n_T + 1$$

$$\alpha_{n-1} = \frac{K_T}{\rho_T C_T} \quad \lambda_{n-1} = \frac{\Delta t}{\Delta z_{n-1}^2}$$

$$\alpha_n = \frac{K_c}{\rho_c C_c} \quad \lambda_n = \frac{\Delta t}{\Delta z_n^2}$$

where  $R_n$  is the rate of reaction in region  $n$ , and Equation 5.2.6 becomes,

$$\begin{aligned}
 -\frac{K_c}{\Delta z_{n-1}} T_{j-1}(t + \Delta t) + \left[ \frac{K_c(1 + 2\alpha_{n-1}\lambda_{n-1})}{2\alpha_{n-1}\lambda_{n-1}\Delta z_{n-1}} + \frac{K_B(1 + 2\alpha_n\lambda_n)}{2\alpha_n\lambda_n\Delta z_n} \right] T_j(t + \Delta t) \\
 -\frac{K_B}{\Delta z_n} T_{j+1}(t + \Delta t) = \left[ \frac{K_c}{2\alpha_{n-1}\lambda_{n-1}\Delta z_{n-1}} + \frac{K_B}{2\alpha_n\lambda_n\Delta z_n} \right] T_j(t) \\
 + \frac{K_c U_j(t + \Delta t) \Delta t}{2\alpha_{n-1}\lambda_{n-1}\Delta z_{n-1}}
 \end{aligned} \tag{5.4.11}$$

where,

$$n = n_T + n_c + 1 \quad j = n_T + n_c + 1$$

$$\alpha_{n-1} = \frac{K_c}{\rho_c C_c}$$

$$\alpha_n = \frac{K_B}{\rho_B C_B}$$

At  $z = -l_t$  and  $z = l_c + l_b$  the heat flux boundary conditions, Equations 5.2.8 and 5.2.9, will become,

$$\begin{aligned}
 \left[ 1 + 2\alpha_n\lambda_n \left( 1 + \frac{h_T}{K_T} \Delta z_n \right) \right] T_j(t + \Delta t) - 2\alpha_n\lambda_n T_{j+1}(t + \Delta t) \\
 = 2\alpha_n\lambda_n \frac{h_T}{K_T} \Delta z_n T_a(t + \Delta t) + T_j(t)
 \end{aligned} \tag{5.4.12}$$

where,

$$n = 1 \quad j = 1$$

$$\alpha_n = \frac{K_T}{\rho_T C_T}$$

and

$$\begin{aligned} & \left[ 1 + 2\alpha_n \lambda_n \left( 1 + \frac{h_O}{K_B} \Delta z_n \right) \right] T_j(t + \Delta t) - 2\alpha_n \lambda_n T_{j-1}(t + \Delta t) \\ &= 2\alpha_n \lambda_n \frac{h_O}{K_B} \Delta z_n T_a(t + \Delta t) + T_j(t) \end{aligned} \quad (5.4.13)$$

where,

$$n = n_T + n_c + n_B \quad j = n_T + n_c + n_B + 1$$

$$\alpha_n = \frac{K_B}{\rho_B C_B}$$

## 5.5 COMPUTER PROGRAM INFIL

The infiltration and cure of a reactive resin in an anisotropic homogenous porous medium has been simulated by the infiltration and cure models. The governing equations have been numerically solved in the Fortran computer code INFIL. The infiltration equations are solved using the finite element method and the heat transfer equations are

solved using a finite difference method. Changes in the interstitial microstructure have been accounted for by changes in the material permeability tensor.

The necessary input parameters for INFIL are as follows:

**Problem Geometry:**

1. Length of the composite
2. Width of the composite
3. Initial finite element mesh geometry

**Solid Material Characteristics:**

1. Number of layers
2. Areal weight
3. Uncompacted thickness
4. Fiber diameter
5. Fiber density
6. Compaction coefficients
7. Kozeny-Carman coefficients

**Resin Characteristics:**

1. Resin Density
2. Kinetics coefficients
3. Viscosity coefficients

**Heat Transfer Characteristics:**

1. Number of divisions in the tool plate
2. Number of divisions in the composite
3. Number of divisions in the breather plies
4. Initial temperature
5. Total heat of reaction of the resin
6. Thermal conductivities of each material
7. Convective heat transfer coefficients of the boundary materials
8. Temperature history of the environment

The logic diagram shown in Figure 11, represents the general organization of the computer program INFIL.

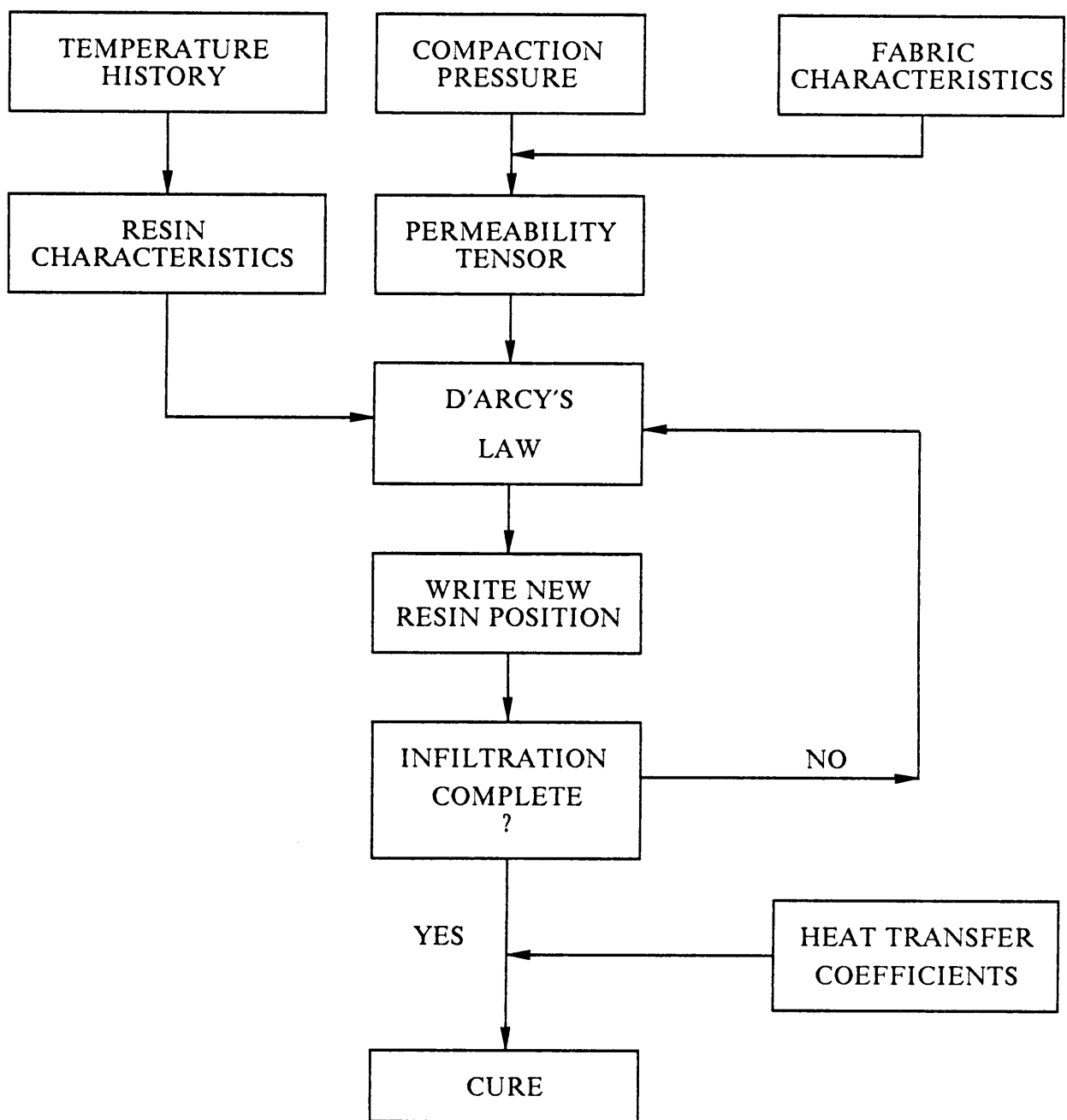


Figure 11. Logic diagram for computer program INFIL.

## **6.0 EXPERIMENTAL METHODS**

An experimental program was performed to obtain the input parameters for the process simulation model, to verify the model, and to compare the quality of laminates produced by the RTM manufacturing method to laminates produced with prepregged materials. The program consisted of three phases: an investigation of the compaction characteristics of reinforcing fabrics, through-the-thickness and in-plane permeability experiments at various compaction pressures, and mechanical characterization of cured laminates. Each phase of the experimental program will be discussed on the basis of the equipment used to perform the test, preparation of test specimens, testing procedures, and analysis of the experimental data.

### **6.1 MATERIALS**

Two reinforcing materials and three resin systems were used for the experimental program. Preliminary compaction experiments were performed on an eight-harness-satin fabric, woven from 3000 filament tows of Celion carbon fiber (C3k/8HS). This fabric

was woven by Textile Products Inc. with 24 tows per unit length in the warp direction and 23 tows per unit length in the fill direction. The balance of the experimental program was performed with a material constructed from 6000 filament tows of Hercules IM7 fiber woven in an eight-harness-satin pattern by Textile Technologies Inc. (IM7/8HS). The IM7 fabric was constructed with 23 tows in the warp direction and 23 tows in the fill direction. Mechanical properties determined during this study were compared to laminate properties of an eight-harness satin fabric woven from 3000 filament tows of Hercules AS4 fiber (AS4/8HS). This material consisted of 19 tows in each of the warp and fill directions. Table 1 contains additional characteristics of each fabric.

Laminates were manufactured to validate the RTM process simulation model and to compare the elastic mechanical properties to laminates produced from prepregged fabrics. The IM7/8HS fabric was infiltrated and cured with either Hercules 3501-6, Hercules 8551-2, or Shell RSL 1282/9470 resin systems. Hercules 3501-6 is a common thermosetting resin system which has the consistency of a tacky solid in its B-staged, room temperature form. Hercules 8551-2 is also a high viscosity resin with base resin characteristics similar to the 3501-6 resin system. Shell RSL 1282/9470 is a low viscosity, two part, thermosetting resin consisting of research resin RSL 1282 and Epon Curing Agent® 9470. When mixed with 32.4 percent by mass of curing agent (32.4 phr) at room temperature, this resin has the consistency of room temperature honey and is intended to be used for filament winding and RTM.

**Table 1. Fabric Properties.**

**Textile Products C3k/8HS Style 4245**

Areal Weight	0.370 Kg/m <sup>2</sup>
Fiber Diameter	$7 \times 10^{-6}$ m
Fiber Density	$1.77 \times 10^3$ Kg/m <sup>3</sup>
Uncompacted Thickness	$6.10 \times 10^{-4}$ m

**TTI IM7/8HS Style X-1226**

Areal Weight	0.422 Kg/m <sup>2</sup>
Fiber Diameter	$5 \times 10^{-6}$ m
Fiber Density	$1.78 \times 10^3$ Kg/m <sup>3</sup>
Uncompacted Thickness	$6.83 \times 10^{-4}$ m

**Hercules AS4/8HS Style A\*370-8H**

Areal Weight	0.370 Kg/m <sup>2</sup>
Fiber Diameter	$8 \times 10^{-6}$ m
Fiber Density	$1.80 \times 10^3$ Kg/m <sup>3</sup>
Cured Thickness	$3.40 \times 10^{-4}$ m

## 6.2 COMPACTION EXPERIMENTS

The goal of the compaction experiments was to describe the load-deflection behavior of common textile reinforcements. During RTM the dry reinforcement is compacted to force the resin into the fiber bundles and to increase the fiber volume fraction. To describe the deformation with Equation 3.2.2, the compaction coefficients,  $a_i$ , zero pressure,  $P_{zero}$ , and the order of the polynomial must be determined for each material and each load cycle.

### 6.2.1 Test Equipment

A fixture was constructed to contain the fabric while applying a uniform compaction pressure to the test specimen. The fixture consisted of male and female halves with a test section measuring 153 by 172 mm. A plexiglass window was placed in one side of the fixture so that the relative position of the plunger and fabric could be observed during the experiment. A schematic of the test fixture is shown in Figure 12.

Compressive loads were applied by an Instron model 1321 multi-axial testing machine. So that the weight of the male half of the fixture would not affect the test results, it was suspended from the upper grip on the testing machine by four threaded rods. The female portion of the fixture was placed on a 9.5 mm thick aluminum plate to spread the applied load over a larger area. Figure 13 is a photograph of the fixture mounted in the testing machine during an experiment. Values of the load were measured by the load cell in the testing machine and the displacement of the fabric and fixture was measured by a Linear Voltage Displacement Transducer (LVDT) mounted to the lower actuator.

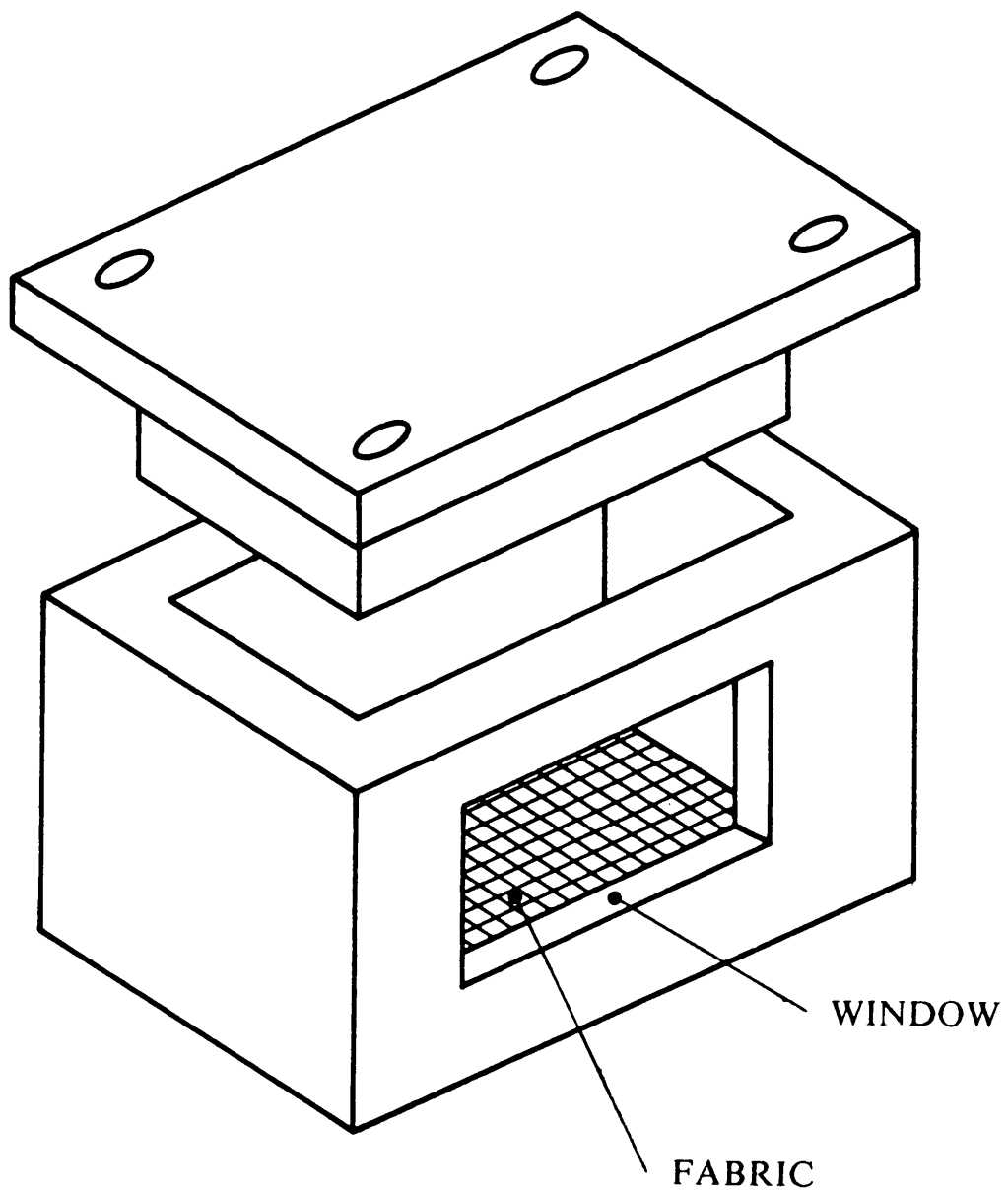
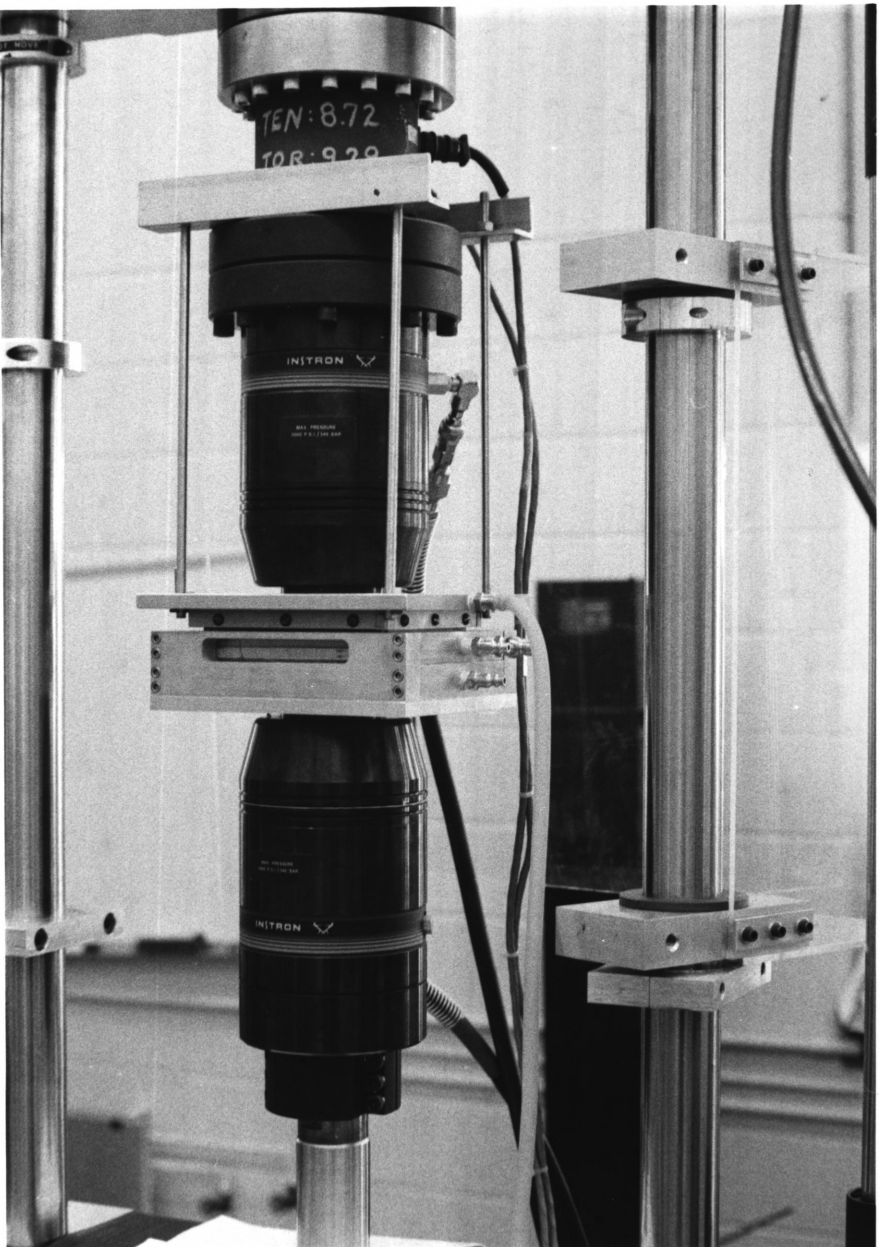


Figure 12. Schematic representation of the test fixture used for the compaction experiments.



**Figure 13.** Test fixture mounted in the Instron model 1321 multi-axis testing machine.

An IBM personal computer was used to record the experimental loads and displacements.

### **6.2.2 Sample Preparation**

Test specimens were oriented so that the 172 mm specimen edge was parallel to the warp or roll direction. Prior to cutting the fabric, the material was adjusted so that the individual tows in the warp and fill directions were straight and so that the fill tows were perpendicular to the warp tows. Correct alignment was maintained during cutting by taping the selvage to the cutting surface as shown in Figure 14.

### **6.2.3 Procedure**

The specified number of plies were placed in the test fixture after stray tows were removed from the edge of the specimen. Proper placement of each layer is important since careless specimen preparation will adversely affect the displacement results due to macroscopic ply bending. The fixture was closed until the bottom surface of the plunger was approximately 2 mm from the top of the fabric. The load cell and displacement transducer were zeroed at this stage of the experiment.

The fabric was compressed at a constant displacement rate of 1.3mm/min. When the load on the fabric and fixture reached 36 kN, the motion of the actuator was reversed and the fabric was unloaded at the same rate. A compressive load of 36 kN on a 153 by 172 mm specimen will produce a compaction pressure of approximately 1400 kPa

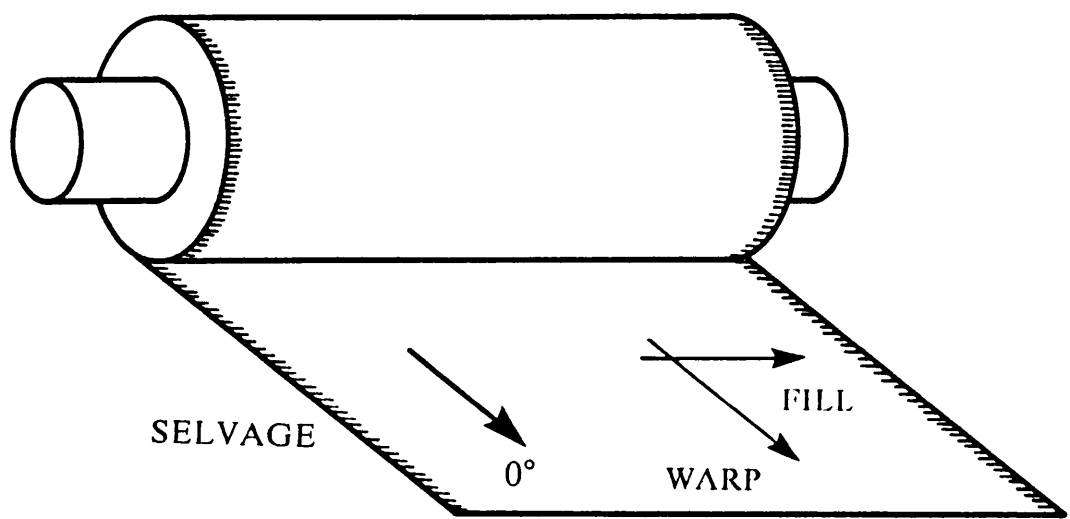


Figure 14. Fabric geometry and directions used for sample preparation.

which is the maximum typical processing pressure for thermosetting matrix composites. Each specimen was loaded and unloaded four times to examine the recompaction behavior of the materials.

#### 6.2.4 Data Analysis

Several tests were conducted without fabric to determine the deflection characteristics of the fixture. Since the displacement transducer was zeroed before load was applied the data was adjusted as follows,

$$d_{\text{fix}} = d_{\text{data}} - C \quad (6.2.1)$$

were  $d_{\text{data}}$  represents the deflection data as measured in the testing machine,  $d_{\text{fix}}$  represents the adjusted fixture deflection and  $C$  is a constant. Next, the adjusted deflection was fit with Equation 3.2.1 by a least squares procedure. The order of the polynomial was chosen so that the curve fit was visibly accurate and the correlation coefficient was at least 95 percent.

The measured data for the fabric and fixture were zeroed in the same manner as for the fixture alone. Values of measured load were used with the fixture deflection equation to obtain the contribution of the fixture to the total deflection. Deflection of the fabric was calculated as follows,

$$d_{\text{matl}} = d_{\text{data}} - d_{\text{fix}} \quad (6.2.2)$$

were  $d_{\text{matl}}$  represents the deflection of the fabric and  $d_{\text{data}}$  is the zeroed deflection of the fabric and fixture. Adjusted fabric deflection data was fit with Equation 3.2.1 and the

order of the polynomial was chosen in the same manner as for the fixture deflection equation.

The value of  $P_{\text{zero}}$  required for Equation 3.2.2 was determined by comparing the deflection and pressure-porosity relationships. Using the uncompacted thickness, the porosity can be calculated by Equation 3.2.13 and compared to the porosity calculated using the deflection model.  $P_{\text{zero}}$  is the magnitude of the compressive load which forces the porosities to match at approximately 7 kPa.

### 6.2.5 Wet Compaction

Compaction experiments were conducted to determine if the presence of a saturating liquid would affect the deformation behavior of a textile reinforcement. Changes to the proceeding experiment involved the configuration of the fixture and preparation of the specimen. The fixture was modified by mounting a porous plate on the loading surface of the plunger. Fluid displaced from the fabric was allowed to flow through the porous plate, into a reservoir, and if necessary, into an overflow tank. The specimen was pre-wetted with fluid in a large tub to remove any trapped air. The wet material was placed within the fixture and extra fluid was added to completely cover the material. Loading rate, procedure, data collection, and analysis were identical to the dry compaction experiments. All tests used tap water as the saturating fluid.

## **6.3 PERMEABILITY EXPERIMENTS**

The objective of the permeability experiments was to investigate the validity of D'Arcy's law and the Kozeny-Carman expression, and to measure the Kozeny-Carman constant for flow through a woven fabric. Results from the compaction experiments and the pressure-porosity relation were used to calculate the material porosity. To determine the Kozeny-Carman constant the measured permeabilities were compared with the calculated porosities. Tests were conducted in the through-the-thickness and inplane flow directions.

### **6.3.1 Test Equipment**

The test fixture, Instron multiaxial testing machine and a variety of plumbing equipment were used to perform the permeability experiments. For the through-the-thickness experiments the fixture was configured with porous plates immediately above and below the fabric. Reservoirs behind each plate allowed the vorticity in the fluid to dissipate before reaching the fabric and provided a position where the pressure could be measured. A cross-sectional view of the fixture, showing the position of important components, is shown in Figure 15. The O-ring was used to seal the upper and lower halves of the fixture.

The plumbing equipment used during the permeability experiments consisted of three major elements: a weighing tank manufactured by Techquipment Inc., a bubble-type flow meter manufactured by The Matheson Co. Inc., and a U-tube manometer. The weighing tank was used to contain and recirculate the test fluid. The flow meter contains

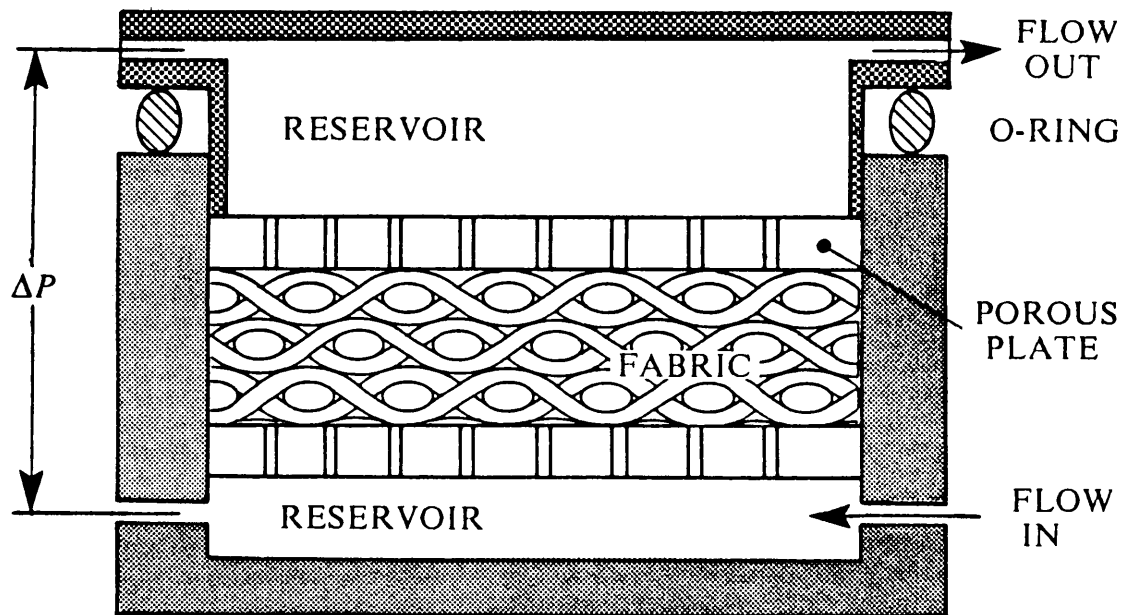


Figure 15. Cross-sectional view of the test fixture configured for through-the-thickness permeability experiments.

a needle valve and was used to measure and regulate the volumetric flow rate. Pressure drops across the fixture and fabric were measured with the U-tube manometer. These devices were connected together and to the test fixture by plastic tubing. Figure 16 is a schematic drawing of how the weighing tank, flow meter, manometer, fixture, and Instron testing machine were assembled for this experiment.

### **6.3.2 Sample Preparation**

Individual fabric layers were cut from the bulk fabric in a manner similar to the compaction experiments. Each layer of fabric was saturated with fluid as it was added to the test fixture. Tap water was used as the test fluid for all permeability experiments.

### **6.3.3 Procedure**

The exit tube was adjusted to the same level as the upper reservoir. This forced the pressure in the reservoir to be atmospheric pressure and allows the greatest sensitivity when measuring the pressure drop.

The flow meter was calibrated to relate the height of the steel ball in the tapered tube to the volumetric flow rate. A constant flow rate was established through the flow meter. The position of the steel ball and the time required to fill a graduated cylinder were recorded.

The Instron testing machine was calibrated to measure the thickness of the fabric directly by placing the fixture into the machine without fabric or O-ring. A small

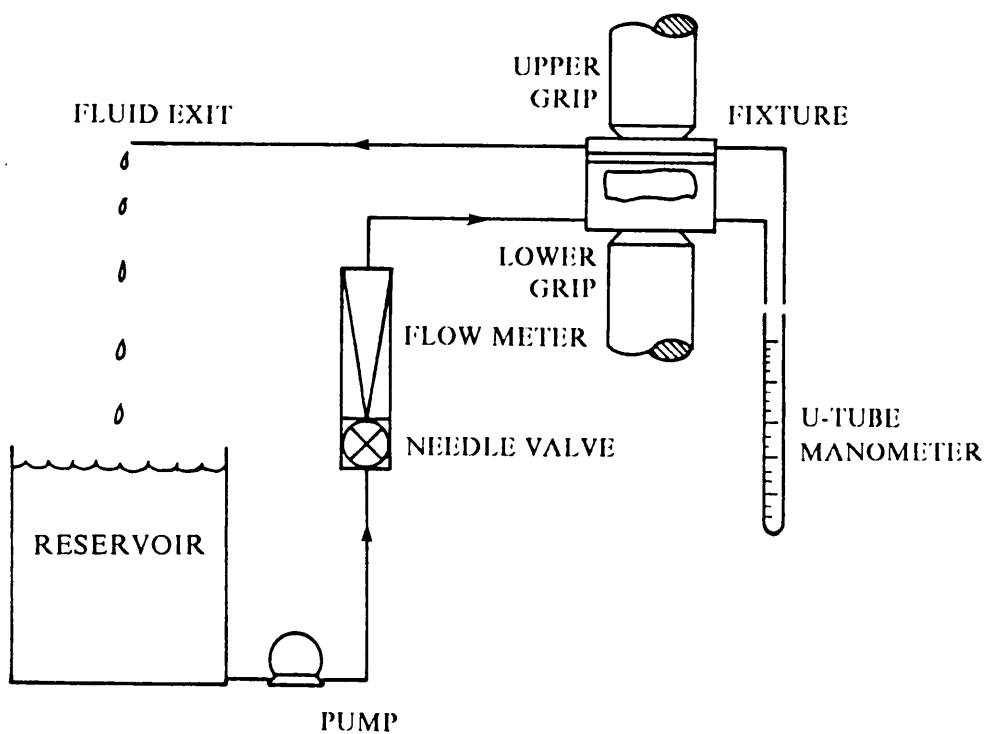


Figure 16. Plumbing schematic of equipment used for the permeability tests.

compressive load (approximately 5N) was applied to the fixture, and the displacement transducer was zeroed. This procedure established a zero fabric thickness when the fixture was empty and nearly unloaded.

Several flow experiments were conducted without a fabric specimen to estimate the energy lost due to flow through the fixture. The O-ring was installed in the fixture, and the trapped air was allowed to escape as the fixture was filled with water. The flow was stopped, and the pressure in the manometers was equilibrated with the atmosphere. A constant flow rate was established through the fixture, and the pressure drop and the position of the steel ball were recorded. This process was repeated for additional increments of flow rate until the maximum possible flow rate was achieved. The flow rate-pressure drop data was obtained for several values of the gap between the porous plates.

Fabric permeabilities were measured in a manner similar to the previous experiment. Fabric specimens were saturated with water, placed in the test fixture and the fixture was sealed against the O-ring. Trapped air was removed by allowing a small amount of fluid to flow through the fabric. The fixture was then placed in the testing machine, and the manometers were adjusted. A compressive load was applied to the fabric by adjusting the relative position of the grips on the testing machine. Pressure drops and flow rates were recorded for approximately six different values of fabric thickness.

#### 6.3.4 Data Analysis

To relate the position of the steel ball in the flow meter to the volumetric flow rate, the following expression was used,

$$q = c_1 + c_2 q' \quad (6.3.1)$$

where  $q$  represents the measured volumetric flow rate,  $c_i$  are calibration constants, and  $q'$  represents the position of the steel ball in the tapered tube.

Minor energy losses within the fixture were compensated for by converting the difference in height of water in the manometer into a pressure gradient. If  $\gamma_{fl}$  represents the specific weight of the test fluid, the pressure gradient can be written as,

$$\frac{dP}{dx}_{fix} = \frac{\gamma_{fl} \Delta l}{t_{gap}} \quad (6.3.2)$$

where  $\Delta l$  represents the difference in height of fluid in the manometers, and  $t_{gap}$  represents the spacing between the porous plates. Experimental flow rates were related to the calculated pressure gradient by a first order polynomial of the form,

$$\frac{dP}{dx}_{fix} = a_1 + a_2 q \quad (6.3.3)$$

where  $q$  represents the flow rate determined from the position of the steel ball and Equation 6.3.1, and the constants  $a_i$  were determined by a least squares procedure. Equation 6.3.3 was modified slightly to account for an increased dependence on the fixture gap by allowing the values of  $a_i$  to vary linearly with the gap.

The gap distances measured during the experiments with fabric were modified to account for the deformation of the fixture. Data from the wet fabric compression tests were fit with the following expression to obtain the compressive load on the fabric and fixture.

$$\ln P = c_0 + c_1 d + c_2 d^2 + c_3 d^3 + \dots \quad (6.3.4)$$

The load cell value was not used due to the presence of the O-ring.

Applied load values from Equation 6.3.4, the uncompacted thickness, and the measured thickness of the fabric were used with Equation 3.2.1 to determine the deflection of the fixture. The measured thickness values were modified to reflect the actual thickness of the fabric by,

$$t_{\text{fabric}} = t_{\text{measured}} + d_{\text{fix}} \quad (6.3.5)$$

Equation 6.3.2 was used with measured heights in the manometers and the adjusted fabric thickness to calculate the pressure gradient across the fixture and fabric. Using the experimental flow rate and Equation 6.3.3 to determine the drop in pressure across the empty fixture, the pressure gradient across the fabric can be calculated as follows,

$$\frac{dP}{dx}_{\text{fabric}} = \frac{dP}{dx}_{\text{measured}} - \frac{dP}{dx}_{\text{fix}} \quad (6.3.6)$$

where  $\frac{dP}{dx}_{\text{fabric}}$  represents the adjusted pressure gradient across the material and  $\frac{dP}{dx}_{\text{measured}}$  represents the measured pressure gradient.

Relating the measured flow rate to the pressure gradient with the expression,

$$q = b_1 - b_2 \frac{dP}{dx}_{\text{fabric}} \quad (6.3.7)$$

the fabric permeability and validity of D'Arcy's law can be determined. If flow through the fabric follows D'Arcy's law, the constant  $b_1$  should be nearly zero and the permeability can then be written as,

$$K = \frac{b_2 \mu_{\text{fl}}}{A} \quad (6.3.8)$$

where  $A$  represents the area normal to the flow.

To determine the Kozeny-Carman constant, the permeability values and the actual fabric thickness were used. Using Equation 3.2.13, the thickness of the fabric, and the properties from Table 1, the porosity can be calculated. A least squares procedure was used to relate the measured permeability to the porosity with Equation 3.2.18 thus determining the Kozeny-Carman constant.

### 6.3.5 In-Plane Permeability

Measurements of the in-plane permeabilities were attempted by following the procedures used for the through-the-thickness experiments. The only significant differences in the two experiments involves the fixture configuration. The porous plates that contacted the fabric in the previous experiment were replaced with solid plates, and the sides of the fixture were fitted with porous plates as shown in Figure 17. The porous plates border reservoirs that contain openings for the introduction of fluid and for pressure measurements. Analysis of the experimental data was performed in a manner similar to the analysis of the through-the-thickness experiments.

## 6.4 MECHANICAL PROPERTIES

The goal of this experimental program was to measure the elastic material properties and volume fractions of several laminates produced by RTM and to compare these properties to laminates fabricated from prepregged materials. Material properties examined in

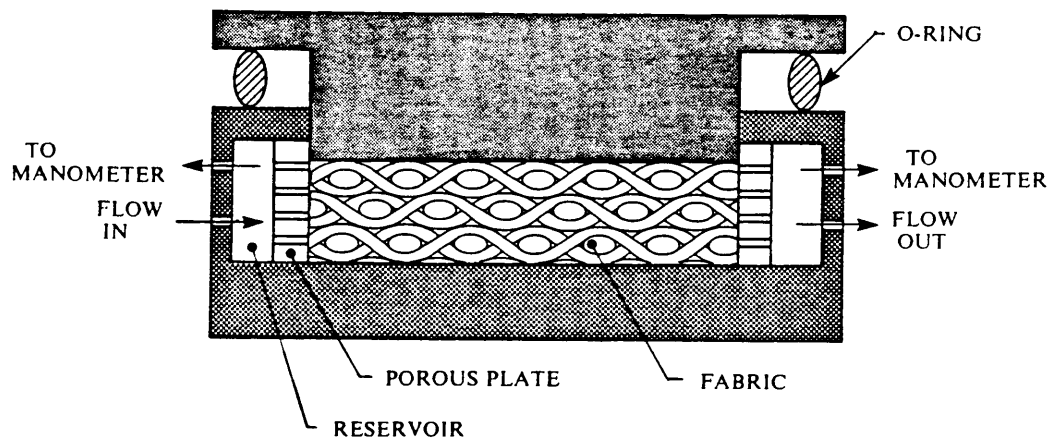


Figure 17. Test fixture configured for the in-plane permeability tests.

this study included the tensile and compressive values of Young's modulus, Possion's ratio, and ultimate stress and strain. Procedures, sample preparation, and data analysis to be discussed will focus on the methods unique to this experimental program.

#### **6.4.1 Test Equipment**

The equipment used to produce laminates by RTM was identical to the equipment used for prepreg laminate production. Standard vacuum bag materials were used with a heated-platen press and a portable vacuum pump. The equipment used to produce, machine and test the laminates is located at the NASA Langley Research Center.

#### **6.4.2 Sample Preparation**

The vacuum bag infiltration technique, discussed in Chapter 5, was used with 16 plies of IM7/8HS fabric to produce two laminates with Hercules 3501-6 and one laminate with Hercules 8551-2. Shell RSL 1282/9470 was used to produce one laminate reinforced with eight plies of IM7/8HS fabric. Laminates measured 203 by 343 mm and all fabric layers were oriented with the warp direction parallel to the long edge of the laminate ( $0^\circ$  direction). Sub-groups, of four plies each, were stitched in the  $0^\circ$  direction with polyester thread approximately 35 mm from the edge of the fabric. The stitching was used to maintain the orientation of the fabric during processing.

The typical vacuum bagging sequence used in this study was slightly more complex than shown in Figure 7. A layer of nonporous release film was used under the resin to facil-

itate post-cure clean up. Edge dams were used to prevent lateral motion of the resin and fabric. One layer of porous release film was used on top of the fabric to allow the air within the fabric, and any excess resin, to escape from the laminate during processing. Several layers of breather material were used to cover the laminate and edge dams. This bagging sequence is shown schematically in Figure 18. Intersections between the different bagging materials were taped to help force the resin through the fabric.

Different handling procedures were required to prepare each resin for infiltration and cure. The Shell RSL 1282/9470 resin was mixed in the proportion of 32.4 phr by mass and degassed in a vacuum chamber for 30 minutes. The resin was then carefully poured into the region bounded by the edge dams. The Hercules 3501-6 and 8551-2 resins required a slightly different procedure. While frozen, the resin was broken into small pieces so that an accurate measurement of the resin mass could be made. The resin was then allowed to warm to room temperature in a plastic bag before weighing to minimize condensation of moisture on the resin. After weighing, the resin was heated until it spread into a uniform layer. Uneven infiltration resulted if the resin is not uniformly distributed before final processing.

The first 3501-6 laminate (Laminate 4228) was produced by heating the system from room temperature at 2.5°C/min to 65°C and applying 687 kPa and full vacuum (-100 kPa) to compact the fabric and force the resin to flow. After the temperature and pressure were held for one hour, the vacuum bag was opened to check the degree of infiltration. Dry spots were observed on the laminate so the system was heated to 93°C and held for an additional 30 minutes. The fabric was saturated during the second attempt, so the manufacturer's recommended cure cycle was initiated. Nonporous release film

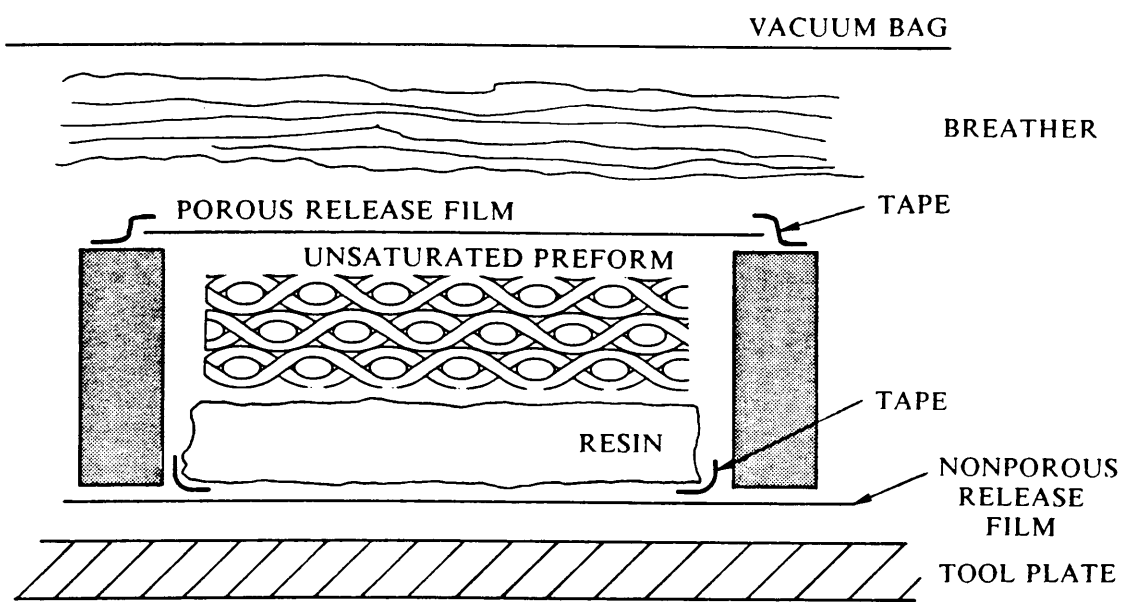


Figure 18. Typical vacuum bag infiltration schematic for production of cured laminates.

was used on both sides of this laminate to help contain the resin. After cooling, the laminate was removed from the platen press and prepared for further testing.

Laminate 4268 was also manufactured with Hercules 3501-6. Infiltration was attempted for 30 minutes at 93°C and 687 kPa of external pressure and full vacuum. When the vacuum bag was opened, the corners of the laminate were dry, so the process was repeated for an additional 30 min. A porous release material and several bleeder plies were used on top of the graphite cloth to allow the excess resin to flow away from the laminate before the resin gelled.

Hercules 8551-2 resin was used to infiltrate Laminate 5118 by heating the system to 120°C and holding for 30 minutes while a vacuum pressure of -100 kPa was applied. Infiltration was completed during the first attempt and the remainder of the cure cycle was performed with an additional applied pressure of 685 kPa.

The last laminate used for the mechanical characterization experiments (Laminate 5238) was constructed from Shell RSL 1282/9470 resin. The resin was heated to 65°C for infiltration and held for 15 minutes while being compacted with full vacuum pressure. The fabric was infiltrated during this time, so the manufacturer's cure cycle was initiated. An additional external pressure of 100 kPa was applied after approximately 90 minutes of the manufacturer's recommended cure cycle.

After cure, panels were nondestructively examined with ultrasonic, gray scale C-scans and photomicroscopy, then machined into tension and short-block compression specimens. The cutting diagram used for this study is shown in Figure 19.

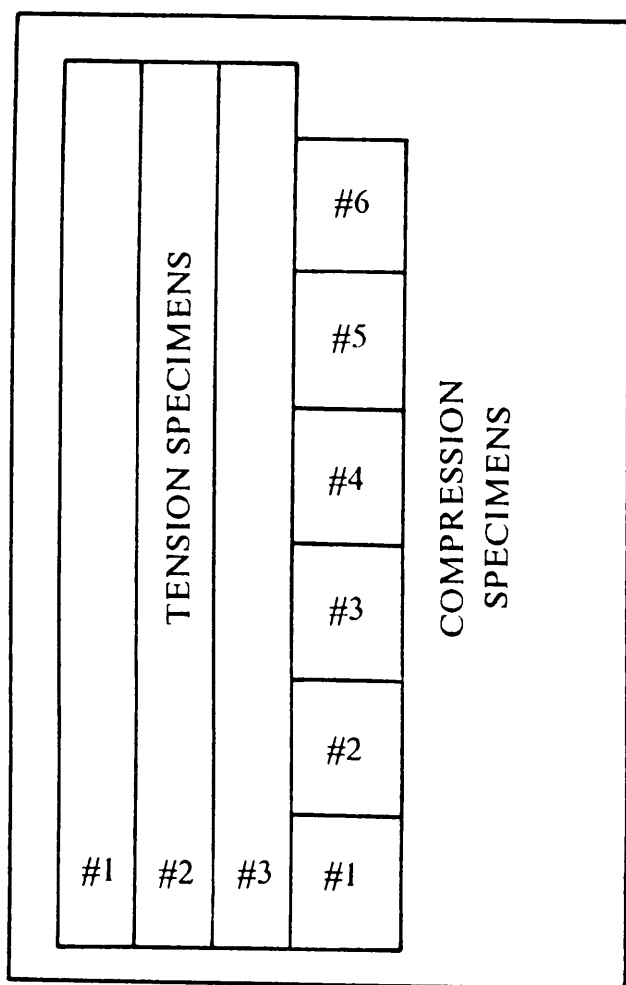


Figure 19. Cutting Diagram for the cured laminates.

### **6.4.3 Testing Procedures**

Test specimens were instrumented and tested to failure according to the procedures described in NASA RP-1092 [31] and NASA RP-1142 [32]. Three specimens from the unused portion of the cured laminate were used to determine the fiber volume fraction. An acid digestion technique was used to perform this test.

### **6.4.4 Data Analysis**

Analysis of the experimental data involved determination of Young's modulus, Possion's ratio and the stress and strain at failure. The values of Young's modulus and Possion's ratio were determined at 0.2 percent strain.

## **7.0 EXPERIMENTAL RESULTS AND DISCUSSION**

This chapter discusses the results of the experimental programs described in Chapter 6. Dry compaction of C3k/8HS and IM7/8HS fabrics were studied as a function of the number of plies and load history. Wet compaction experiments were performed on the IM7/8HS fabric. Permeability values were obtained using five plies of IM7/8HS and compared to literature experimental values and the Kozeny-Carman expression. Cured laminates were nondestructively examined by ultrasonic, gray-scale C-scans and by photomicroscopy. Values of volume fraction, tensile and compressive elastic modulus, ultimate strength, Poission's ratio, and ultimate strain were determined and compared to manufacturer's test values for AS4/8HS fabric prepregged with Hercules 3501-6.

## 7.1 COMPACTION

The goal of the compaction experiments was to characterize the deflection of woven textile materials when loaded in compression. Deflection of woven textiles is attributed to a combination of three actions; macroscopic ply flattening, motion of the fiber tows and distortions of individual tows. The material behavior was examined with regard to the loading path, previous loading history, number of plies, and type of fabric. A summary of the compaction experiments performed during the course of this study is shown in Table 2.

### 7.1.1 Dry Compaction Preliminaries

To accurately describe the deflection of the woven materials, the load-deflection behavior of the empty test fixture was required. The fixture was cycled three times between 0 and 1400 kPa while data for each cycle were recorded during loading and unloading. All loading and unloading paths of the empty fixture, were identical. The experimental data was adjusted with Equation 6.2.1 and fit with the following polynomial,

$$d_{\text{fix}} = a_0 + a_1 \ln P + a_2 (\ln P)^2 + a_3 (\ln P)^3 + a_4 (\ln P)^4 \quad (7.1.1)$$

where,

**Table 2. Dry Compression Test Matrix.**

Material	Number of Plies	Number of Samples
Fixture	-	3
C3k/8HS	1	3
	3	3
	5	3
IM7/8HS (dry)	5	2
IM7/8HS (wet)	5	2

$$\begin{aligned}
 a_0 &= 2.314 \times 10^{-5} \text{ m} \\
 a_1 &= -7.606 \times 10^{-6} \text{ m/N} \\
 a_2 &= 8.866 \times 10^{-7} \text{ m/N}^2 \\
 a_3 &= -3.383 \times 10^{-8} \text{ m/N}^3 \\
 a_4 &= 4.867 \times 10^{-10} \text{ m/N}^4
 \end{aligned}$$

Experimental data and Equation 7.1.1 are shown in Figure 20. The accuracy of the curve fit is acceptable for all values of the load.

### 7.1.2 Dry Compaction

The C3k/8HS fabric specimens were compressed in the test fixture as described in Section 6.2. Load-deflection results for the first loading cycle of five plies of fabric and the test fixture were zeroed with Equation 6.2.1 and are shown in Figure 21. Equations 6.2.2 and 7.1.1 were used to account for the deflection of the fixture. The contribution of the fixture to the total deflection is shown in Figure 22. Adjusted deflection values exhibit considerable stiffening at rates which change with the applied load.

A third order form of Equation 3.2.1 was chosen to describe the loading and unloading paths of C3k/8HS. The initial loading cycle can be expressed mathematically as follows,

$$d_{\text{matl}} = a_0 + a_1 \ln P + a_2 (\ln P)^2 + a_3 (\ln P)^3 \quad (7.1.2)$$

when loading,

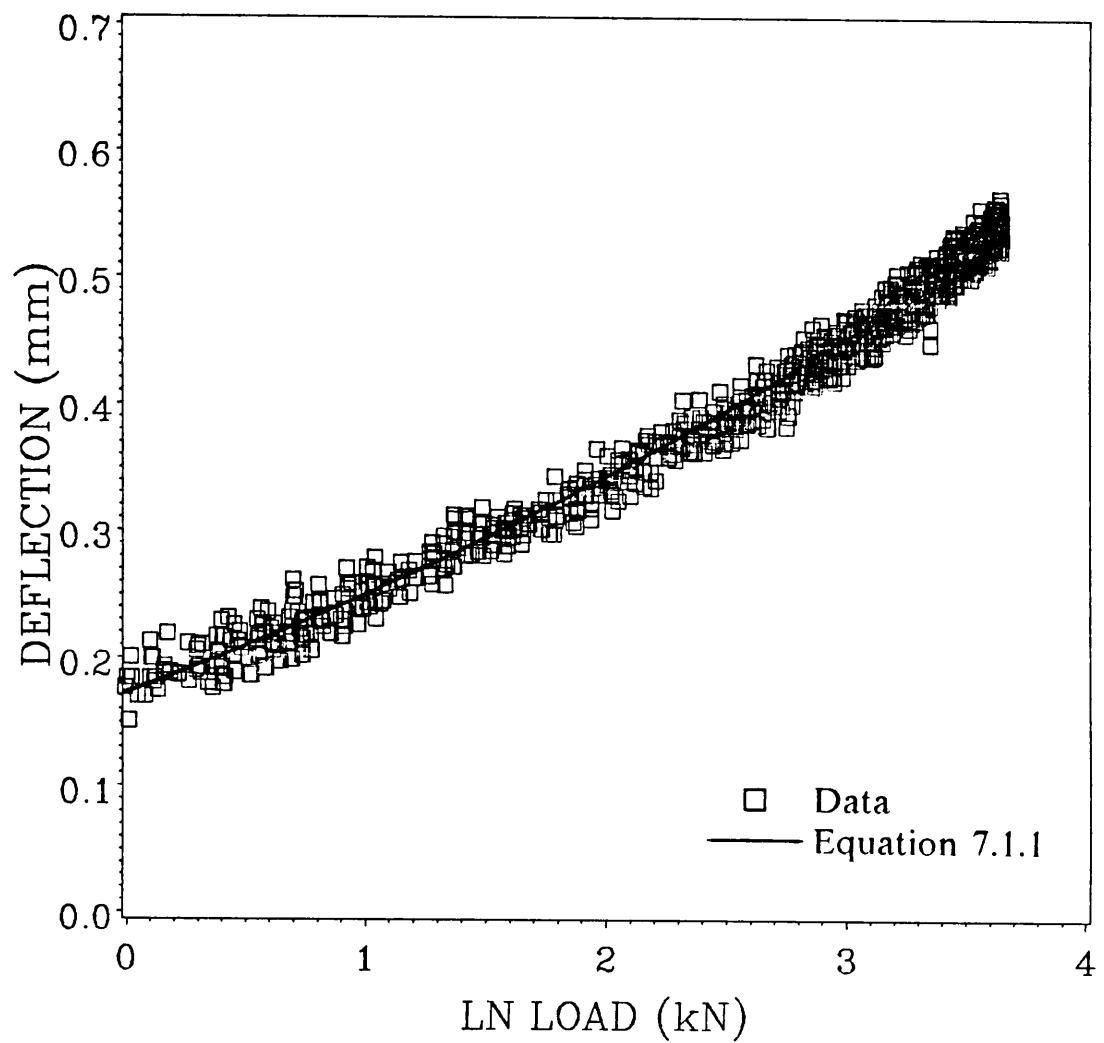


Figure 20. Experimental fixture data and Equation 7.1.1.

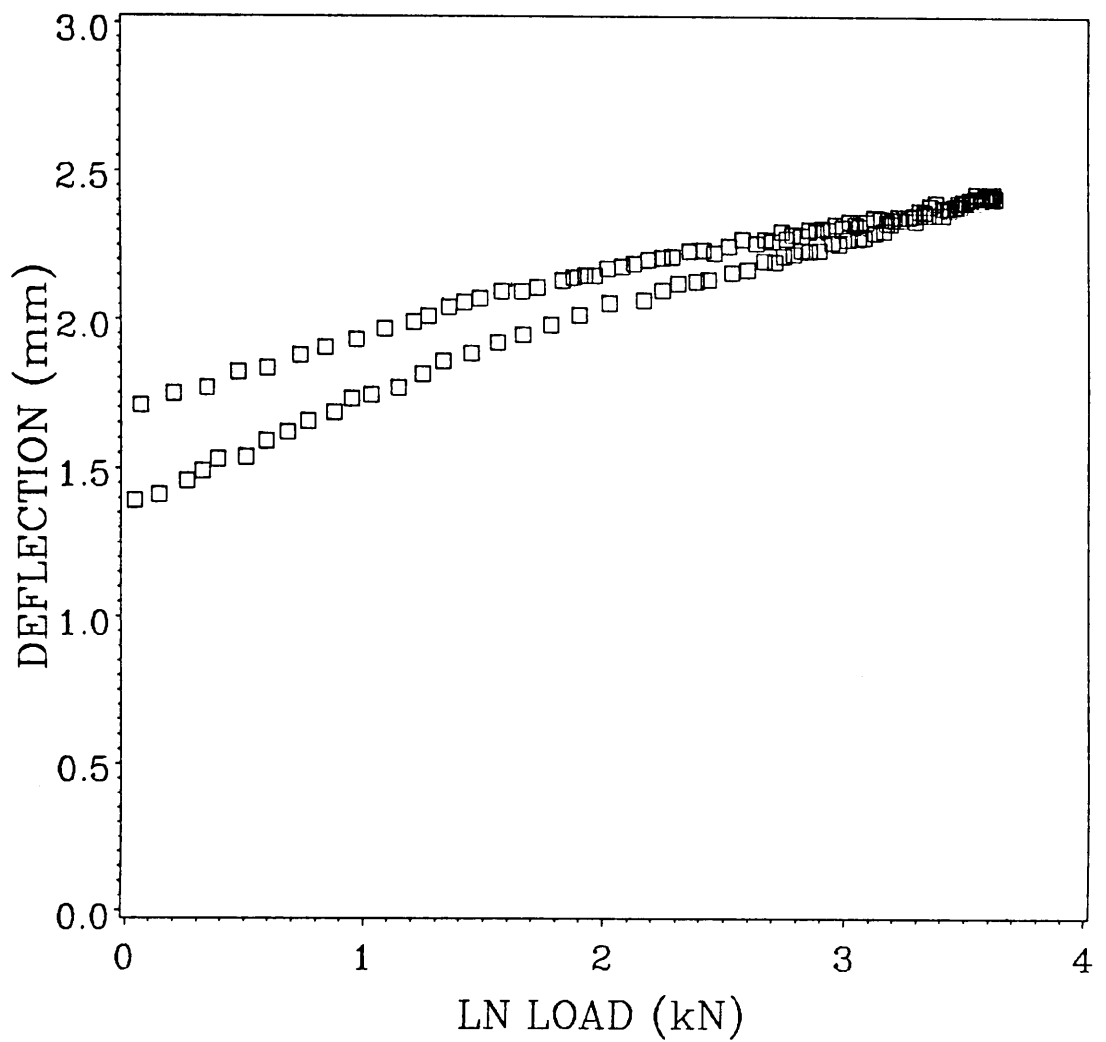


Figure 21. First load cycle of five plies of C3k/8HS fabric and the test fixture.

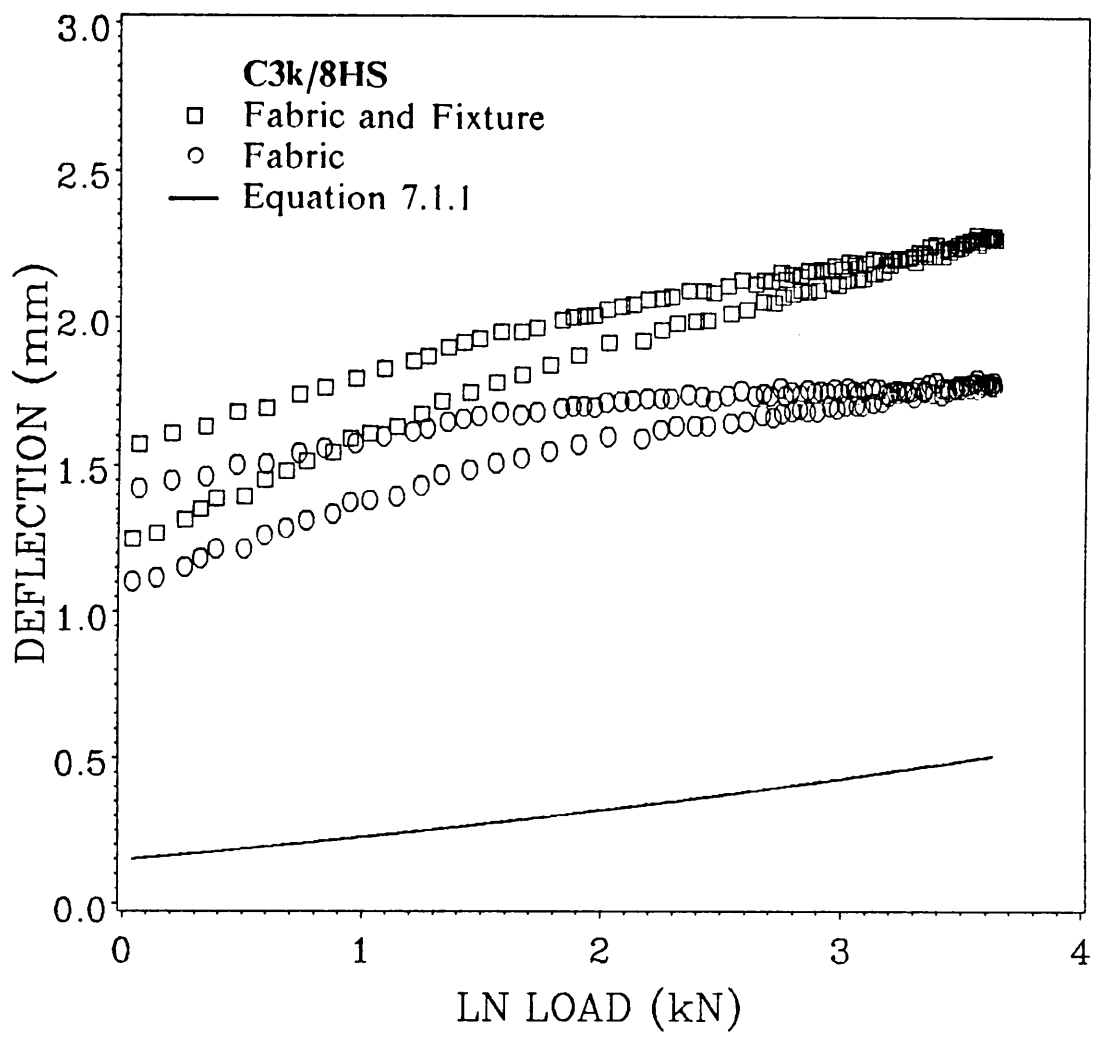


Figure 22. Effect of the fixture on the first loading cycle of C3k/8HS.

$$\begin{aligned}
 a_0 &= -4.789 \times 10^{-6} \text{ m} \\
 a_1 &= -2.256 \times 10^{-6} \text{ m/N} \\
 a_2 &= 4.751 \times 10^{-7} \text{ m/N}^2 \\
 a_3 &= -7.481 \times 10^{-9} \text{ m/N}^3
 \end{aligned}$$

and when unloading,

$$\begin{aligned}
 a_0 &= 6.200 \times 10^{-5} \text{ m} \\
 a_1 &= 1.303 \times 10^{-6} \text{ m/N} \\
 a_2 &= 2.025 \times 10^{-7} \text{ m/N}^2 \\
 a_3 &= -3.920 \times 10^{-9} \text{ m/N}^3
 \end{aligned}$$

Equation 7.1.2 was used with the matching procedure outlined in Section 3.2.1 and is shown in Figure 23 with the first cycle, adjusted data. The accuracy of the deflection model is excellent for this specimen.

Three specimens of five fabric plies each, were examined to investigate the repeatability of the experimental procedure. Each specimen was zeroed, adjusted and curve fit as described previously. Deflection model results for the initial loading path of each specimen and the mean response is shown in Figure 24. The magnitude of the deflection varies between specimens, however, the shape of the load-deflection response is nearly the same. The variation in magnitude is attributed to the procedure used to zero the deflection data. Mean fabric response was assumed to be characteristic of the fabric specimens.

An investigation was performed to determine the effect of varying the number of plies on the load-deflection behavior of C3k/8HS. The first load response for specimens of one, three, and five plies is shown in Figure 25. Each curve represents the mean be-

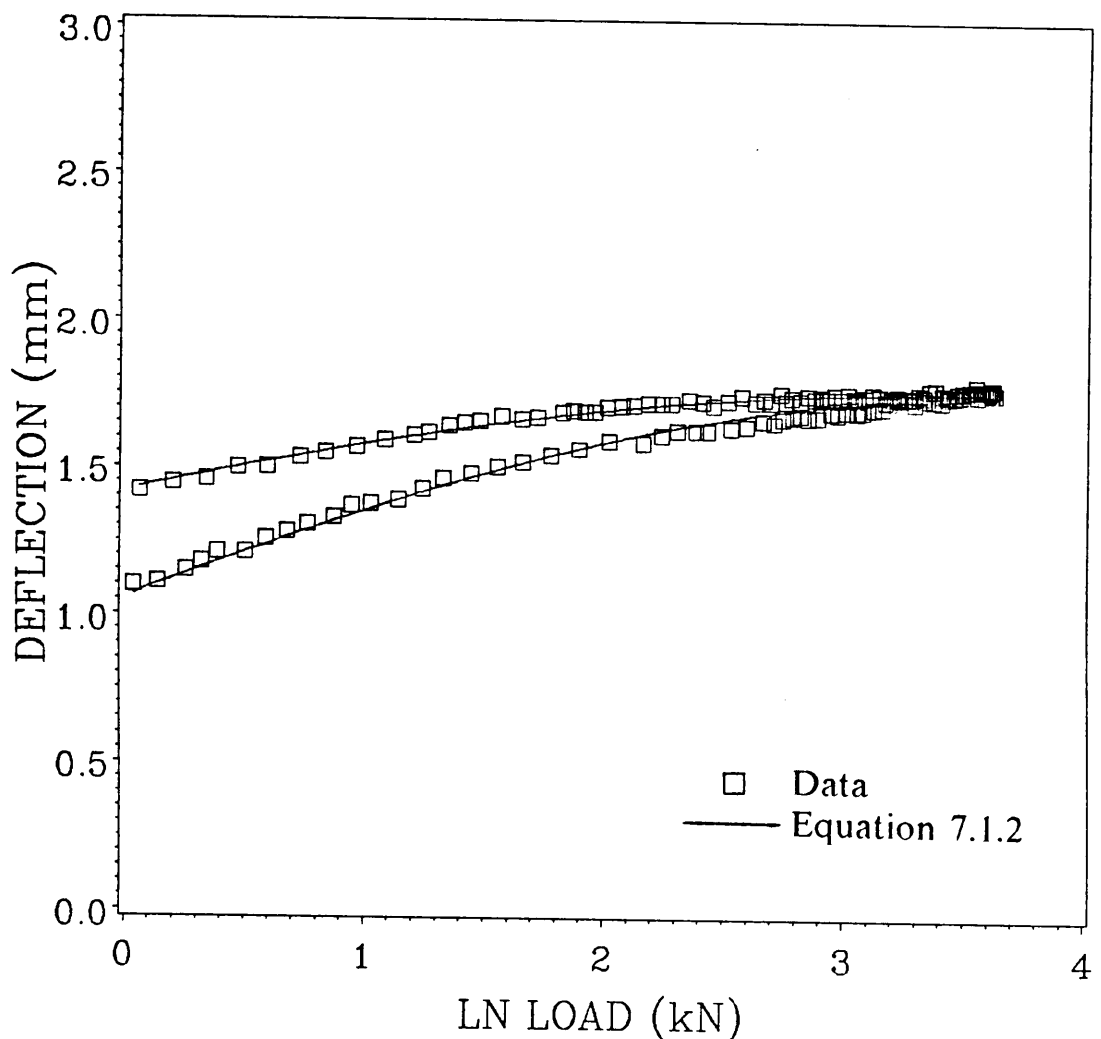


Figure 23. First loading cycle of adjusted, five ply, C3k/8HS data with Equation 7.1.2.

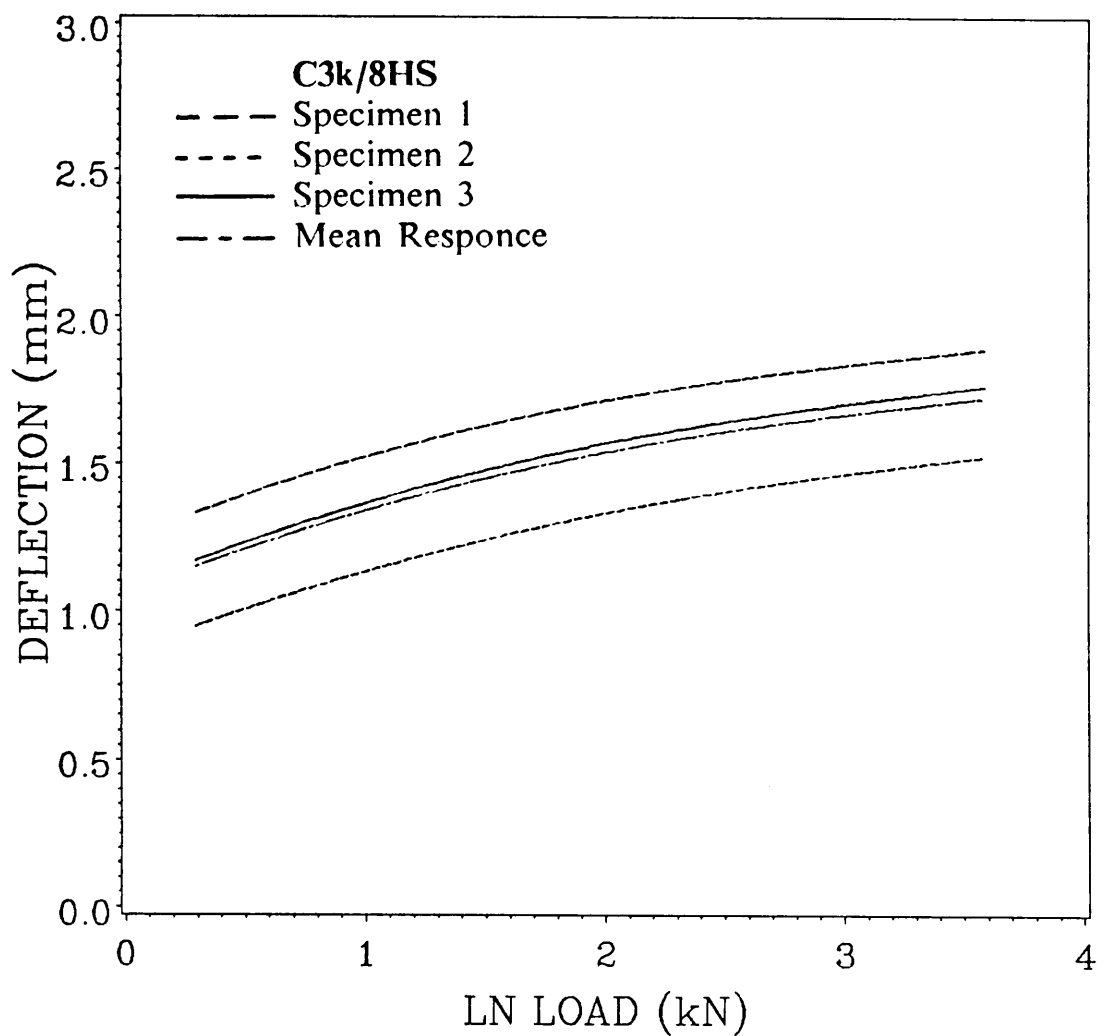


Figure 24. Variation between five ply specimens of C3k/8HS and mean response.

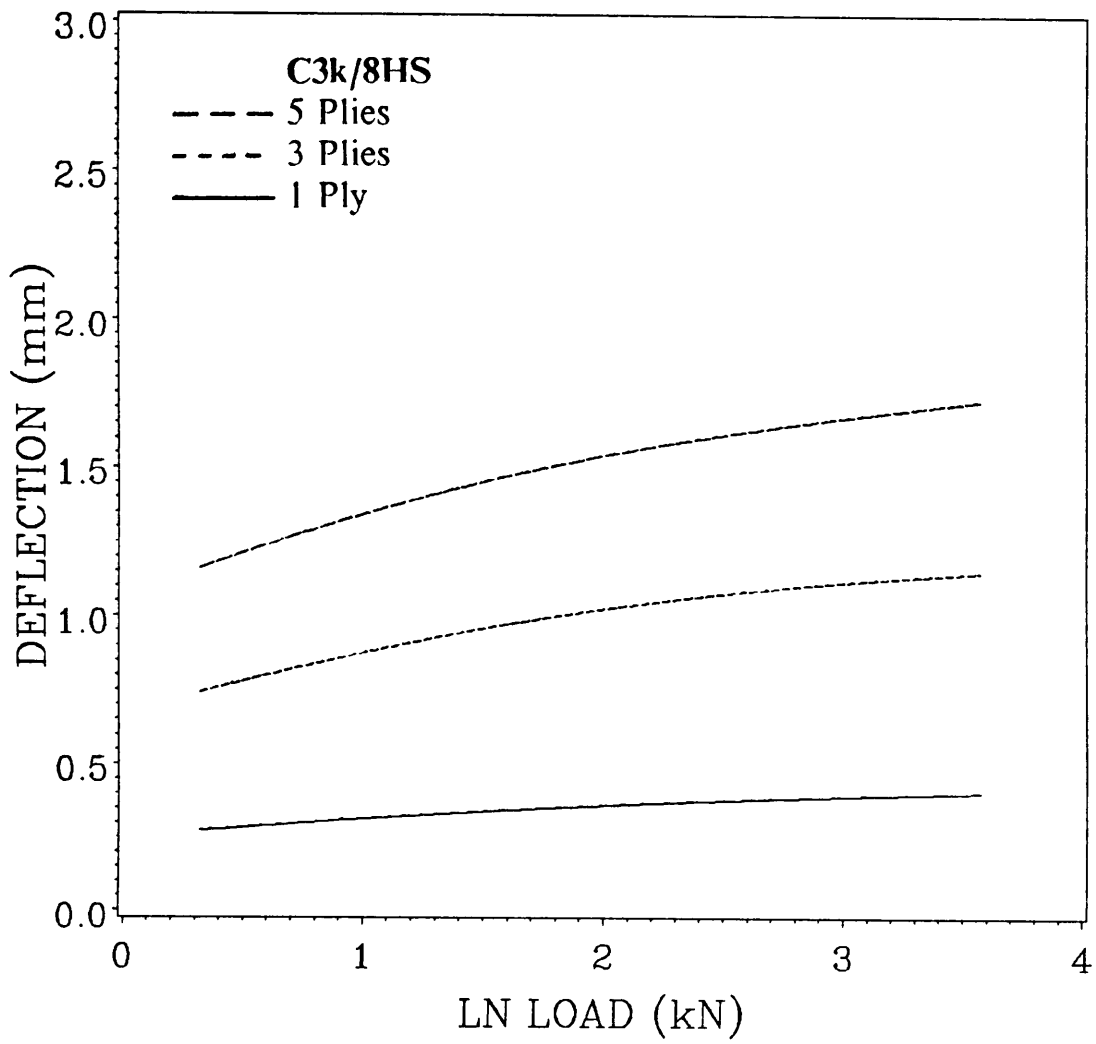


Figure 25. Initial loading curves of multi-ply specimens.

havior of three specimens. If the deflection is normalized by the number of plies, the material response is nearly the same as shown in Figure 26. Since the normalized deflection behavior does not vary significantly with the number of plies, the nesting of adjacent layers does not contribute to the total deflection. The normalized deflection coefficients of C3k/8HS fabric for four loading and unloading cycles are listed in Table 3.

A study of the compaction characteristics of IM7/8HS fabric was performed in a manner similar to the previous study. Two, five ply samples were cycled between 0 and 1400 kPa four times. The data was zeroed, adjusted and normalized as previously described and the resulting normalized compaction coefficients are shown in Table 4. Using the deflection model and matching procedure, the four cycle behavior of the IM7/8HS fabric was calculated and is shown in Figure 27. The shape of each loading and unloading path is very similar. The amount of permanent deformation decreases with each loading cycle. After the first cycle, the loading and unloading response is nearly independent of the number of cycles.

### 7.1.3 Wet Compaction

Wet compaction experiments were performed and analyzed in a similar manner to the experiments with dry materials. Two samples, of five plies each, were saturated with water and cycled four times. To accurately describe wet compaction, a fourth order version of Equation 3.2.1 was used. The resulting normalized compaction coefficients are listed in Table 5. Although the correlation coefficient for the fourth loading cycle was greater than 95 percent, the compaction model did not accurately describe the ex-

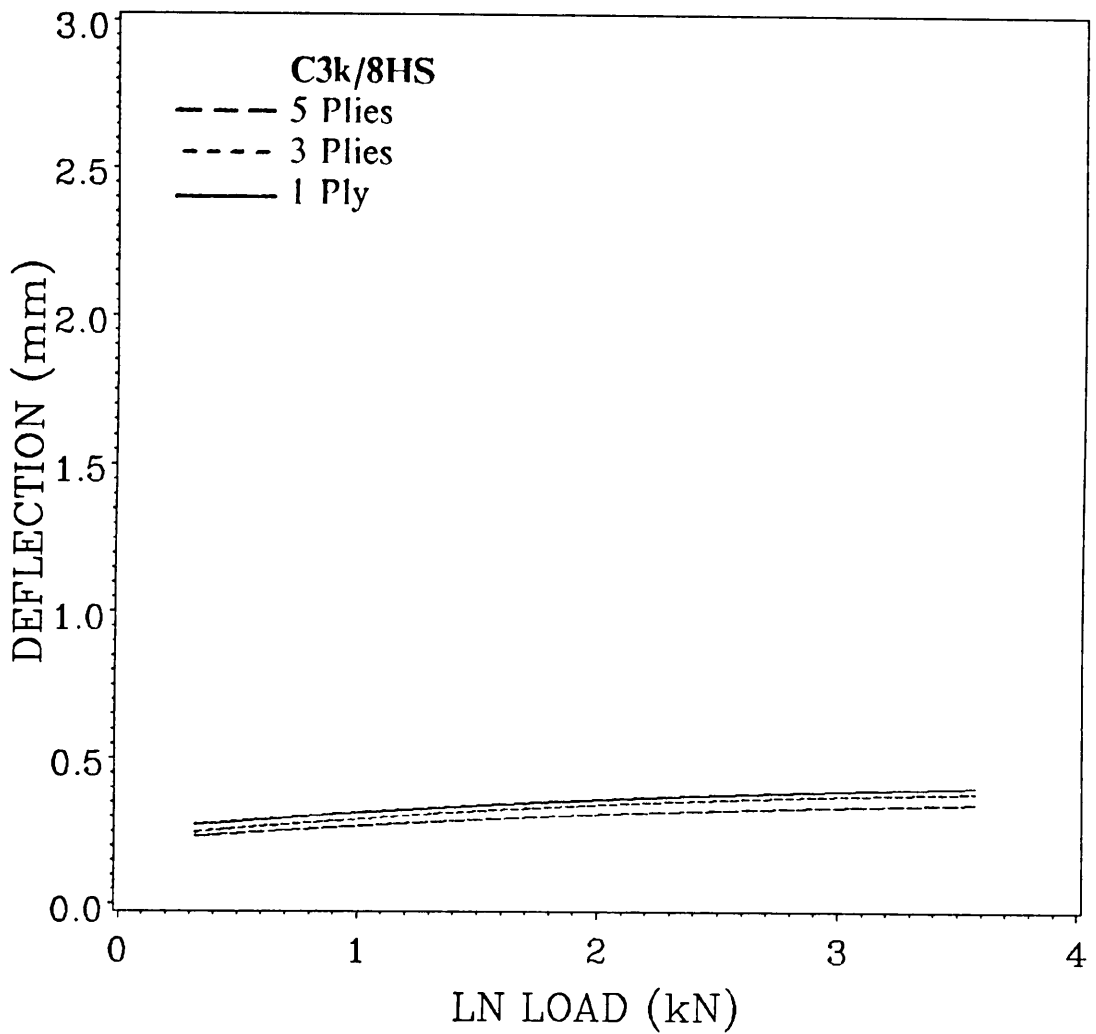


Figure 26. Normalized initial loading curves for multi-ply specimens.

**Table 3. Normalized Compaction Coefficients for Dry C3k/8HS Fabric.**

Loading

Cycle No.	Coefficient			
	$a_0$ (m)	$a_1$ ( $\frac{m}{N}$ )	$a_2$ ( $\frac{m}{N^2}$ )	$a_3$ ( $\frac{m}{N^3}$ )
1	-975.6	-451.2	95.02	-1.496
2	-1891.	-362.4	81.34	-1.308
3	-1478.	-195.2	72.04	-1.187
4	-3749.	78.97	59.92	-1.034

Unloading

Cycle No.	Coefficient			
	$a_0$ (m)	$a_1$ ( $\frac{m}{N}$ )	$a_2$ ( $\frac{m}{N^2}$ )	$a_3$ ( $\frac{m}{N^3}$ )
1	12400.	265.7	40.49	-0.7838
2	-2992.	1349.	2.905	-0.3645
3	1774.	647.0	28.54	-0.6715
4	-38510.	4745.	-113.1	0.9082

all values  $\times 10^{-8}$

**Table 4. Normalized Compaction Coefficients for Dry IM7/8HS Fabric.**

Loading

Cycle No.	Coefficient			
	$a_0$ (m)	$a_1$ ( $\frac{m}{N}$ )	$a_2$ ( $\frac{m}{N^2}$ )	$a_3$ ( $\frac{m}{N^3}$ )
1	620.0	-89.54	9.698	-0.1142
2	1604.	-281.8	12.95	-0.1404
3	1506.	-266.0	12.06	-0.1302
4	1454.	-254.6	11.53	-0.1244

Unloading

Cycle No.	Coefficient			
	$a_0$ (m)	$a_1$ ( $\frac{m}{N}$ )	$a_2$ ( $\frac{m}{N^2}$ )	$a_3$ ( $\frac{m}{N^3}$ )
1	4714.	-164.6	9.872	-0.01230
2	1244.	-175.4	9.806	-0.01197
3	1191.	-184.6	9.980	-0.01211
4	7607.	-132.9	7.904	-0.009601

all values  $\times 10^{-7}$

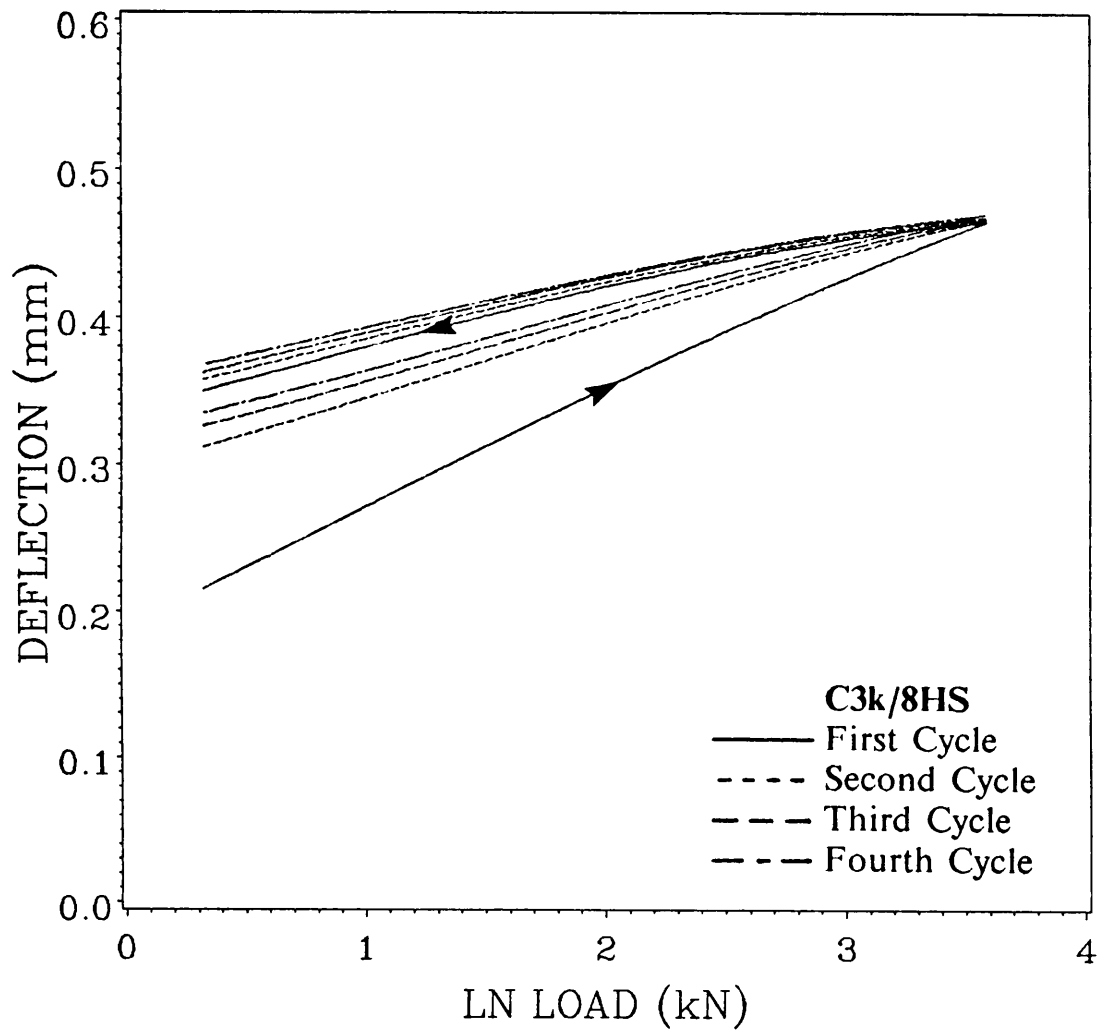


Figure 27. Normalized, four cycle behavior of IM7/8HS fabric.

**Table 5. Normalized Compaction Coefficients for Wet IM7/8HS Fabric.**

Loading

Cycle No.	$a_0$ (m)	Coefficient			
		$a_1$ ( $\frac{m}{N}$ )	$a_2$ ( $\frac{m}{N^2}$ )	$a_3$ ( $\frac{m}{N^3}$ )	$a_4$ ( $\frac{m}{N^4}$ )
1	1306.	-14.93	18.78	-0.4378	0.003143
2	5077.	-1024.	67.34	-1.698	0.01530
3	2279.	-499.0	33.43	-0.7956	0.006741
4	-91360.	16310.	-1024.	27.12	-0.2570

Unloading

Cycle No.	$a_0$ (m)	Coefficient			
		$a_1$ ( $\frac{m}{N}$ )	$a_2$ ( $\frac{m}{N^2}$ )	$a_3$ ( $\frac{m}{N^3}$ )	$a_4$ ( $\frac{m}{N^4}$ )
1	2918.	-21.45	6.306	-0.1212	0.0004918
2	-87.60	-0.8268	4.303	-0.06744	0.00002336
3	263.7	-72.35	8.352	-0.7472	0.0009706
4	635.0	-153.1	13.74	-0.3244	0.002550

all values  $\times 10^{-7}$

perimental data. The response for the first three loading and unloading cycles are shown in Figure 28. The behavior is quite similar to the dry fabric since the majority of the permanent deformation occurs during the first loading cycle. The initial loading curve crosses subsequent loading curves due to the accuracy of the curve fit and the averaging procedure. Actual data does not exhibit this behavior.

Initial load-deflection response of wet and dry IM7/8HS fabric models are compared in Figure 29. The amount of unrecoverable deformation and the total deflection is larger for the dry fabric. These differences are attributed to the presence of the fluid. Wet fiber tows move relative to one another more easily than the dry tows, thus, the fabric “recovers” more elastic deformation when wet. Intra-tow motion also increases in the presence of a fluid. No direct observations have been made to identify the relative amounts of intra-tow and inter-tow motion. Differences in total deformation might be attributed to the time required to remove the excess fluid during the later stages of compaction due to changes in fabric permeability. A study of loading rate on the saturated compaction characteristics would be required to confirm this supposition.

## 7.2 PERMEABILITY

The goal of the permeability experimental program was to measure and characterize changes in permeability due to changes in compaction pressure and porosity. The IM7/8HS fabric was tested through-the-thickness of the fabric and in the 0°, in-plane direction. Permeability results were compared to the Kozeny-Carman expression and literature values for systems of unidirectional fibers. Using the experimental values of flow rate and pressure gradient, the validity of D’Arcy’s law was investigated.

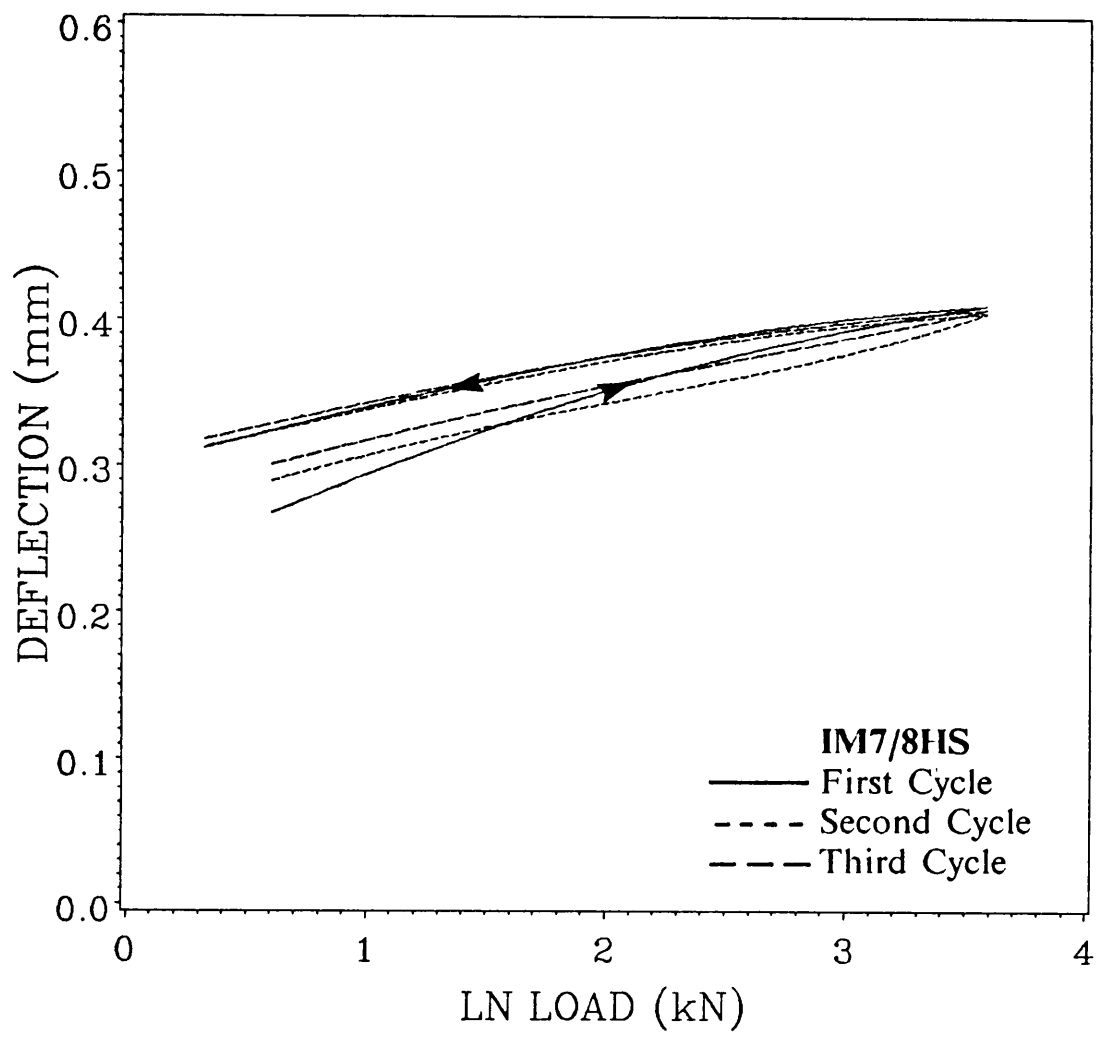


Figure 28. Compaction characteristics of the first three compaction cycles of wet IM7/8HS fabric.

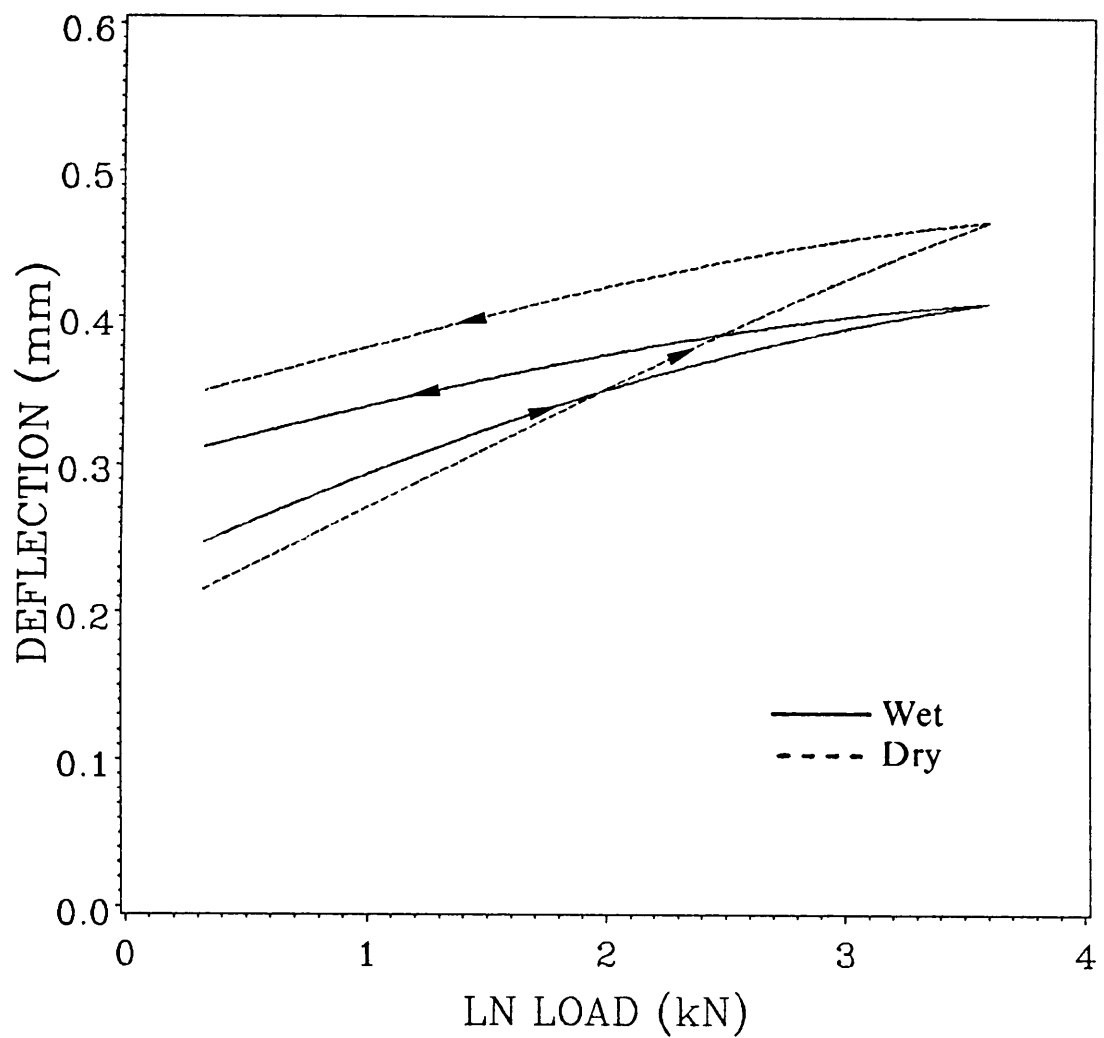


Figure 29. Comparison of wet and dry compaction behavior of the IM7/8HS fabric.

### 7.2.1 Experiment Preliminaries

Before actual permeability measurements could be made, investigations were required to calibrate the flow meter and to determine the effects of the fixture on the measured pressure data.

Calibration of the bubble type flow meter was required to relate the position of the steel ball in divisions,  $q'$ , to the volumetric flow rate,  $q$ . When the measured data was fit with Equation 6.3.1, the constants  $c_1$  and  $c_2$  were determined to be  $-1.280 \text{ cm}^3/\text{s}$  and  $1.503 \text{ cm}^3/(\text{divisions s})$  respectively. Calibration data and Equation 6.3.1 are displayed in Figure 30.

To obtain an accurate value of fabric thickness during the permeability experiments, load-deflection data of the fixture and wet fabric was modeled with Equation 6.3.4. Four terms were required for an accurate data fit, where the coefficients were determined to be,

$$\begin{aligned}c_0 &= -1.792 \text{ N} \\c_1 &= 9348 \text{ N/m} \\c_2 &= 3.877 \text{ N/m}^2 \\c_3 &= -1.292 \times 10^8 \text{ N/m}^3\end{aligned}$$

Actual fabric thicknesses were calculated using these constants and the procedure described in Section 6.3.4.

A pressure drop develops due to the tortuous path of a fluid particle as it passes through the empty test fixture. Values of pressure drop were measured at various amounts of fixture gap and flow rate. A pseudo-pressure gradient was calculated from the measured

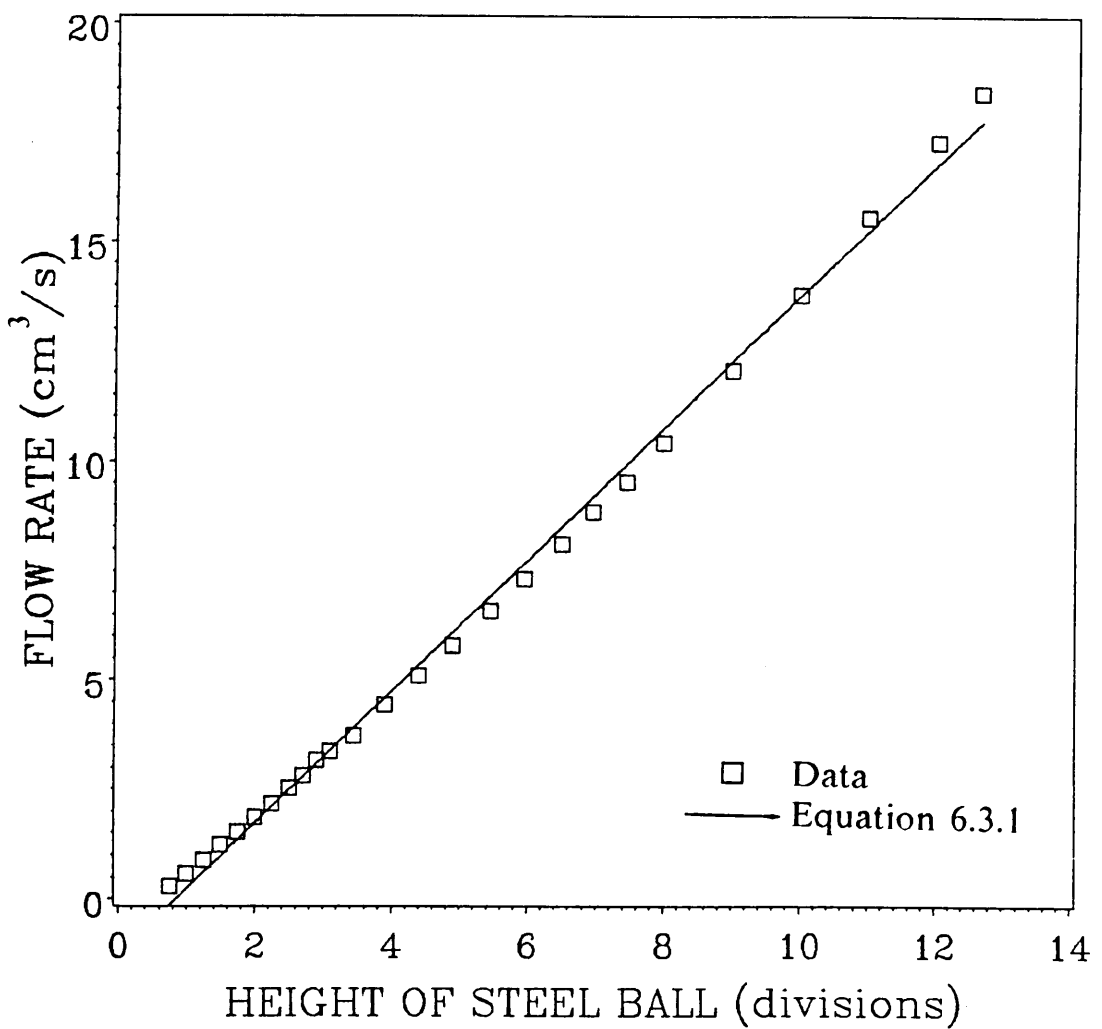


Figure 30. Flow meter calibration data and Equation 6.3.1.

data by dividing the pressure drop by the gap distance. When this gradient was related to the flow rate by Equation 6.3.3, the coefficients,  $a_i$ , varied significantly with the fixture gap. Equation 6.3.3 was modified to account for this behavior by allowing the coefficients to behave as linear functions of thickness. The resulting behavior can be described by the following expression,

$$\frac{dP}{dx}_{\text{fix}} = (b_0 + b_1 t) - (b_2 + b_3 t) q \quad (7.2.1)$$

where,

$$\begin{aligned} b_0 &= -7.146 \text{ kPa/m} \\ b_1 &= -1181. \text{ kPa/m}^2 \\ b_2 &= 8.597 \times 10^6 \text{ kPa s/m}^4 \\ b_3 &= -1.998 \times 10^9 \text{ kPa s/m}^5 \end{aligned}$$

and  $t$  is the gap between the porous plates. Figure 31 contains selected experimental results and the corresponding behavior of Equation 7.2.1.

## 7.2.2 Transverse Permeability Results

Through-the-thickness permeability experiments were performed on five, five ply samples of IM7/8HS fabric. For each specimen, manometer and flow meter values were measured at approximately six compacted thicknesses. The measured values were adjusted as described in Sections 6.3 and 7.2.1 to obtain the flow rate and the pressure gradient across the fabric. As expected, increasing the compaction pressure caused an increase in the resistance to fluid motion. Experimental data and Equation 6.3.7 are shown in Figure 32 for sample Number 3. Experimental velocities were used to calculate

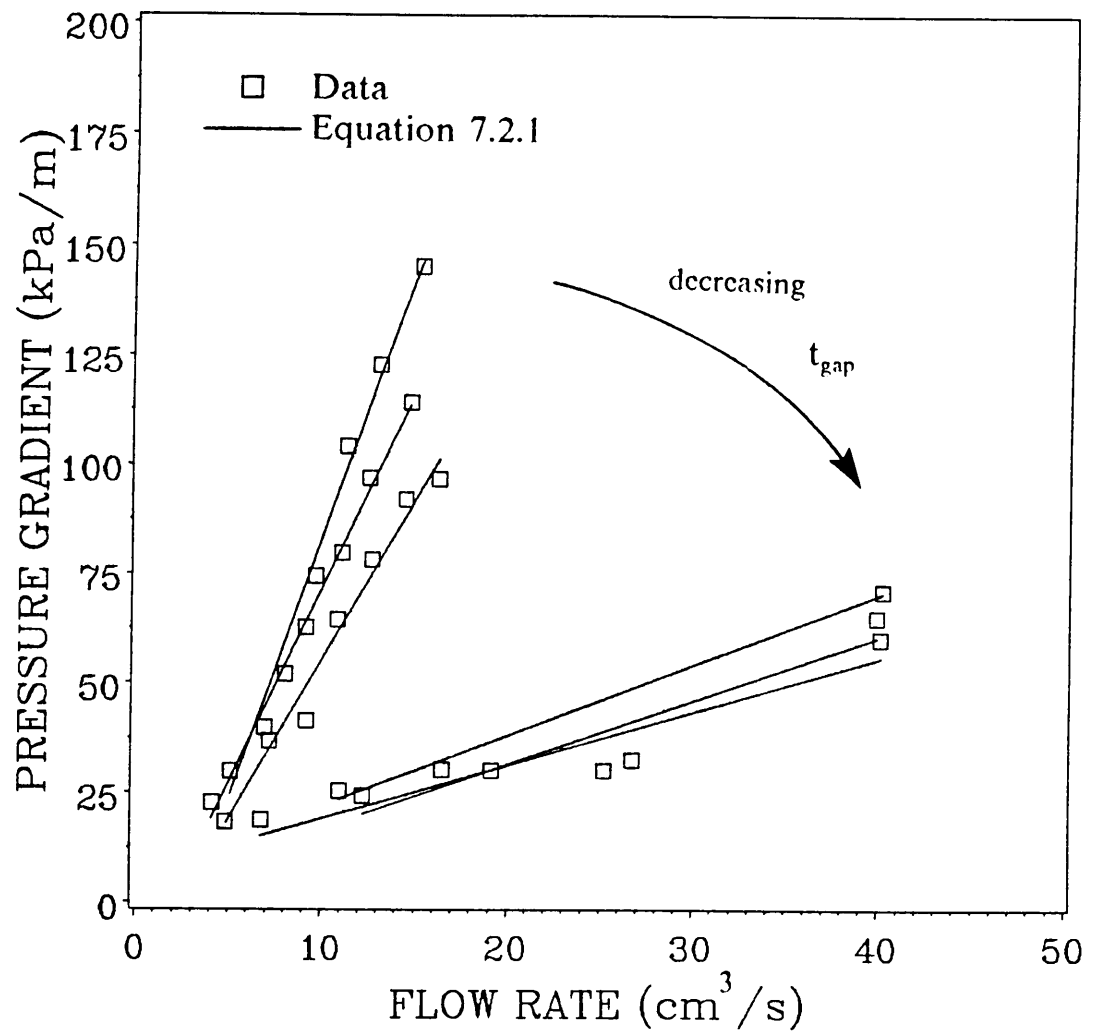


Figure 31. Selected flow data for the empty fixture and Equation 7.2.1.

the maximum Reynolds number for each experiment. In all cases, the Reynolds number did not exceed  $5 \times 10^{-3}$ , indicating the flow through this fabric could be described by D'Arcy's law.

From the slope of the flow rate versus pressure gradient curve, the permeability can be computed with Equation 6.3.8. When the two terms of Equation 6.3.7 were examined after the data reduction, the magnitude of  $b_1$  was found to be several orders less than the magnitude of  $b_2 \frac{dP}{dx}_{\text{fabric}}$ , and was subsequently neglected. If solid-fluid surface interactions were significant, the magnitude of  $b_1$  would approach the magnitude of the second term at low values of pressure gradient and would be positive. The sign of  $b_1$  was not consistent either for a particular specimen or from one fabric sample to the next.

Units of permeability are length squared, so when the permeability is normalized by the diameter of the fiber many experiments can be compared irrespective of fiber size. Fabric porosities were computed from Equation 3.2.13, the fabric characteristics shown in Table 1, and the thickness of the fabric.

Through-the-thickness porosity-permeability results are shown in Figure 33. No appreciable data scatter was evident for any particular specimen, although some variation between specimens was observed. As expected, the data indicates a decrease in permeability with decreasing porosity. Decreasing porosity indicates that there is less space for the fluid to move through the porous fiber bed which increases the resistance to the flow, and decreases the permeability.

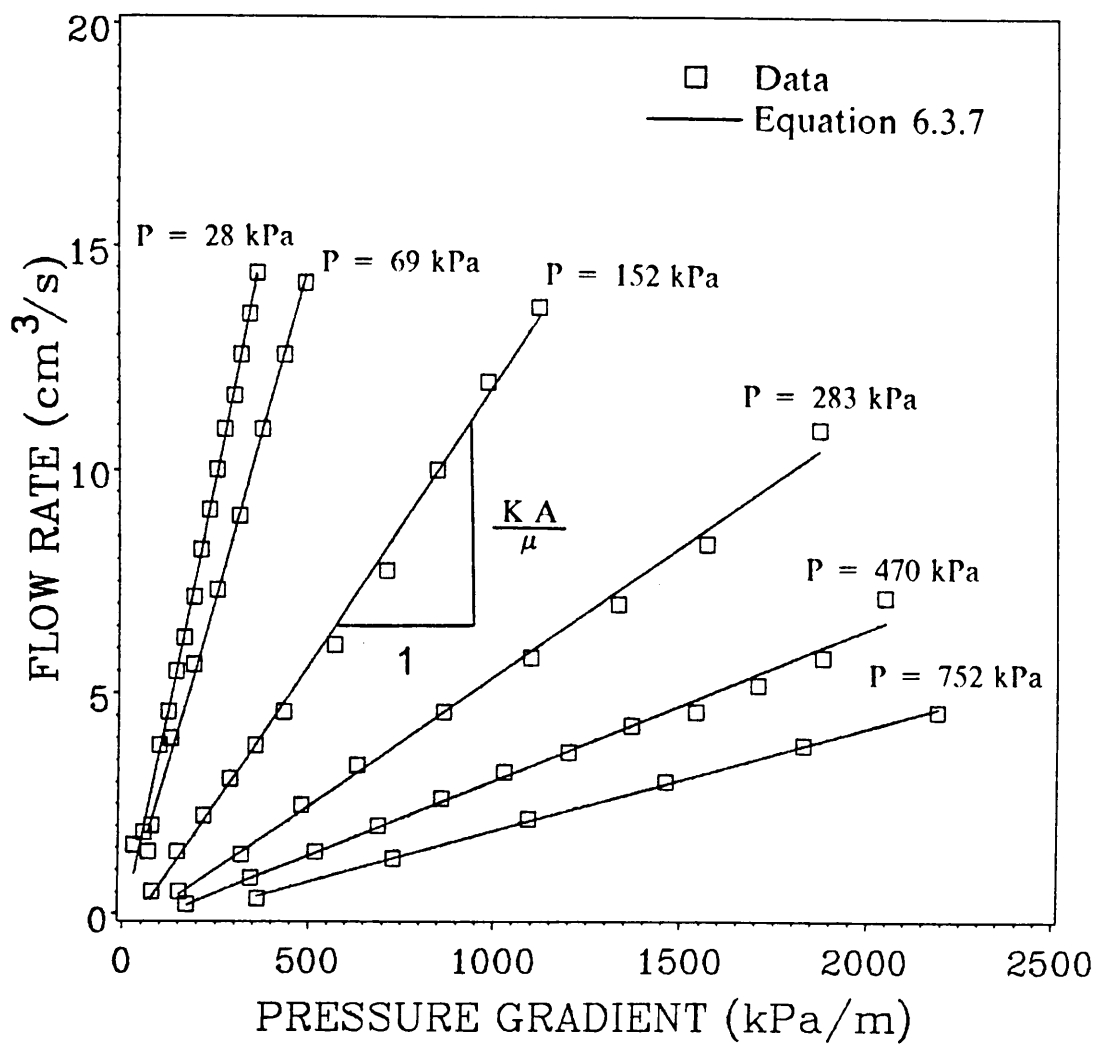


Figure 32. Experimental data and Equation 6.3.7 for IM7/8HS fabric sample Number 3.

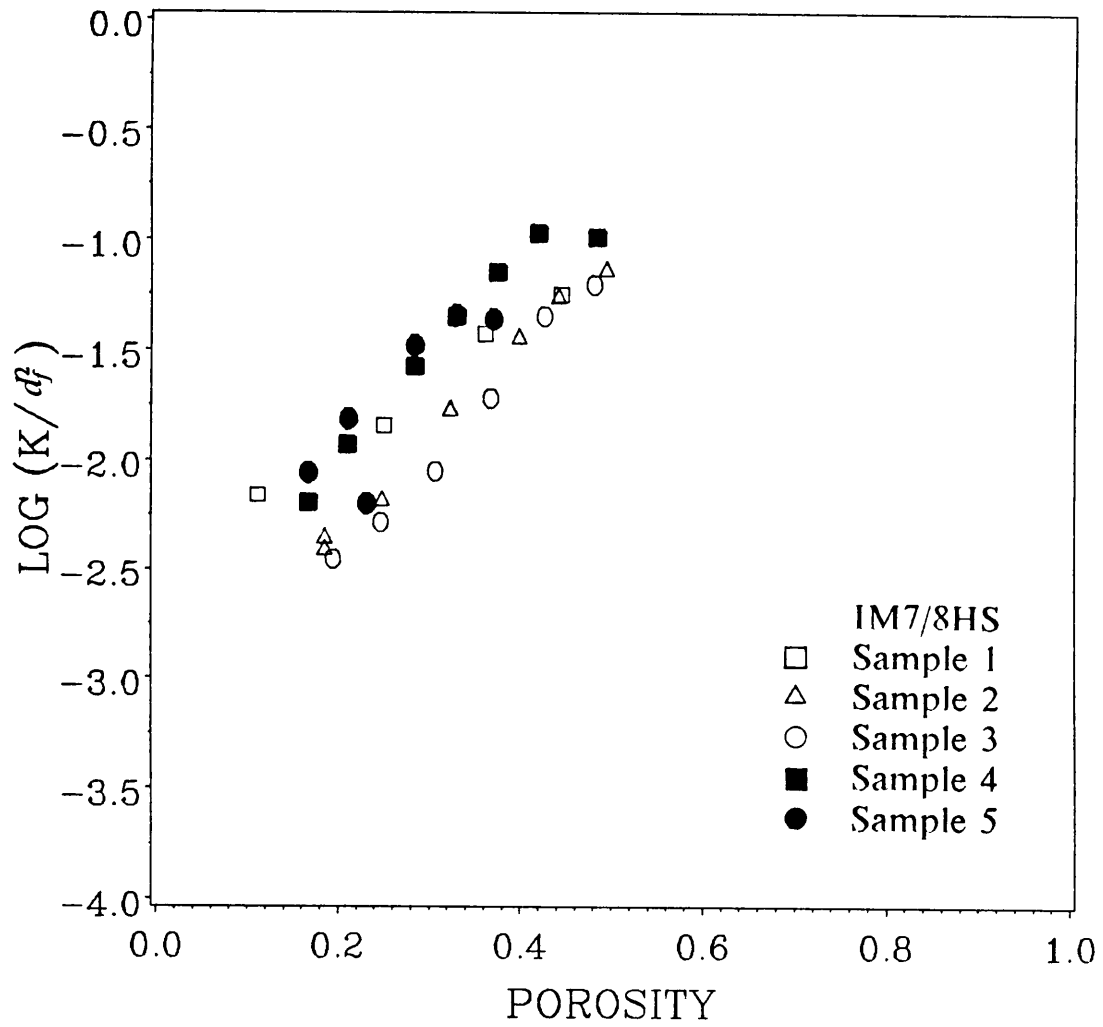


Figure 33. Measured through-the-thickness permeability of five plies of IM7/8HS fabric.

### 7.2.3 Transverse Permeability Verification

A review of the current literature revealed many sources of transverse permeability for fibrous materials. Only two investigators examined materials in the same porosity range as the present study. Gutowski *et al.* [23] report permeability values for a system of unidirectional Hysol-Grafil XA-S graphite fibers oriented transverse to the flow. The porosity range of this study is quite small ( $0.30 \pm 0.02$ ), however, the trend of decreasing permeability with decreasing porosity observed with the IM7/8HS fabric is followed. The magnitude of the permeability for the unidirectional fiber system is much less than the fabric as shown in Figure 34. Differences in permeability of the two materials can be attributed to the geometry of the fibers in the fabric. Individual tows are oriented at right angles and undulate within each layer which causes a nonhomogenous distribution of fibers. Regions between tows are much less dense than the inter-tow regions. Since the fluid will travel along a path of least resistance, the fabric should have a lower resistance to flow than the unidirectional fiber system.

Lam and Kardos [22] report transverse permeability values for flow through systems of aligned graphite fibers oriented in a variety of aligned and crossed ply configurations. In all cases, the permeabilities are less than those measured with the IM7/8HS fabric and larger than the values reported by Gutowski *et al.* [23] as shown in Figure 34.

Small differences in permeability are observed between the crossed ply configurations. The 0/90 crossed ply orientation has the smallest permeability, followed by the 0/45 and the 0/30 configurations respectively. Differences in permeability might be attributed to the way individual fibers pack within in the fiber bed. Fiber orientation is the same for the 0/90 crossed ply configuration and the fabric used in the present study, however,

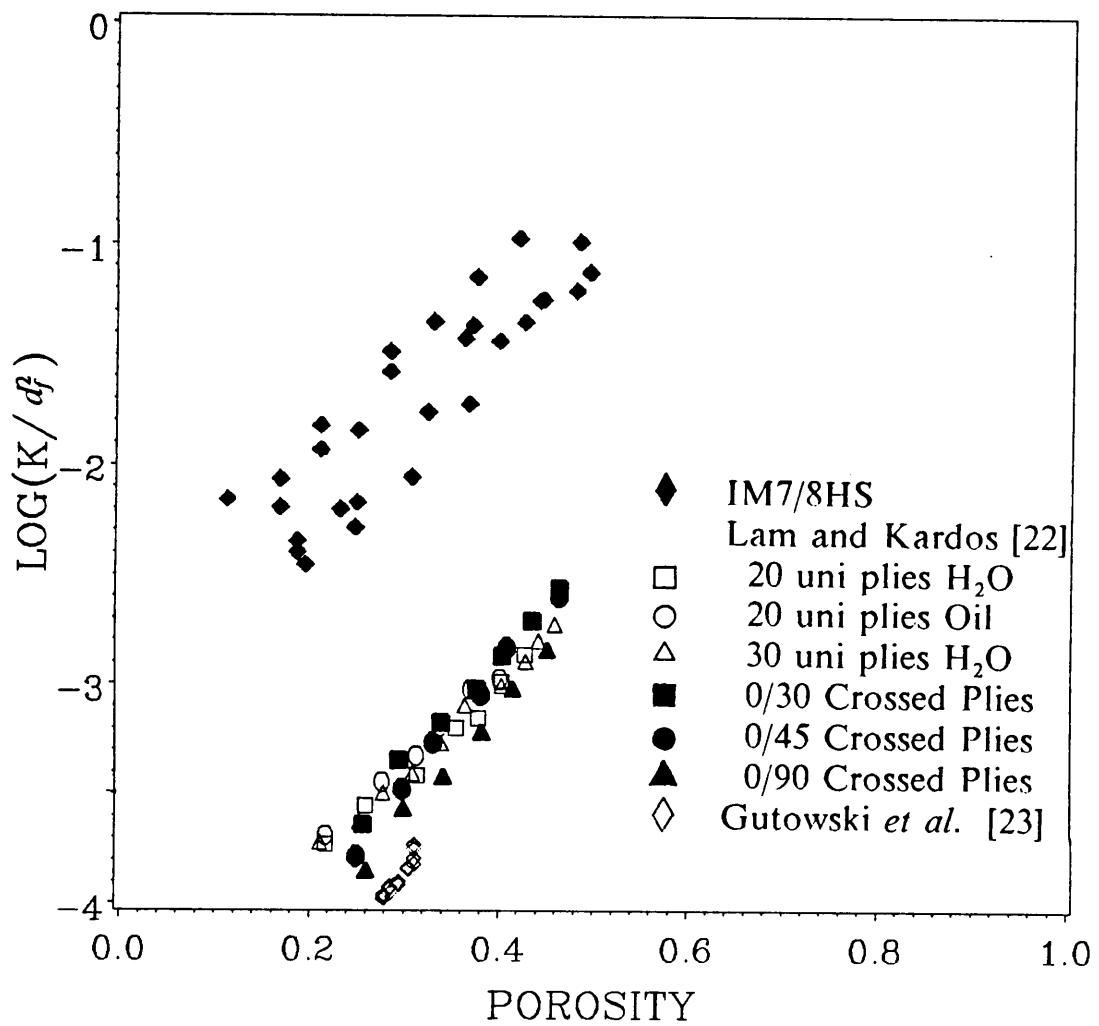


Figure 34. Through-the-thickness permeability comparison with literature values.

permeability of the 0/90 fiber system is significantly less than the fabric. Nonhomogenous fiber distributions, due to tow undulations in the fabric, could cause differences in permeability.

Using the previous data sets, the dependence of test fluid viscosity on the transverse permeability can also be addressed. Gutowski *et al.* [23] permeabilities were measured with fluid viscosities of 0.05, 0.91, and 9.62 Pa s. No difference in permeability is observed. Lam and Kardos [22] used fluid viscosities of 0.001 and 0.005 Pa s for the aligned fiber system with little observed effect. Experiments with crossed ply fibers were performed with water ( $\mu = 0.001$  Pa s). Based on these results, the transverse permeability of fibrous materials is greatly influenced by orientations of individual filaments and not by the fluid viscosity.

Kozeny-Carman's model, Equation 3.2.18, was successfully fit to the experimental fabric data with a value of the Kozeny-Carman constant of 2.8798. The data is slightly less dependent on the porosity than is predicted by the Kozeny-Carman model as shown in Figure 35.

#### 7.2.4 In-Plane Permeability Results

Permeability experiments were performed on three, five ply specimens of IM7/8HS fabric in the plane of the fabric. Flow rate and pressure drop values were obtained and manipulated in a manner similar to the through-the-thickness experiments. The loss of energy due to the fixture was negligible when configured for the in-plane tests.

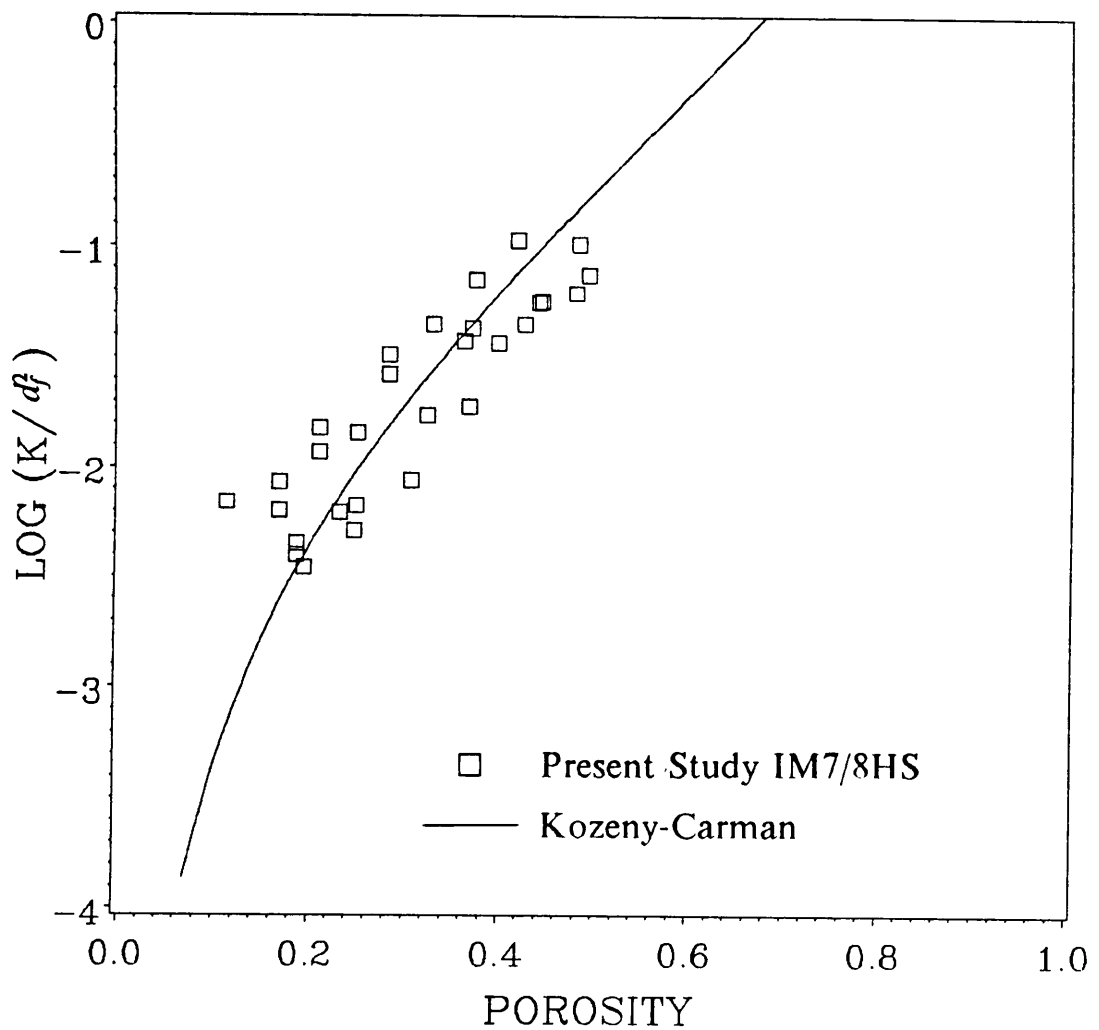


Figure 35. Through-the-thickness fabric permeabilities and the Kozeny-Carman model.

Pressure gradient and volumetric flow rate data were fit with Equation 6.3.7. The constant  $b_1$  was determined to be negligible. Results for sample Number 2, and the corresponding data fit, are shown in Figure 36.

### 7.2.5 In-Plane Permeability Verification

Permeabilities for in-plane flow were calculated from the first order constant in equation 6.3.7 and are displayed in Figure 37 with values reported by Gutowski *et al.* [23] and Lam and Kardos [22] for aligned Hercules AS4 fibers. Measured fabric permeabilities are independent of porosity and are much larger in magnitude than the literature results. One explanation for the independence on porosity is related to how the fixture was sealed during the experiment. A gap between the plunger and the female portion of the mold, parallel to the flow direction as shown in Figure 38, allowed fluid to move through the fixture without flowing through the fabric. If a significant portion of fluid flows through this gap, the measured pressure drop will not be due to the resistance of the fabric and will be independent of the material porosity.

Lam and Kardos [22] report in-plane permeability values for aligned fiber systems measured with water and a viscous oil, and 0/90, 0/45 and 0/30 crossed ply values measured with water. Permeability values measured with oil are consistently larger than values measured with water. As with the transverse flow configuration, the permeabilities of the 0/90 sample are the smallest followed by the 0/45 and 0/30 samples respectively. This trend is expected since the resistance of a group of fibers transverse to the flow direction is greater than along a fiber bundle. The 0/90 crossed ply configuration is similar to the orientation of fibers in the IM7/8HS fabric. Differences in fabric

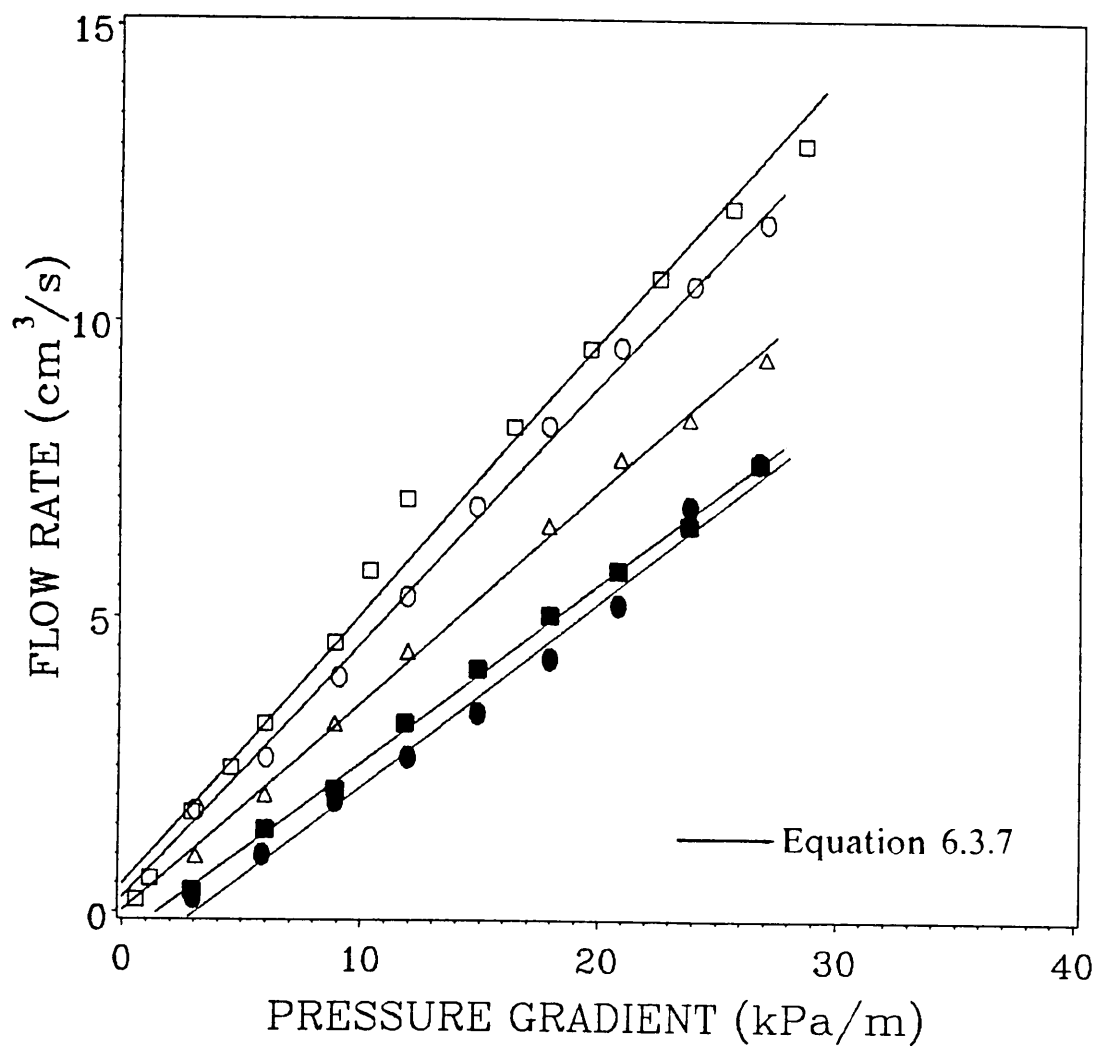


Figure 36. In-Plane flow data and Equation 6.3.7 for sample Number 2.

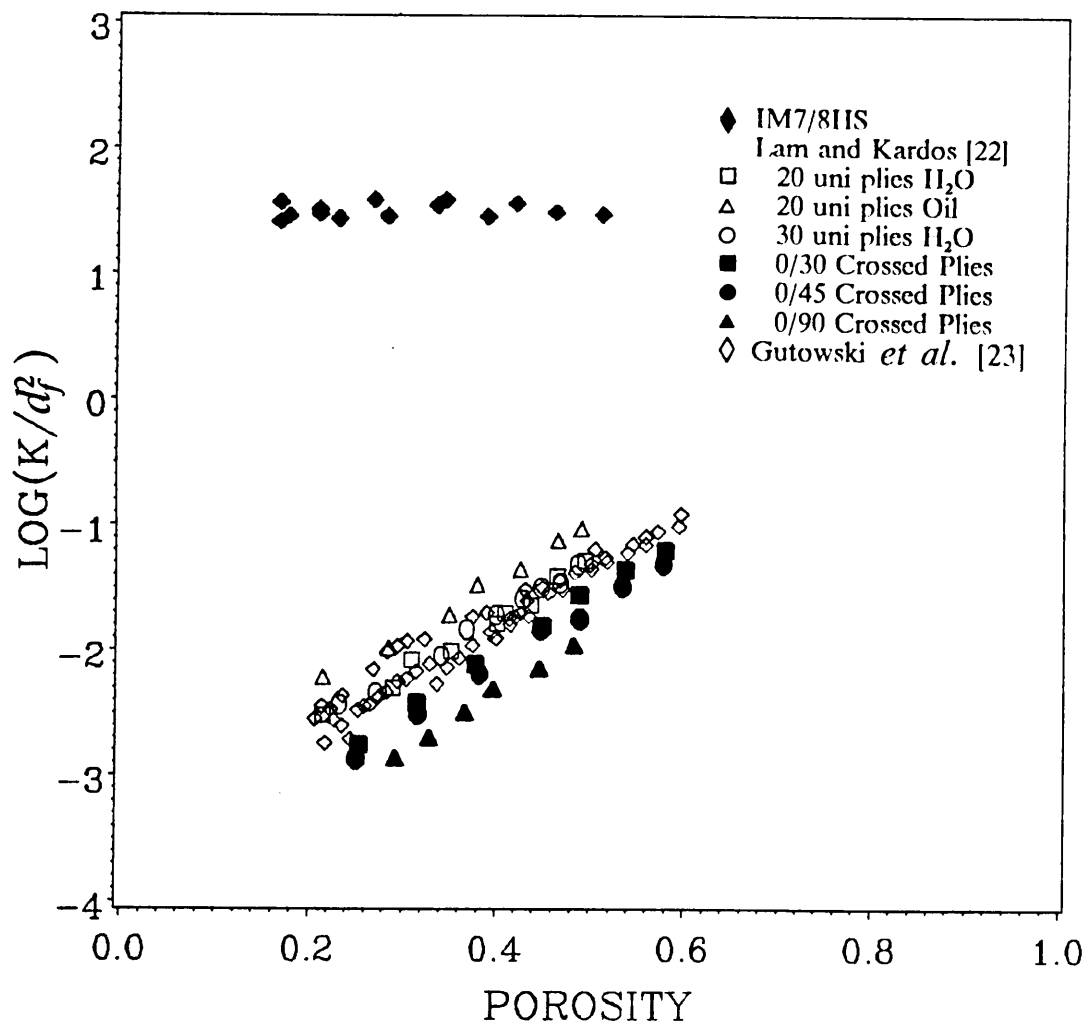


Figure 37. In-Plane permeability comparison with literature values.

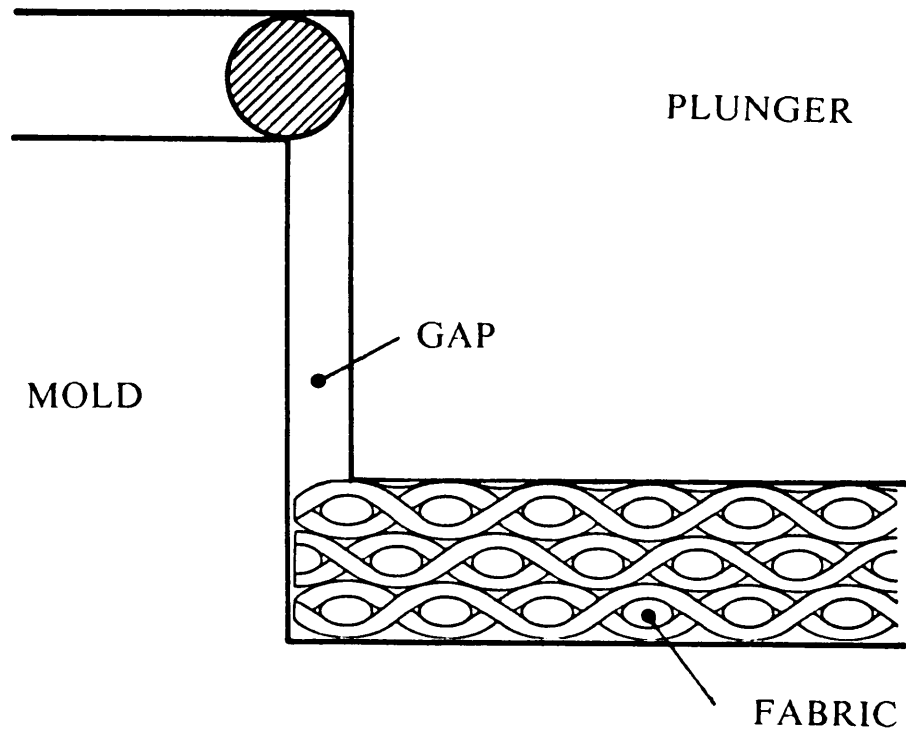


Figure 38. Schematic of gap in fixture.

and aligned fiber permeabilities are expected due to undulations of the fiber tows and nonhomogeneous fiber distributions. In all cases, the literature results indicate the in-plane permeability is a strong function of porosity and suggest that the fabric permeability values are incorrect.

Data reported by Gutowski *et al.* [23] for aligned fiber systems was determined with a variety of viscous fluids and is scattered around the data reported by Lam and Kardos [22]. Dependence on viscosity cannot be discussed for this data since viscosities were not reported for each data set.

## 7.3 MECHANICAL CHARACTERIZATION

An experimental program was performed to compare the RTM process to other manufacturing methods on the basis of mechanical performance of cured laminates. Four RTM laminates were produced by the vacuum bag infiltration technique from IM7/8HS fabric and one of the resin systems described in Section 6.1. Heat and pressure were applied by a heated platen press. Cured laminates were examined nondestructively, machined into test specimens and loaded to failure in tension and compression. Experimental values were compared to manufacturer's published results of an AS4/8HS fabric, 3501-6 resin laminate on the basis of elastic modulus, ultimate stress and ultimate strain.

### **7.3.1 Nondestructive Evaluation**

Nondestructive evaluation of the cured laminates included visual examination of the surface, through-the-thickness photomicrographs and ultrasonic, gray-scale C-scans.

The surfaces of Laminate 4228 appeared uniform but slightly resin rich due to the use of a nonporous release material during processing. A gray-scale, ultrasonic C-scan was performed to access the overall quality of the laminate; the resulting image is shown in Figure 39. The region of reduced quality in the upper left portion of the laminate was identified as voids when specimens were machined from this area.

Photomicroscopy was used to examine the distribution of resin through-the-thickness of the laminate. Figure 40 is a through-the-thickness photomicrograph of Laminate 4228. Individual fiber tows normal to the surface are visible as oval bundles and tows parallel to the machined surface appear as undulating ribbons. The darker regions surrounding the tows are unreinforced resin.

Ultrasonic inspection of Laminate 4268 was performed with a gray-scale C-scan as shown in Figure 41. Comparing Laminates 4228 and 4268 on the basis of their C-scans, the quality of Laminate 4268 appears more uniform. When specimens were machined from the panel, no macroscopic voids were visible.

Figure 42 is a photomicrograph of Laminate 4268. The boundaries between the fiber tows normal to the machined surface are much more difficult to determine compared to Laminate 4228. The resin rich zones, observed in Figure 40, are also much less prevalent in this laminate. Based on ultrasonic and visual information, Laminate 4268 should ex-

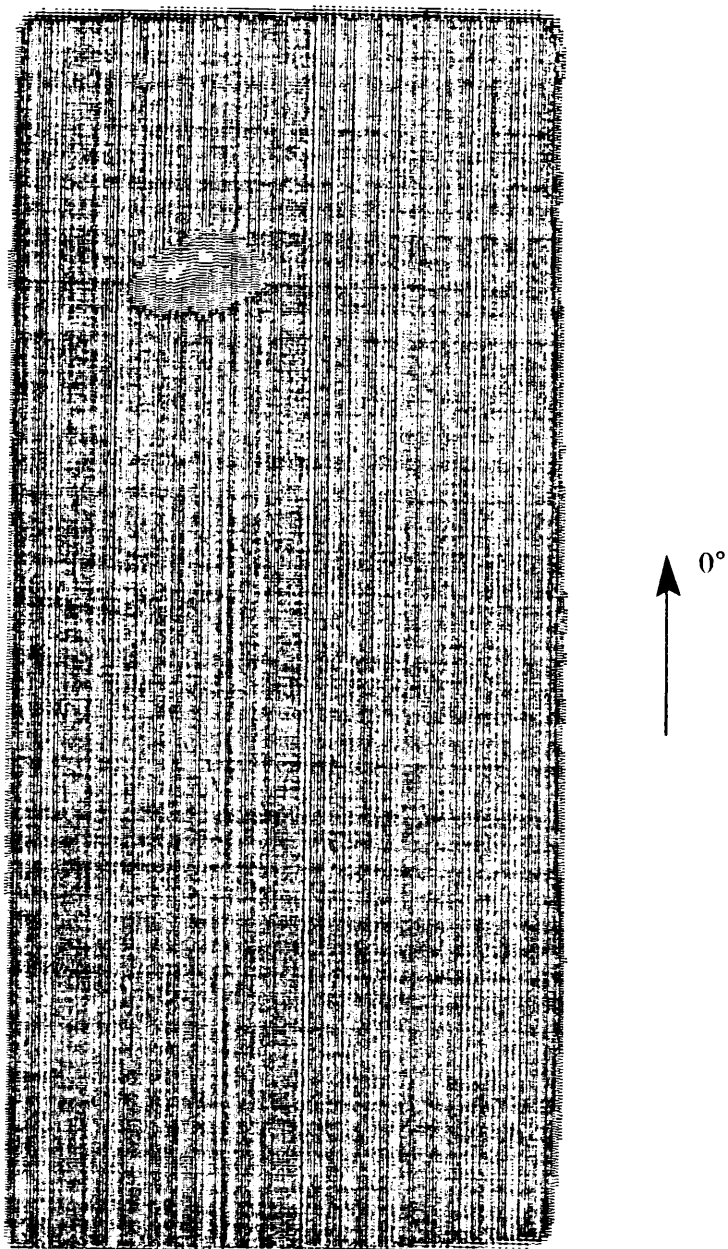
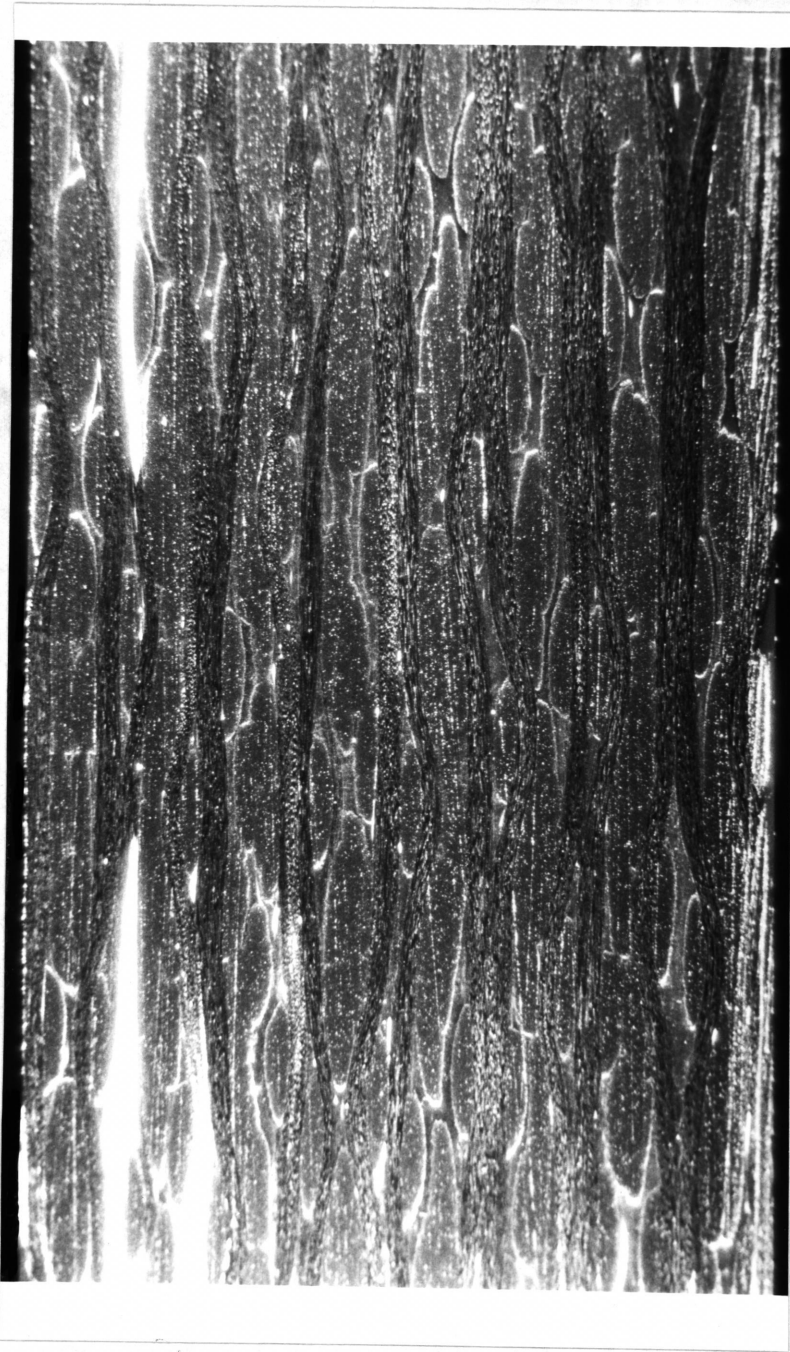


Figure 39. Ultrasonic, gray-scale C-scan of Laminate 4228.



**Figure 40.** Photomicrograph of Laminate 4228 (10.6 X).

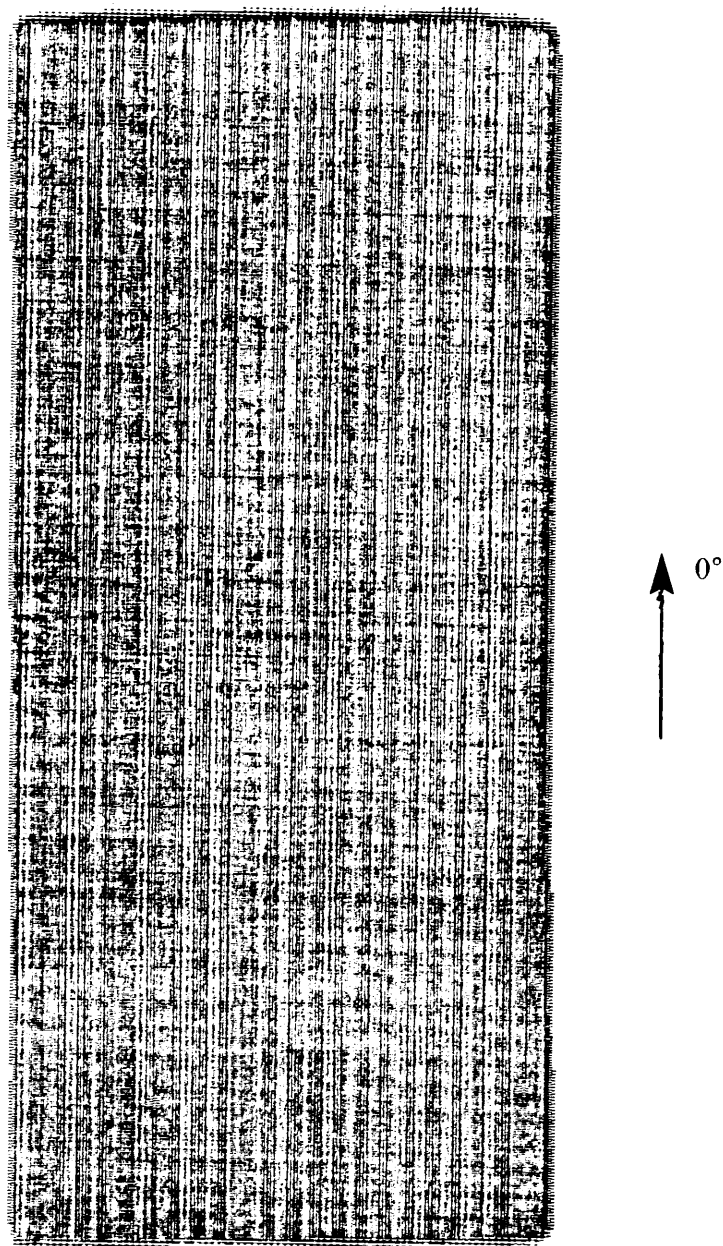


Figure 41. Ultrasonic, gray-scale C-scan of Laminate 4268.



**Figure 42.** Photomicrograph of Laminate 4268 (9.4 X).

hibit better mechanical characteristics due to improved homogeneity and fiber volume fraction.

Ultrasonic inspection of Laminate 5118 was performed and the resulting gray-scale C-scan is shown in Figure 43. A gradient in the ultrasonic attenuation is evident along the length of this laminate. Visual inspection of the laminate surfaces and specimen edges did not reveal the cause of this gradient. No appreciable change in thickness was observed and the gradients in attenuation cannot be explained.

Figure 44 is a photomicrograph of panel 5118. As with Laminate 4228, individual tows and large resin rich regions are visible. Based on visual examination of the laminate and thickness measurements, the volume fraction of this laminate should be slightly less than Laminate 4228. Relative estimates of the laminate mechanical properties cannot be made since Laminate 5118 was manufactured with a different resin system.

Large regions of unreinforced resin and large separations between individual tows are visible in the photomicrograph of Laminate 5238 shown in Figure 45. Another feature of this laminate is the presence of voids located between individual tows. The edges and sides of the voids are smooth, indicating the voids were formed by trapped gases and not by nonuniform infiltration. Visual inspection of other cross-sections revealed a uniform distribution of macroscopic voids throughout the laminate. From the micrograph, the volume fraction of this laminate is expected to be the lowest of the laminates produced during this study. Ultrasonic inspection of this laminate was not performed.

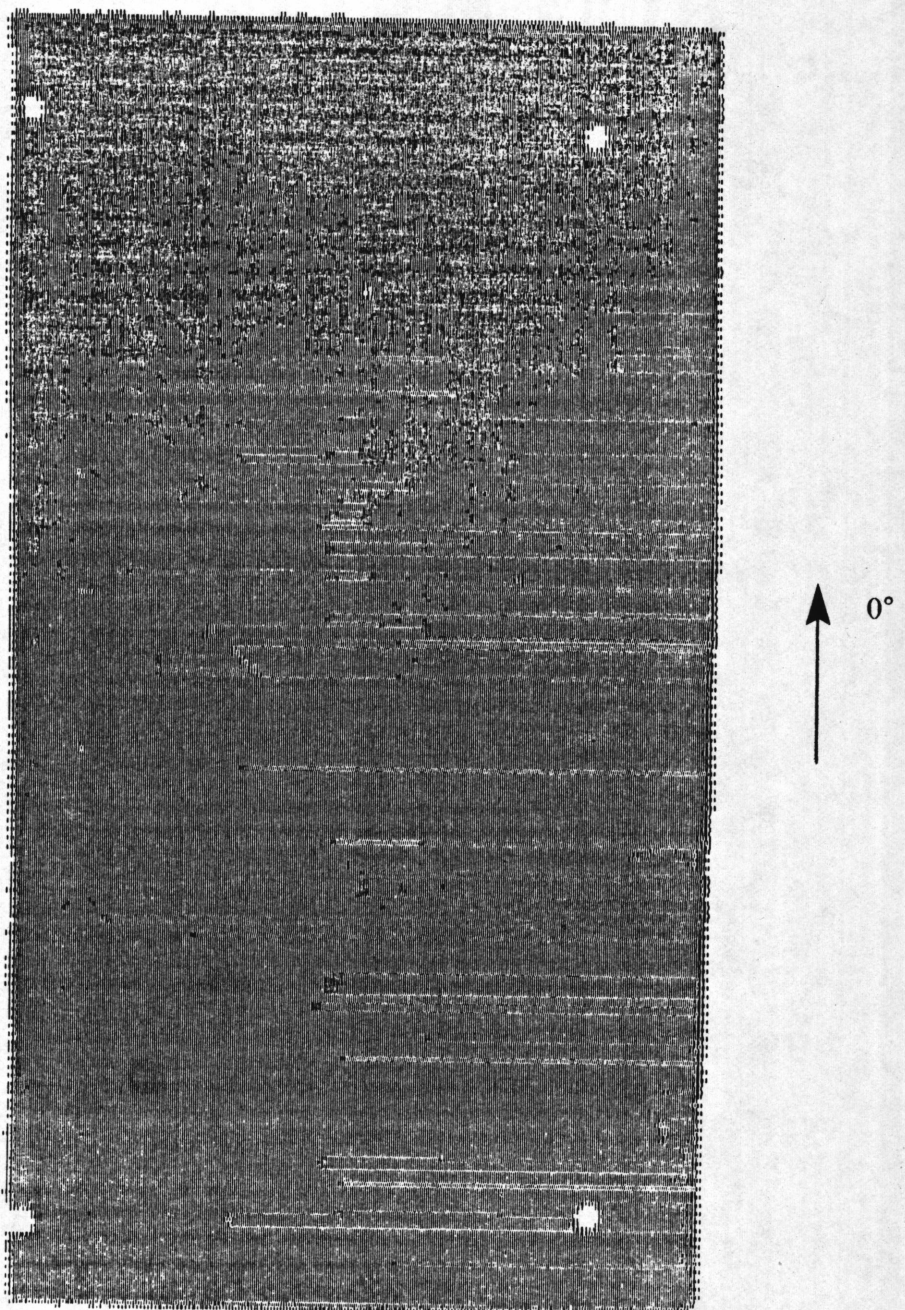


Figure 43. Ultrasonic, gray-scale C-scan of Laminate 5118.

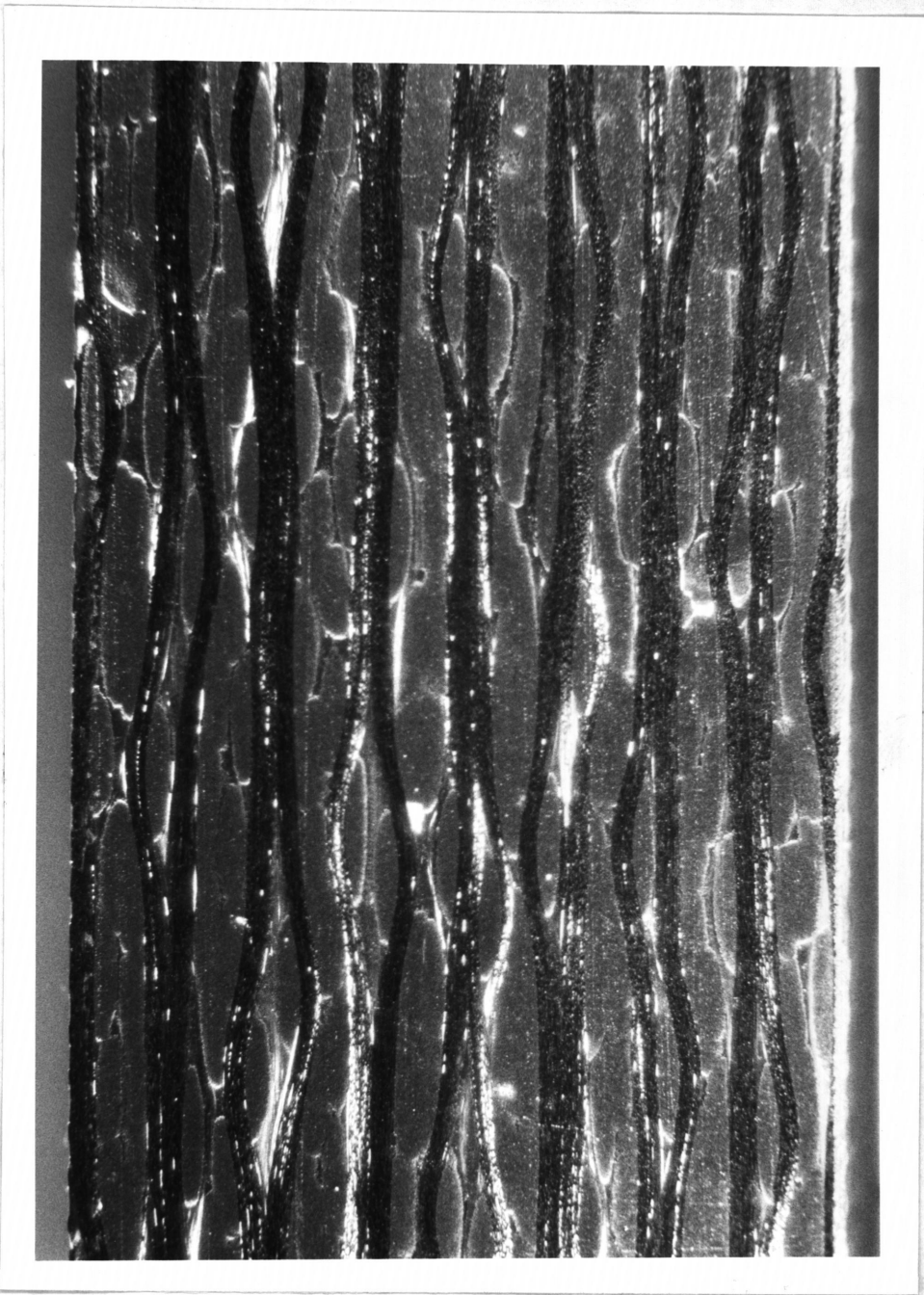
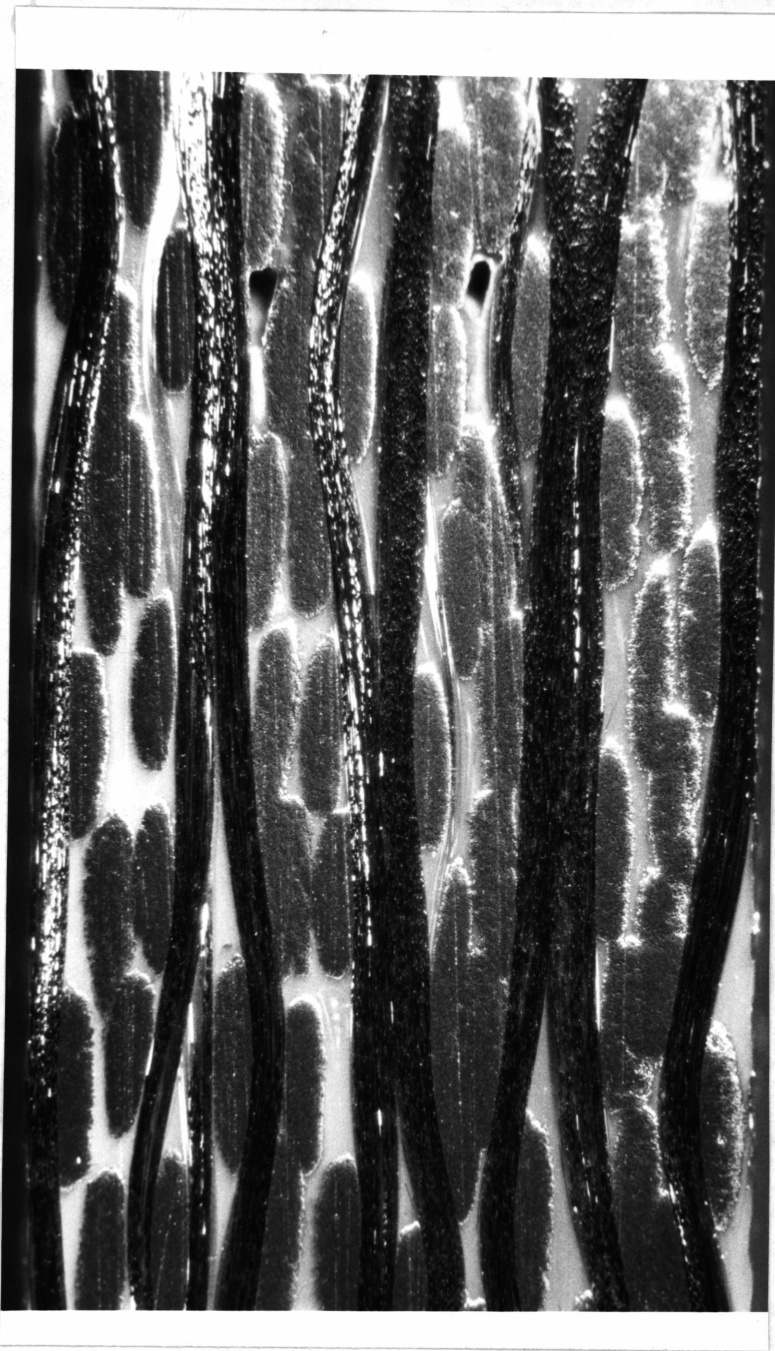


Figure 44. Photomicrograph of Laminate 5118 (8.8 X).



**Figure 45.** Photomicrograph of Laminate 5238 (14.9 X).

### **7.3.2 Volume Fraction Determination**

Three specimens were machined from each cured laminate for volume fraction measurements. Individual results, mean and standard deviations for fiber volume fraction and the cured ply thicknesses are shown in Table 6.

As predicted from the compaction pressures and the photomicrographs, the volume fraction of Laminate 4228 is less than Laminate 4268. Although the two panels were processed with the same compaction pressure, the additional time and temperature cycles required to infiltrate Laminate 4228 might have advanced the crosslinking of polymer chains, thus, preventing complete compaction of the reinforcement. Laminate 4268 was manufactured with porous release cloth which would also lower the total resin volume by allowing excess resin to be bled from the reinforcement.

The measured volume fraction of Laminate 5118 seems to agree with the predictions made in the previous section. The pressure used to manufacture this panel was larger than either of the laminates cured with the Hercules 3501-6 resin system. One possible reason for this discrepancy is that the viscosity of the Hercules 8551-2 resin impeded fluid motion or actually supported a fraction of the applied pressure.

Laminate 5238 was cured at the lowest value of compaction pressure. The photomicrograph and normalized thickness values predict a very small value of volume fraction compared to the other cured laminates. Experimental volume fraction measurements have verified this prediction.

**Table 6. Volume Fraction of Cured Laminates.**

Laminate	Sample Number	Cured Thickness (mm)	$v_f$ (%)	Mean $v_f$ (%)	Standard Deviation (%)
4228	1	0.41125	58.1	58.2	0.1700
	2		58.0		
	3		58.4		
4268	1	0.40625	62.0	62.4	0.3682
	2		62.4		
	3		62.9		
5118	1	0.44438	55.7	56.3	0.4546
	2		56.8		
	3		56.4		
5238	1	0.53375	54.4	54.2	0.1247
	2		54.1		
	3		54.2		

### **7.3.3 Porosity Model Verification**

The volume fractions of the cured test laminates were compared to the pressure-porosity relationship for verification of Equation 3.2.13. Since the laminates were opened for inspection, the compaction characteristics of the second loading cycle were used. Experimental values and results from the porosity model are shown in Figure 46. Experimental data tends to agree with the porosity model.

Data scatter could be attributed to variations in applied pressure and the viscosity near the resin gel point. The applied pressure often drifted by 140 kPa during processing. Repeated fluctuations of the pressure would cause the fabric to acquire more permanent deformation thus decreasing the porosity. When the resin gels, the pressure applied at that time would determine the porosity and not the average pressure.

### **7.3.4 Mechanical Characterization Results**

Each cured laminate was machined into three tensile and four compressive specimens for mechanical characterization. Each specimen was instrumented with electrical resistance strain gages and loaded until the specimen failed. The load versus strain data was examined and the values of elastic modulus, Poisson's ratio, ultimate stress, and ultimate strain were determined. Experimental results were compared to manufacturer's values for AS4/8HS fabric prepregged and cured with Hercules 3501-6 resin.

Differences in reinforcement type between the manufacturer's data and the laminates produced in this study, will be reflected in the mechanical characteristics. Since tensile

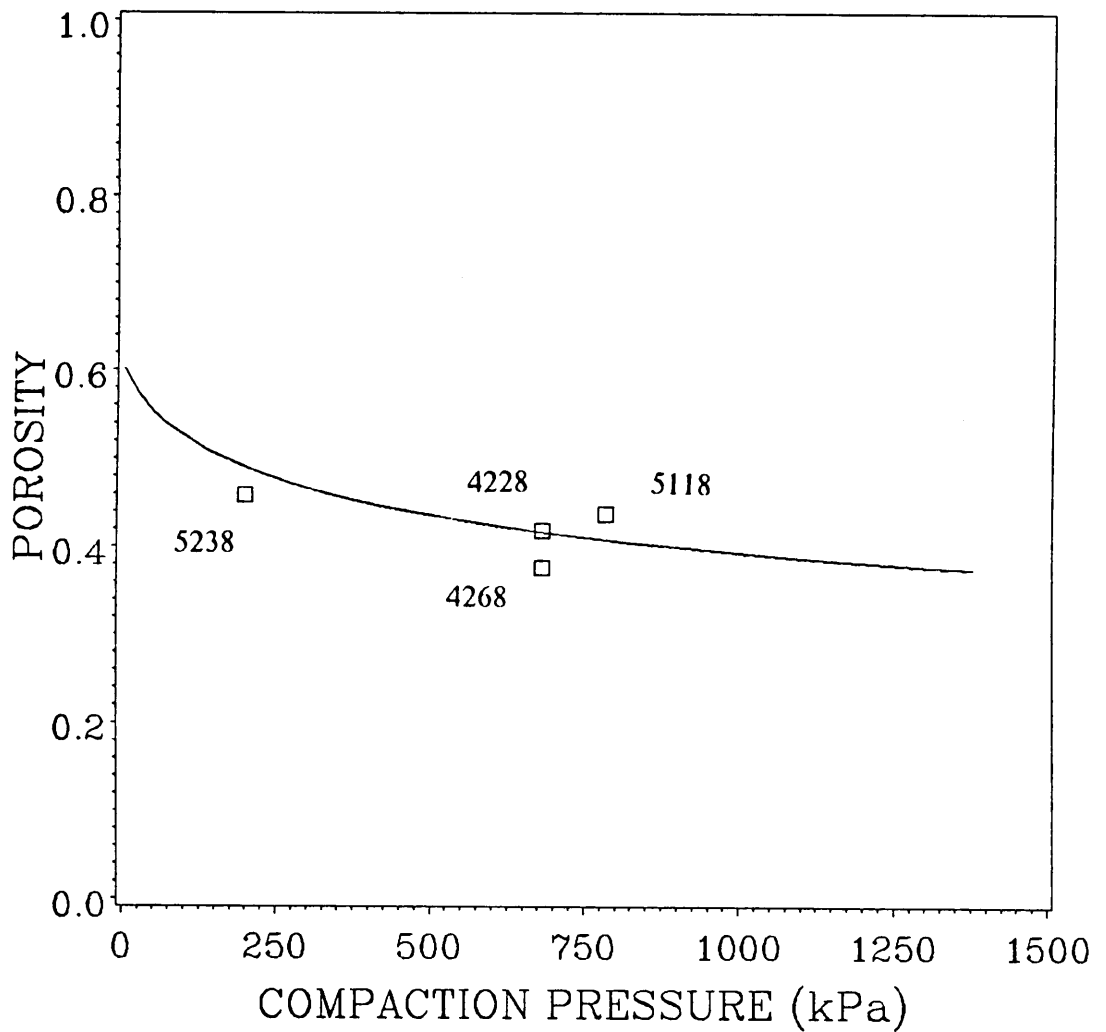


Figure 46. Pressure-porosity model verification.

properties are dominated by the fibers, more discrepancy should be observed for this loading situation. Comparing the mechanical properties supplied by the manufacturer for the IM7 and AS4 fibers, the ratio of IM7 fiber modulus to AS4 fiber modulus is 1.204. Similarly, the ratios of tensile strength and ultimate tensile strain are 1.242 and 1.046 respectively. Fabric styles are also slightly different as shown in Table 1. All mechanical properties for the AS4/8HS, Hercules 3501-6 material system were obtained from laminates with a 62 percent fiber volume fraction.

Results from the tensile tests are summarized in Table 7. With the exception of specimens 5118T2 and 5118T3 which slipped in the grips of the testing machine, all specimens fractured near one or both grips. The strain gages on several specimens failed before the laminate fractured, consequentially, no ultimate strain values were obtained.

Measured values for the tensile elastic modulus are shown in Figure 47. The height of each bar is related to the mean of the experimental data and the cross-hatched portion of the bar represents a "one sigma" variation about the mean so that the accuracy of the mean value can be considered.

The modulus values follow the trend predicted by the fiber volume fraction, ie. larger volume fractions predict larger tensile moduli. Laminate 5238 has an uncharacteristically low modulus which might be attributed to the presence of voids in this laminate. Since the volume fraction of Laminate 4268 is nearly the same as the manufacturer's test sample, and was produced with the same resin system, differences in mechanical response could be due to variations in the reinforcement's mechanical characteristics and differences in processing. Laminate 4268 has a larger tensile modulus than the AS4/8HS laminate.

**Table 7. Mechanical Test Results - Tension.**

Laminate No.	Resin Type	Specimen No.	Elastic Modulus	Poisson's Ratio (GPa)	Ultimate Stress	Ultimate Strain (kPa)	Failure Location (%)
4228	3501-6	4228T1	75.36	0.029	822.6	1.037	end
		4228T2	75.09	0.044	779.8	1.046	end
		4228T3	73.43	0.039	819.1	1.104	end
		Mean	74.60	0.037	807.2	1.062	
4268	3501-6	4268T1	74.40	0.026	898.4	1.168	end
		4268T2	78.33	0.037	877.0	**	end
		4268T3	77.71	0.041	836.4	1.149	end
		Mean	76.81	0.035	870.6	1.159	
5118	8551-7	5118T1	72.19	0.035	893.6	1.164	end
		5118T2	72.88	0.034	903.9	1.168	slip
		5118T3	71.36	0.040	931.5	1.232	slip
		Mean	72.12	0.039	909.7	1.188	
5238	Shell	5238T1	59.43	0.039	804.6	**	end
		5238T2	58.06	0.042	865.3	**	end
		5238T3	56.95	0.038	801.2	1.393	end
		Mean	58.15	0.040	824.0	1.393	-
		Std. Dev.	1.015	0.0017	29.45	-	

\*\* Gage failure prior to ultimate load.

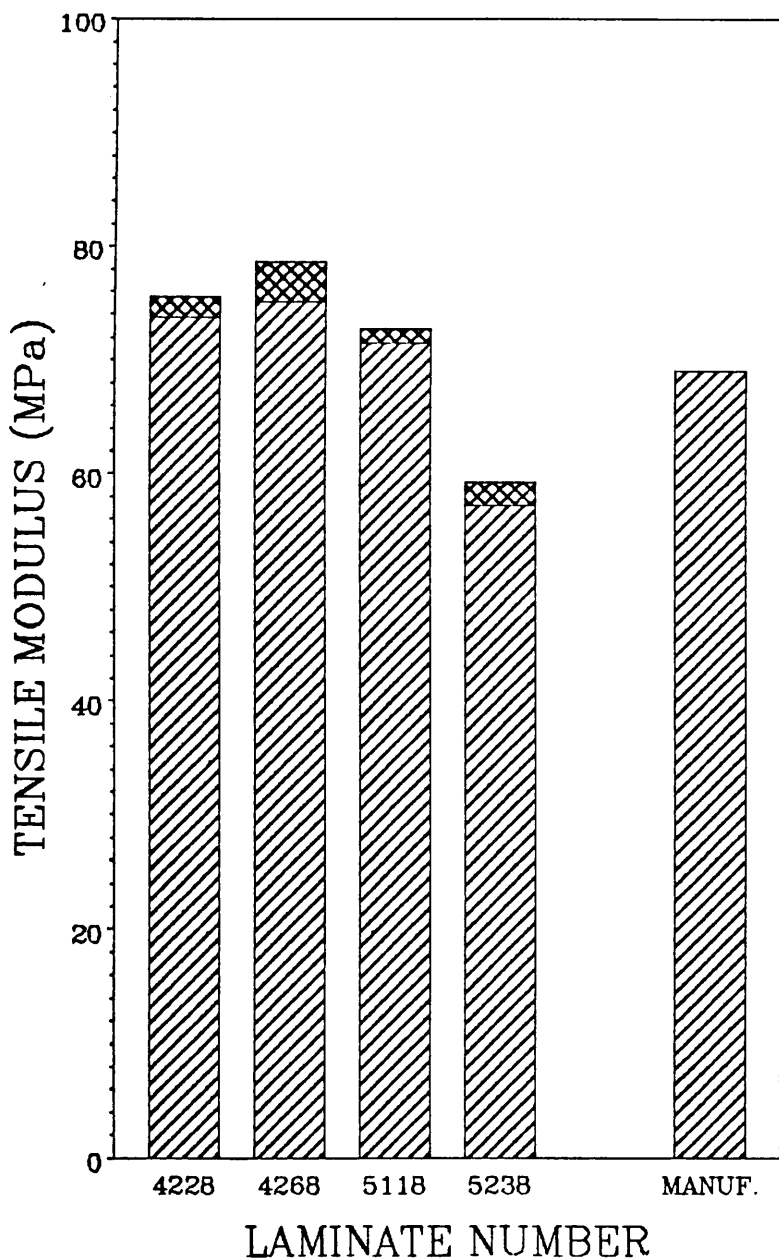


Figure 47. Elastic modulus for tensile loading.

Ultimate tensile stress values are displayed in Figure 48. Strength values for all IM7/8HS laminates are nearly the same and are greater than the strength of the AS4/8HS laminate. Laminate 5118 exhibits the greatest strength value although the volume fraction is relatively low. The increased strength is attributed to the resin system used to produce this laminate.

Ultimate tensile strain values exhibit more variation in magnitude than other tensile mechanical values as shown in Figure 49. Due to premature failure of the bonded strain gauges, standard deviations could not be computed for Laminates 4268 and 5118, and conclusions based on the values shown are subjected to unknown statistical variations. In all cases, the IM7/8HS specimens exhibited a larger value of ultimate tensile strain than the AS4/8HS material. Since the ultimate strain value for individual fibers is nearly the same, the variations in performance can be attributed to fabric construction, resin type, and/or processing conditions.

Mechanical characterization results for the compressive specimens are shown in Table 8. Fracture was observed either at the center or near the loaded edges. Typical edge failures consisted of cracks which were smooth and straight across the width of the laminate and made an angle of 30 to 60 degrees with the laminate-normal direction. When failure occurred at the center of the specimen, the path of the crack through the thickness of the laminate was very irregular. No generalizations could be made about the shape or location of failure based on mechanical properties.

Trends in the compressive moduli are similar to the tensile moduli as shown in Figure 50. Compressive modulus values for Laminate 5238 are much closer to the other IM7/8HS laminates and the manufacturer's values, unlike the tensile modulus values.

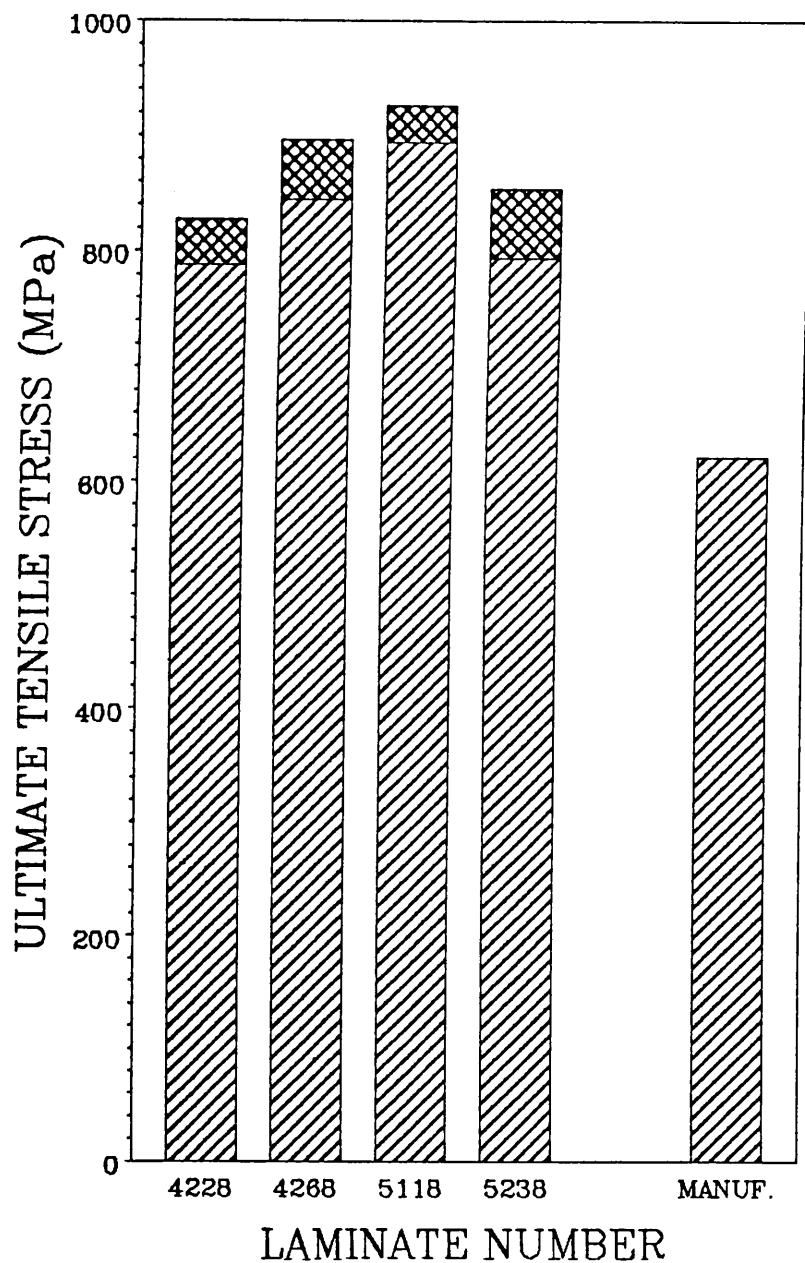


Figure 48. Ultimate tensile stress.

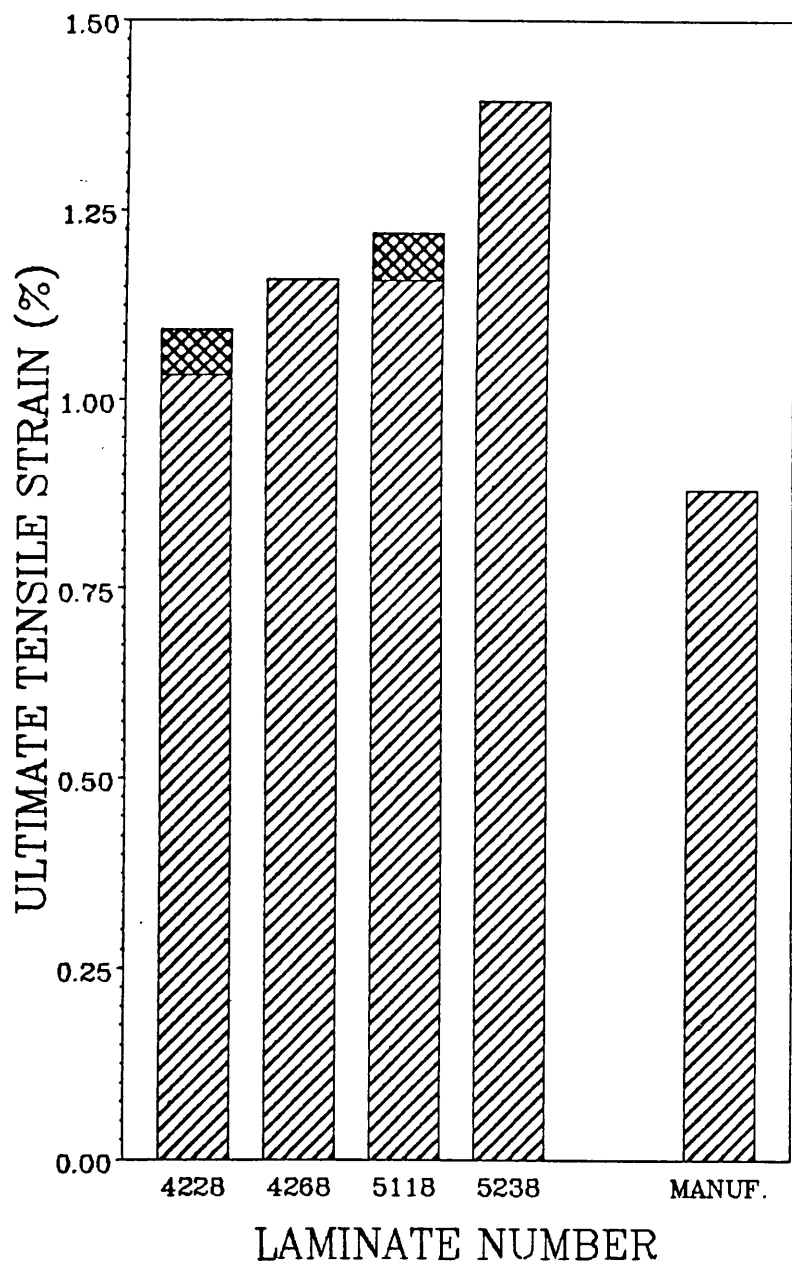


Figure 49. Ultimate tensile strain.

**Table 8. Mechanical Test Results - Compression.**

Laminate No.	Resin Type	Specimen No.	Elastic Modulus	Poisson's Ratio (GPa)	Ultimate Stress	Ultimate Strain (kPa)	Failure Location (%)
4228	3501-6	4228C1	75.71	0.048	645.4	0.969	edge
		4228C2	74.67	0.051	635.7	0.900	center
		4228C3	71.02	0.063	527.5	0.767	center
		4228C4	70.60	0.042	629.5	0.975	center
4268	3501-6	Mean	73.00	0.051	609.5	0.903	
		Std. Dev.	2.224	0.0076	47.71	0.0837	
		4268C1	76.26	0.055	584.7	0.828	center
		4268C2	77.29	0.042	635.0	0.929	center
5118	8551-7	4268C3	78.12	0.040	587.5	0.828	center
		4268C4	79.71	0.040	601.2	0.859	center
		Mean	77.84	0.044	602.1	0.861	
		Std. Dev.	1.261	0.0063	20.02	0.0412	
5238	Shell	5118C1	72.19	0.041	642.6	1.008	edge
		5118C2	72.54	0.042	613.0	0.954	center
		5118C3	71.23	0.048	659.2	1.065	edge
		5118C4	71.36	0.043	650.9	1.043	edge
5238	Shell	Mean	71.83	0.044	641.4	1.018	
		Std. Dev.	0.5502	0.0027	17.43	0.04192	
		5238C1	59.09	0.042	393.7	0.725	center
		5238C2	63.02	0.039	440.6	0.809	edge
5238	Shell	5238C3	64.54	0.029	455.1	0.835	center
		5238C4	61.50	0.042	383.4	0.708	center
		Mean	62.04	0.038	418.2	0.769	
		Std. Dev.	2.012	0.0053	30.31	0.0539	

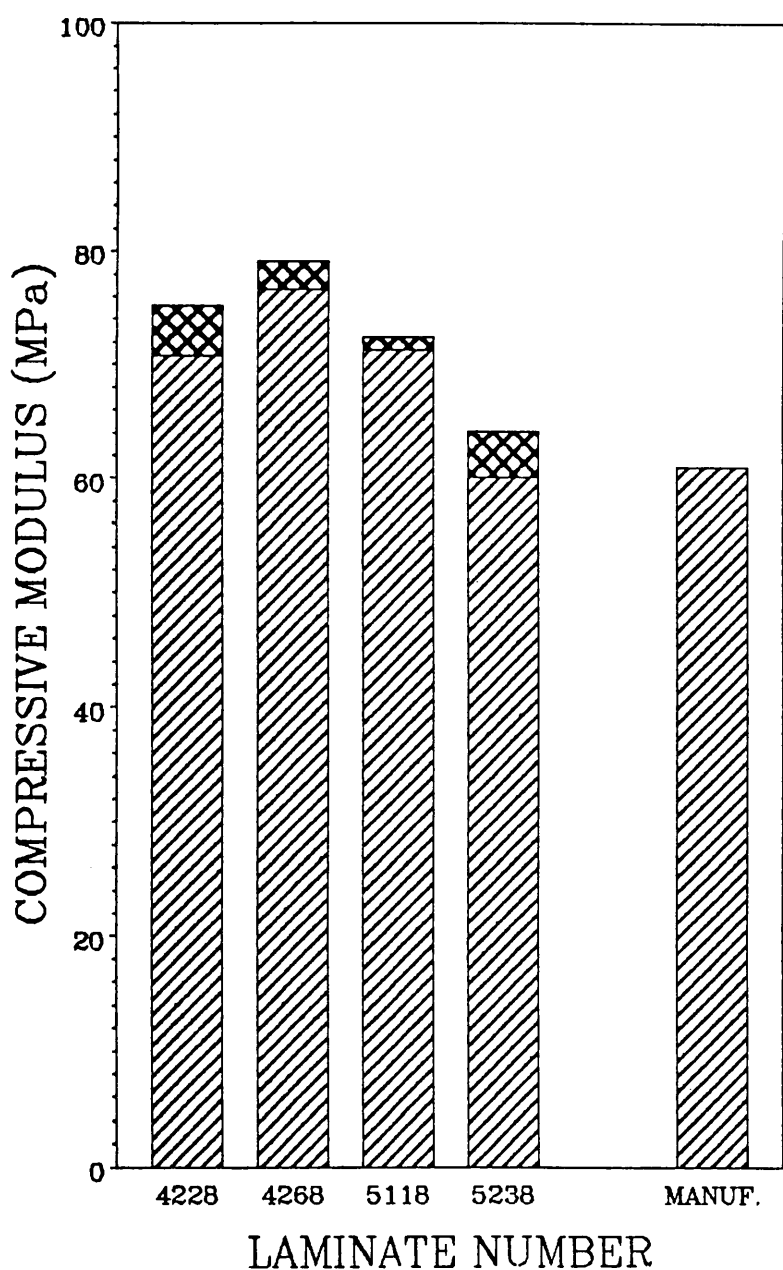


Figure 50. Elastic modulus for compressive loading.

Ultimate compressive stress of the IM7/8HS reinforced composites is less than the ultimate tensile stress. This trend is reversed for the AS4/8HS values as shown in Figure 51. The lower compressive values are expected since this mechanical property is dominated by the matrix material. Laminates 4228 and 4268 correspond to the manufacturer's value of ultimate tensile stress more closely than the compressive stress value. The compressive stress values for laminate 5238 are significantly less than the other IM7/8HS laminates and which is attributed to the presence of voids.

Ultimate compressive strain values follow a similar trend as the ultimate compressive stresses as shown in Figure 52. Laminate 5118 exhibits the largest compressive strain value and the performance of Laminate 5238 appears to be reduced by the presence of voids. In all cases, the AS4/8HS ultimate compressive strain is larger than the values obtained during this study.

The mechanical characterization study has shown that the RTM process can be used to produce high quality composite materials. Although a comparison between like materials was not made, the laminates produced for this study compare favorably with similar materials produced from prepregged fabric.

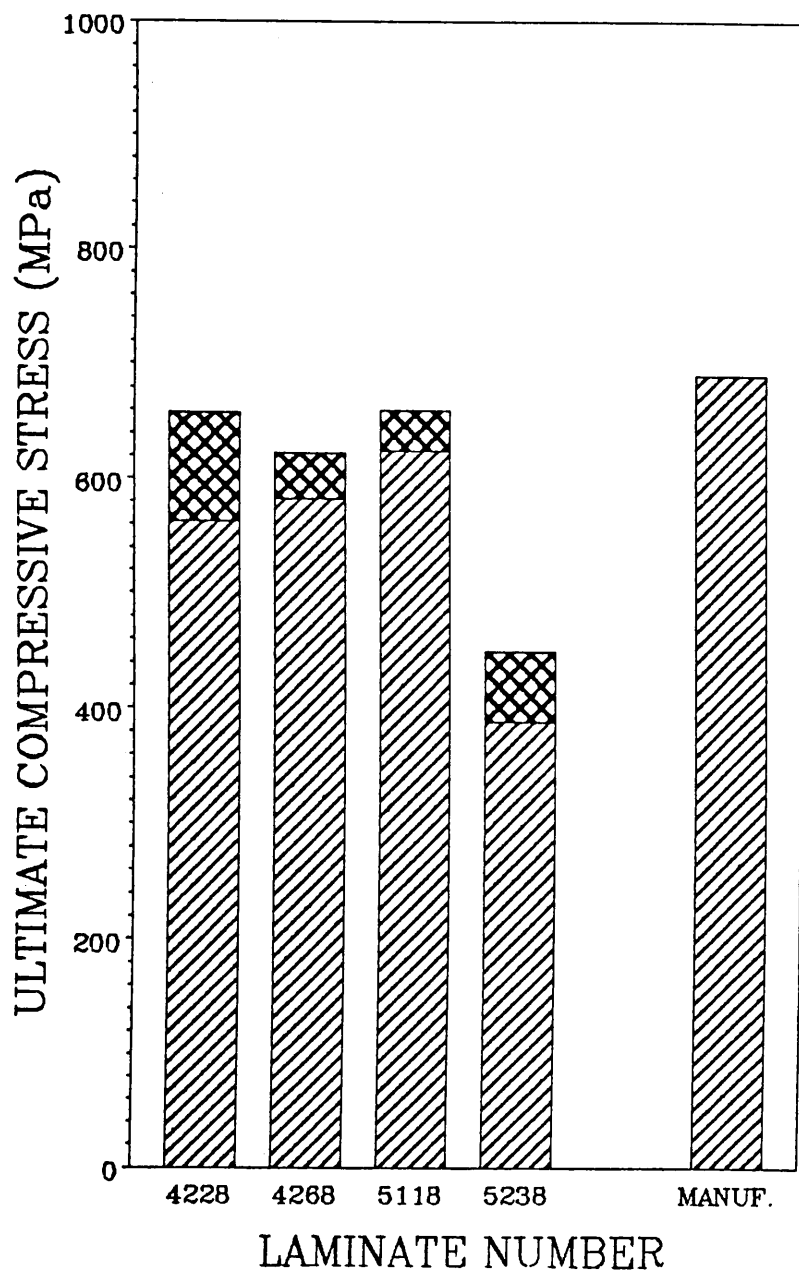


Figure 51. Ultimate compressive stress.

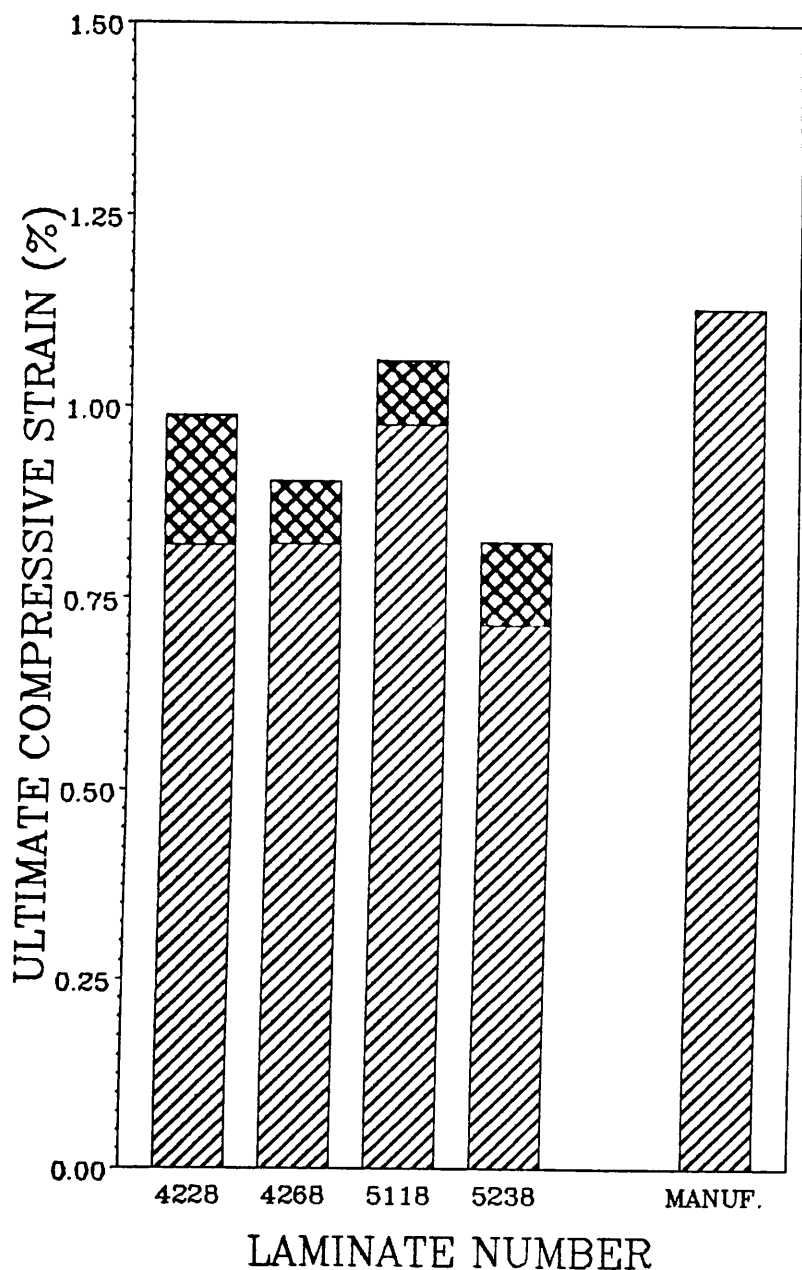


Figure 52. Ultimate compressive strain.

## 8.0 RTM PROCESS SIMULATION

The overall goal of this work has been to develop and verify a processing model for resin transfer molding. The model is intended to be used by engineers and scientists when developing processing cycles from known material properties to eliminate the costly trial-and-error approach to process cycle development. In previous chapters, the development of the process model and numerical solution procedures have been outlined, and numerous portions of the model have been verified experimentally. In the following sections the RTM processing model will be used to investigate the behavior of the IM7/8HS, Hercules 3501-6 material system when subjected to various processing conditions.

When developing a processing cycle, three major questions must be answered: what temperature cycle should be used, what autoclave and vacuum pressures should be used, and how long will the process take? Since the infiltrated fabric behaves like a prepegged material and post-infiltration flow has been neglected, the following investigations are focused on the infiltration process. A series of three parametric studies have been completed which examine the effects of autoclave pressure, isothermal infiltration temper-

ature and heating rate on the infiltration time. Additional investigations include a ramp-hold temperature profile on the infiltration characteristics of a thick reinforcement, and a comparison between the processing model and the actual production of Laminate 4268.

## 8.1 PARAMETRIC STUDY: AUTOCLAVE PRESSURE

This study examines the effect of the autoclave pressure on the infiltration time. In each simulation, the characteristics of 16 plies of IM7/8HS fabric and Hercules 3501-6 resin were used to simulate infiltration at a constant temperature of 100°C. The vacuum bag infiltration procedure was simulated with a vacuum pressure of approximately -100 kPa and the autoclave pressure was varied between 0 and 1400 kPa. As discussed in Section 5.2, the autoclave and vacuum pressures compact the material and drive the flow.

The normalized position of the infiltration front, defined as the distance that the resin has progressed divided by the thickness of the reinforcement, is plotted versus time in Figure 53 for several autoclave pressures. Initially, the infiltration is independent of autoclave pressure. When approximately 20 percent of the material is infiltrated, the lower pressure simulations begin to take progressively longer to infiltrate the reinforcement. In each case, the rate of infiltration, ie. the slope of the infiltration profile, decreases due to a drop in the pressure gradient caused by the increasing infiltration length.

In general, the viscosity and degree of cure will change with time due to the chemical reactions within the resin. Since the infiltration times, ie. the time required to completely saturate the material with resin, are very short for these simulations, the viscosity does

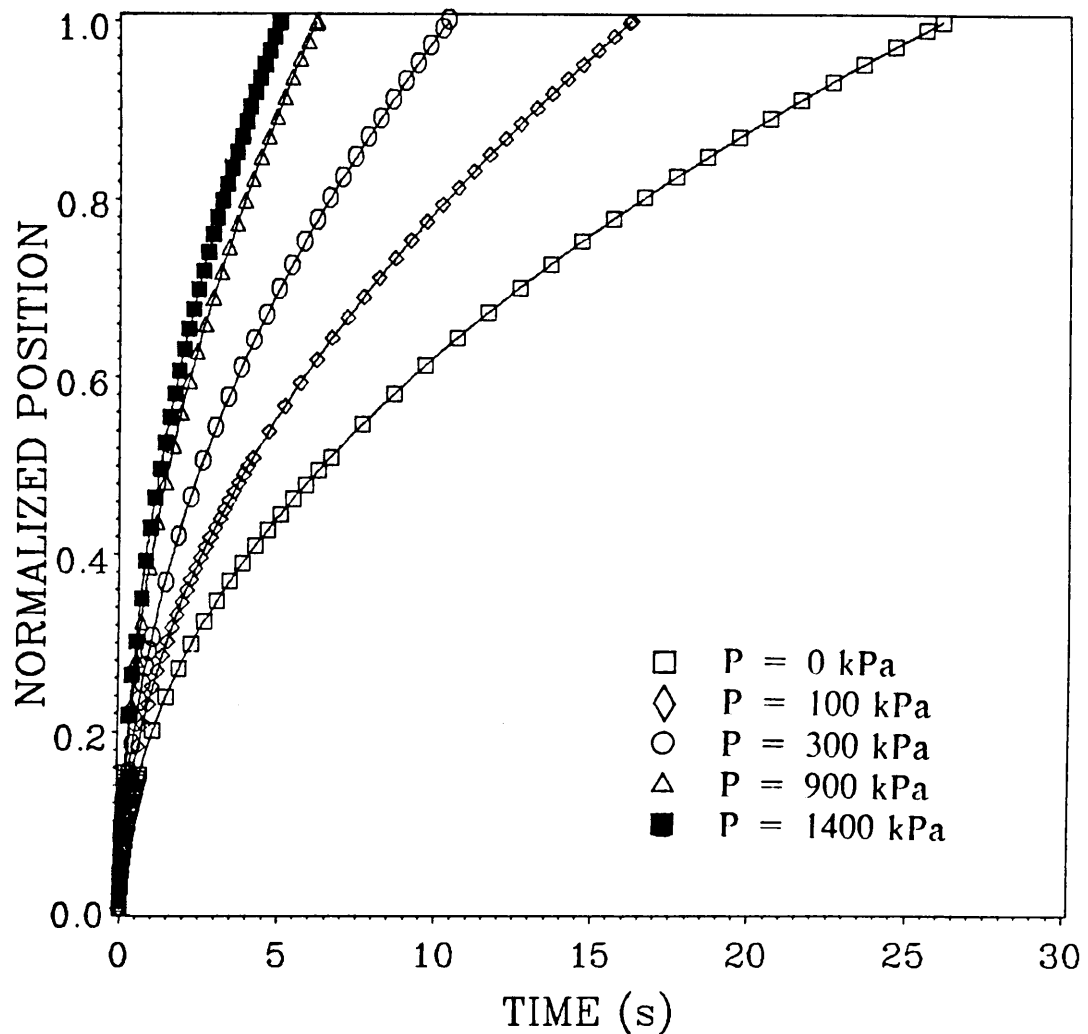


Figure 53. Selected infiltration profiles used for the pressure parametric study.

not change appreciably. The thickness, porosity and infiltration times for each simulation are listed in Table 9.

Increasing the autoclave pressure decreases the thickness, porosity and permeability of the reinforcement. Infiltration time is plotted versus the autoclave pressure in Figure 54. The infiltration time decreases with increasing pressure, indicating the autoclave pressure effects the pressure drop more than the permeability. This effect is most apparent between 0 and 600 kPa when the infiltration time decreases by 50 percent.

## 8.2 PARAMETRIC STUDY: ISOTHERMAL INFILTRATION

This study examined the effects of isothermal infiltration temperature on the infiltration time of the 16 ply IM7/8HS, Hercules 3501-6 material system. The vacuum bag infiltration technique was simulated with full vacuum pressure (-100 kPa) and autoclave pressures of 0, 200, 500, and 1400 kPa. Isothermal infiltration temperatures were varied between 75 and 175°C .

As with the pressure parametric study, the infiltration times calculated during this study will not cause the viscosity of the resin to change significantly. As expected, the shape of the infiltration profiles shown in Figure 55 are similar to the pressure parametric study. Infiltration times and viscosities for each combination of temperature and pressure are listed in Table 10.

**Table 9. Selected Results from the Pressure Parametric Study.**

Autoclave Pressure (kPa)	Thickness ( $\times 10^{-3}$ m)	Porosity (%)	Infiltration Time (s)
0	8.302	52.43	26.10
100	7.732	48.85	16.18
200	7.405	46.57	12.37
300	7.177	44.87	10.33
500	6.869	42.40	8.159
700	6.664	40.63	6.958
900	6.516	39.28	6.114
1100	6.402	38.20	5.562
1400	6.274	36.93	4.944

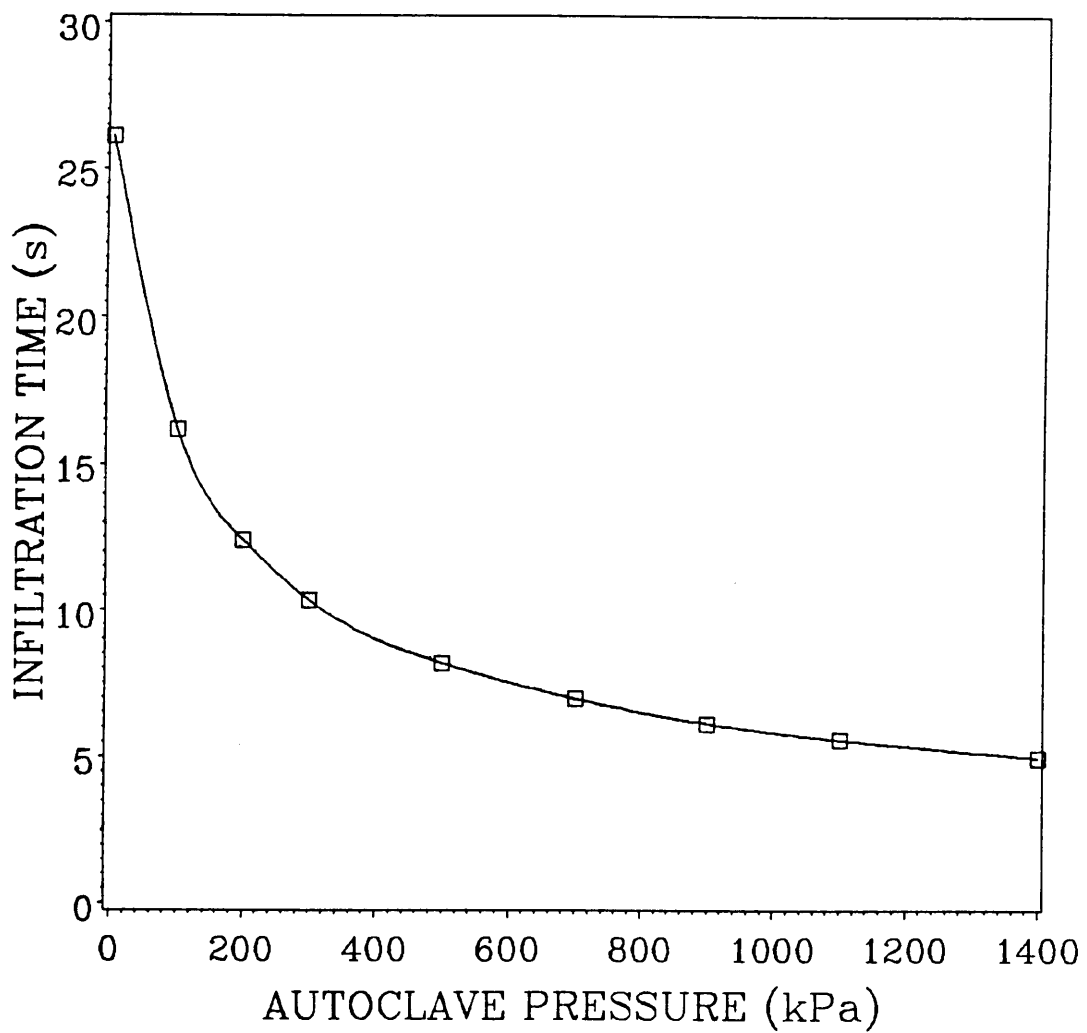


Figure 54. Results from the pressure parametric study.

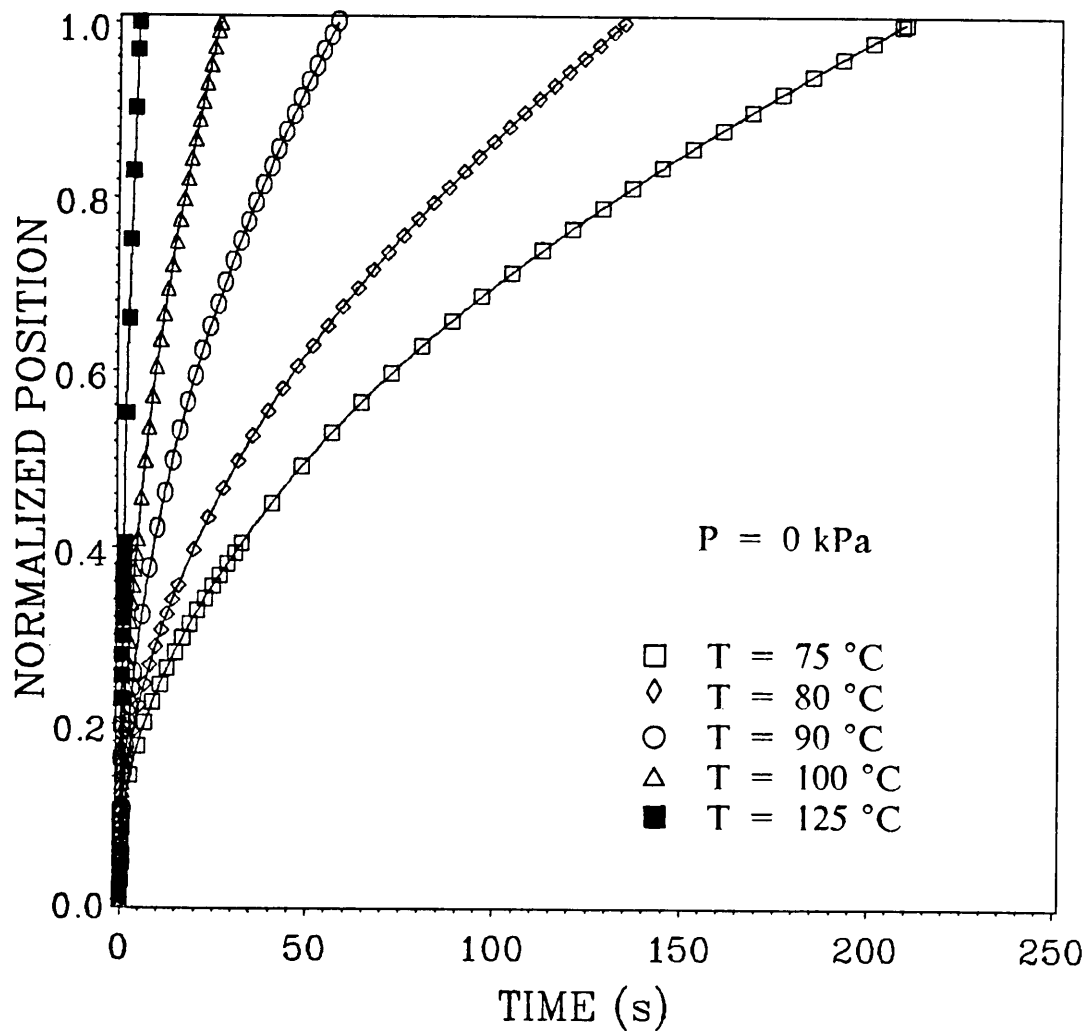


Figure 55. Selected infiltration profiles used for the isothermal infiltration parametric study.

**Table 10. Selected Results from the Isothermal Infiltration Parametric Study.**

Autoclave Pressure (kPa)	Isothermal Temperature (°C)	Viscosity ( $\times 10^{-3}$ Pa s)	Infiltration Time (s)
0	75	3454.	209.4
	80	2214.	134.1
	90	943.9	57.31
	100	421.2	25.72
	125	66.91	3.899
	150	13.20	0.7663
	175	3.124	0.1922
200	75	3452.	100.8
	80	2213.	63.78
	90	943.6	27.23
	100	421.1	12.38
	125	66.88	1.943
	150	13.20	0.3839
	175	3.124	0.09110
500	75	3452.	67.13
	80	2213.	42.92
	90	943.5	18.09
	100	421.0	8.123
	125	66.88	1.294
	150	13.20	0.2566
	175	3.124	0.06043
1400	75	3452.	40.62
	80	2213.	25.95
	90	943.4	11.02
	100	421.0	4.972
	125	66.87	0.7881
	150	13.20	0.1521
	175	3.124	0.03529

The effect of temperature on the infiltration time is shown in Figure 56. Temperature and pressure have a significant effect on the total infiltration time between 75 and 100°C. In this interval, the infiltration time for each simulated autoclave pressure decreases by an order of magnitude due to changes in resin viscosity. Above 125°C, the dependence of the infiltration time on the temperature and pressure is greatly reduced.

### 8.3 PARAMETRIC STUDY: HEATING RATE

Typical processing cycles begin by raising the temperature of the material system from ambient conditions at a constant rate to a hold temperature. This study was initiated to investigate the effect of heating rate on the infiltration time using the same material system and pressure conditions as in the previous section. In each simulation, 18°C was used as the initial temperature and the heating rate was varied between 0.5 and 5.0°C/min. Large hold temperatures were used to ensure infiltration occurred during the heating cycle.

A fundamental difference in the shape of the infiltration profile was observed for these simulations. Since the temperature was not changing in the previous simulations, the viscosity of the fluid was constant throughout infiltration. As shown in Figure 57, the changing temperature causes the fluid to accelerate within the material during cure which alters the shape of the infiltration profile. Due to larger initial viscosities, infiltration times at least one order of magnitude greater than the isothermal simulations were predicted. The time-temperature history of these simulations does not allow the resin to crosslink appreciably and additional heat and time are required to complete the cure.

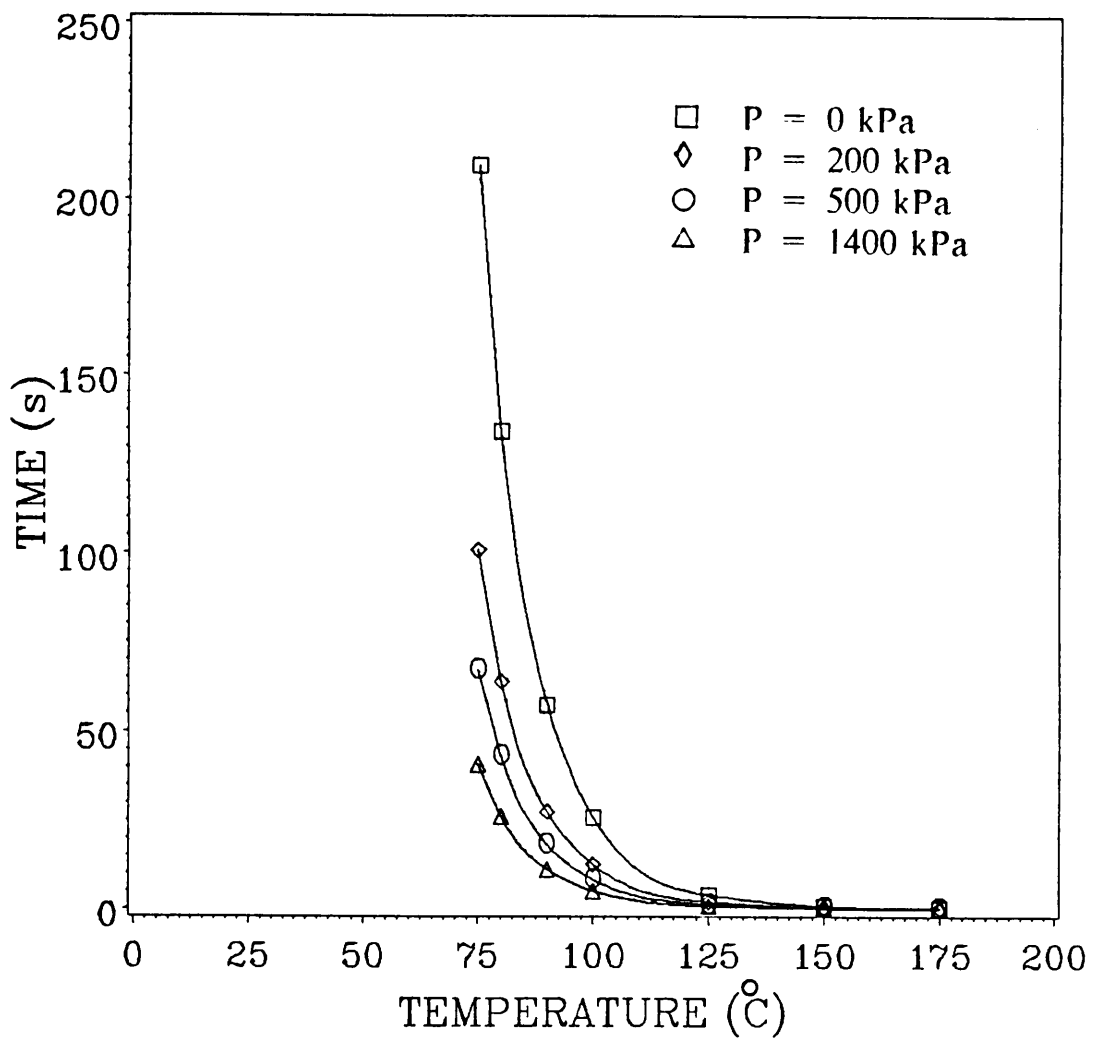


Figure 56. Results from the isothermal temperature parametric study.

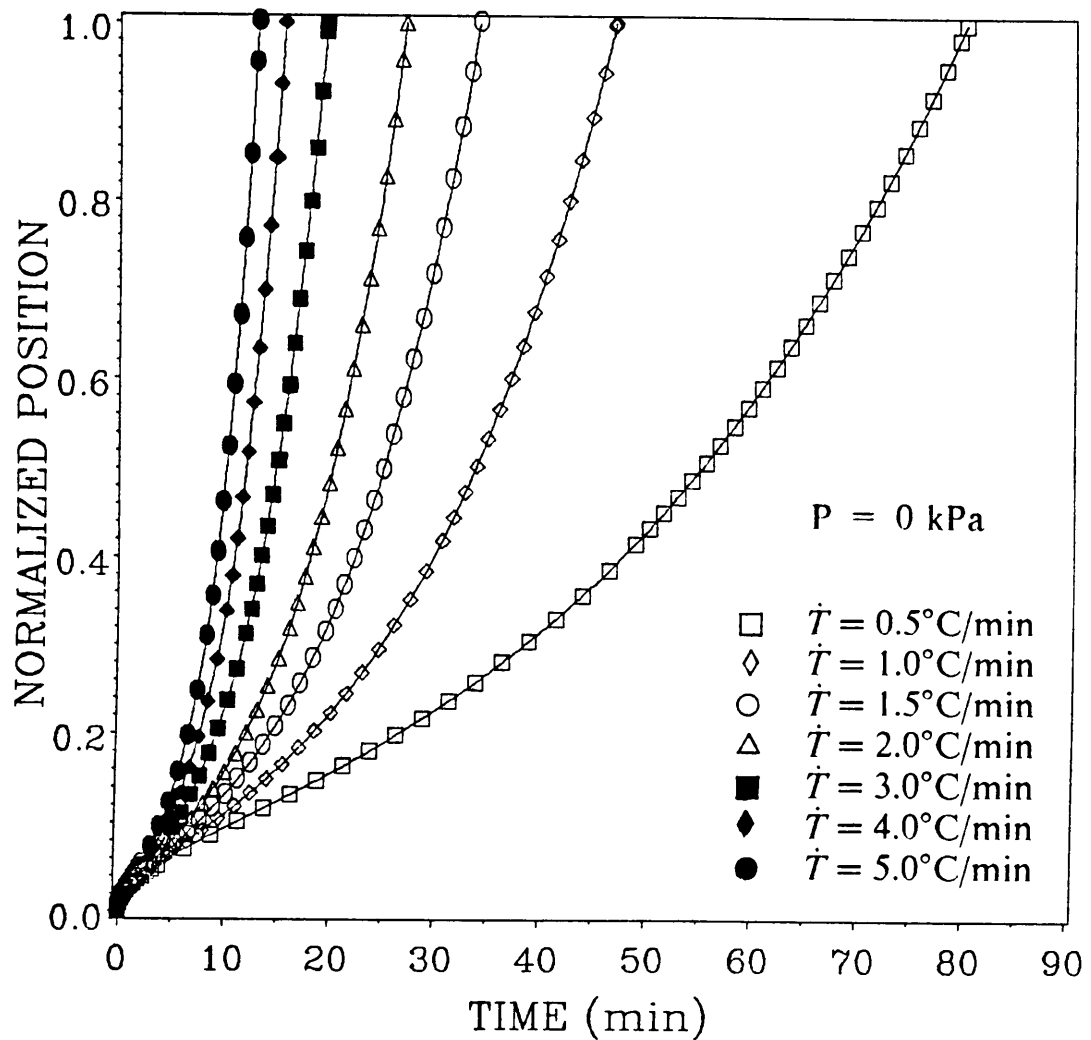


Figure 57. Selected infiltration profiles used for the heating rate parametric study.

The manufacturer's recommended cure cycle for this resin system involves heating the material from ambient conditions at 2.2°C/min to a 93°C hold temperature. After 70 minutes the material is heated to 177°C at the same rate and held for an additional 120 minutes. Results shown in Table 11 for the final temperature, defined as the temperature when the laminate is completely infiltrated, indicate the material will be completely infiltrated before the manufacturer's first hold temperature is reached. Temperature and pressure combinations used during this study suggest that the recommended cure cycle could be used without modification to produce composite laminates by RTM.

The dependence of the infiltration time on the heating rate and autoclave pressure shown in Figure 58, is similar to the trends in the isothermal results. The infiltration time is a strong function of heating rate for low rates (< 2.0°C/min), and decreases as the heating rate increases. Infiltration time is much less dependent on the autoclave pressure in this study than in the isothermal simulations.

## 8.4 THICK LAMINATE STUDY

This study was initiated to attempt to determine some of the limits of laminate production by RTM. Specifically, infiltration of a 100 ply laminate was simulated to determine whether the resin would infiltrate the reinforcement or gel prematurely. A vacuum pressure of -100 kPa was used to drive the flow and compact the plies. The temperature cycles used during these simulations consisted of a 5°C/min ramp from 20°C to a hold temperature of 50, 75, 100, and 150°C. Thickness and material porosity were estimated to be 5.2 cm and 48 percent respectively.

**Table 11. Selected Results from the Heating Rate Parametric Study.**

Autoclave Pressure (kPa)	Temperature Rate (°C/min)	Final Temperature (°C)	Infiltration Time (s)
0	0.5	58.04	4805
	1.0	64.76	2806
	1.5	68.83	2033
	2.0	71.76	1613
	3.0	75.96	1159
	4.0	79.11	916.7
	5.0	81.56	763.1
200	0.5	51.08	3969
	1.0	57.44	2366
	1.5	61.30	1732
	2.0	64.12	1384
	3.0	68.13	1003
	4.0	71.10	796.4
	5.0	73.46	665.5
500	0.5	47.59	3545
	1.0	53.78	2147
	1.5	57.42	1577
	2.0	60.20	1266
	3.0	64.12	922.4
	4.0	67.03	735.5
	5.0	69.34	616.1
1400	0.5	43.15	3018
	1.0	49.14	1868
	1.5	52.77	1391
	2.0	55.36	1121
	3.0	59.22	824.3
	4.0	62.05	660.7
	5.0	64.30	555.5

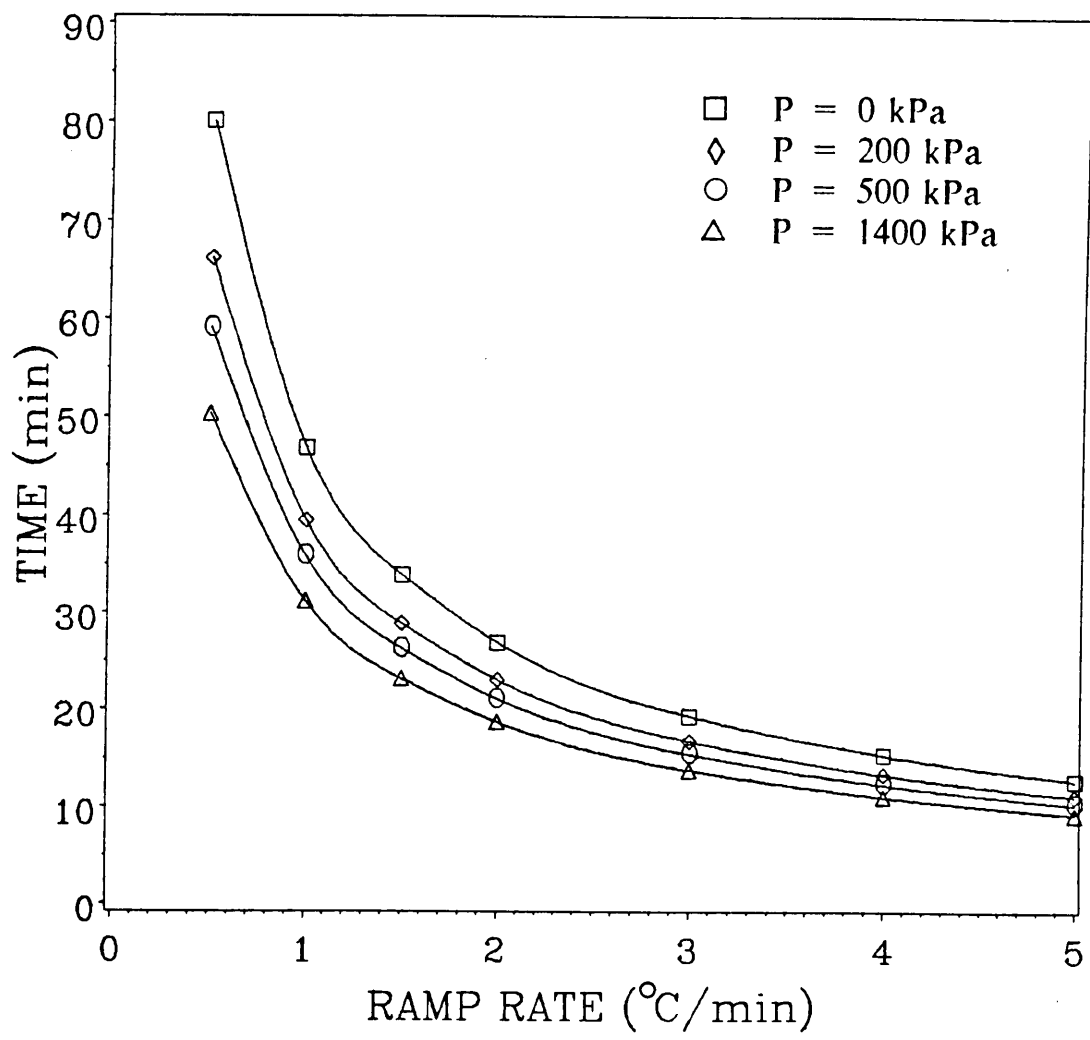


Figure 58. Results from the heating rate parametric study.

In all simulations, infiltration was completed just after reaching minimum viscosity. As in the isothermal infiltration study, the larger hold temperatures resulted in shorter infiltration times. If the conditions of this study were adopted, the manufacturer's cure cycle would need to be altered to achieve complete infiltration. A summary of results for this study is shown in Table 12.

## 8.5 MODEL VERIFICATION

To check the accuracy of the infiltration and cure models, a simulation of the production of Laminate 4268 was performed. This laminate was constructed from Hercules 3501-6 and IM7/8HS fabric as described in Section 6.4.2. After the 93°C hold for 30 minutes, the manufacturer's temperature cycle was initiated to complete the cure of the laminate.

The process model predicted that infiltration was completed approximately 18.5 minutes after the initial heating cycle was begun, as shown by the infiltration profile in Figure 59. The simulation was continued after infiltration to obtain the complete temperature, degree of cure and viscosity history shown in Figure 60. Final resin cure was predicted during the latter stages of the third temperature hold with little exothermic heat generation occurring during cure.

The processing simulation and experimental results are compared in Table 13. The slight discrepancy in the resin mass, thickness, and volume fraction could be attributed to improper control of the applied platen pressure during cure. Progress of the actual resin infiltration could not be observed during the experiment, therefore an accurate value of the experimental infiltration time could not be determined.

**Table 12. Selected Results from the Thick Laminate Parametric Study.**

Hold Temperature (°C)	Final Degree of Cure (%)	Infiltration Time (min)
50	22.75	6868.
75	15.09	340.0
100	13.11	53.65
150	12.66	23.25

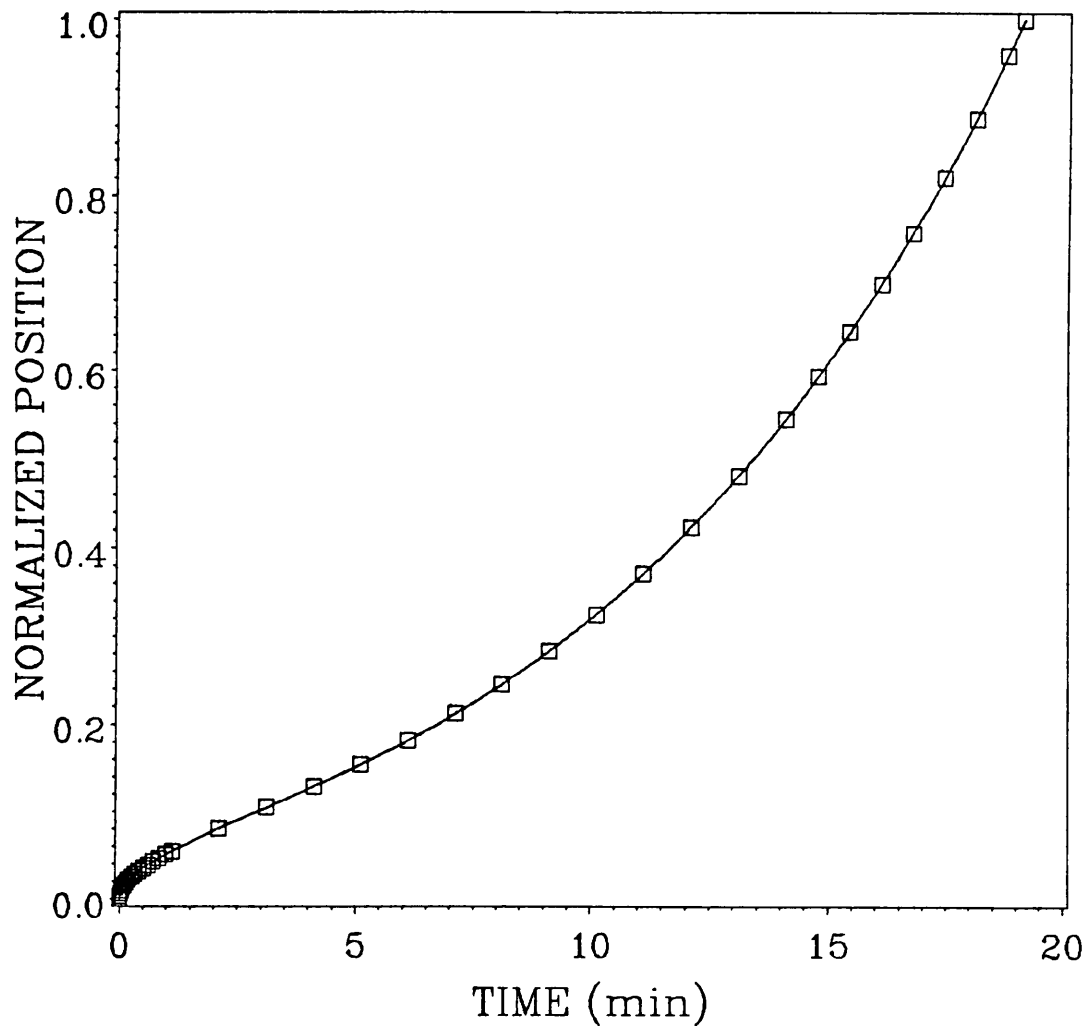


Figure 59. Infiltration profile for the simulation of Laminate 4268.

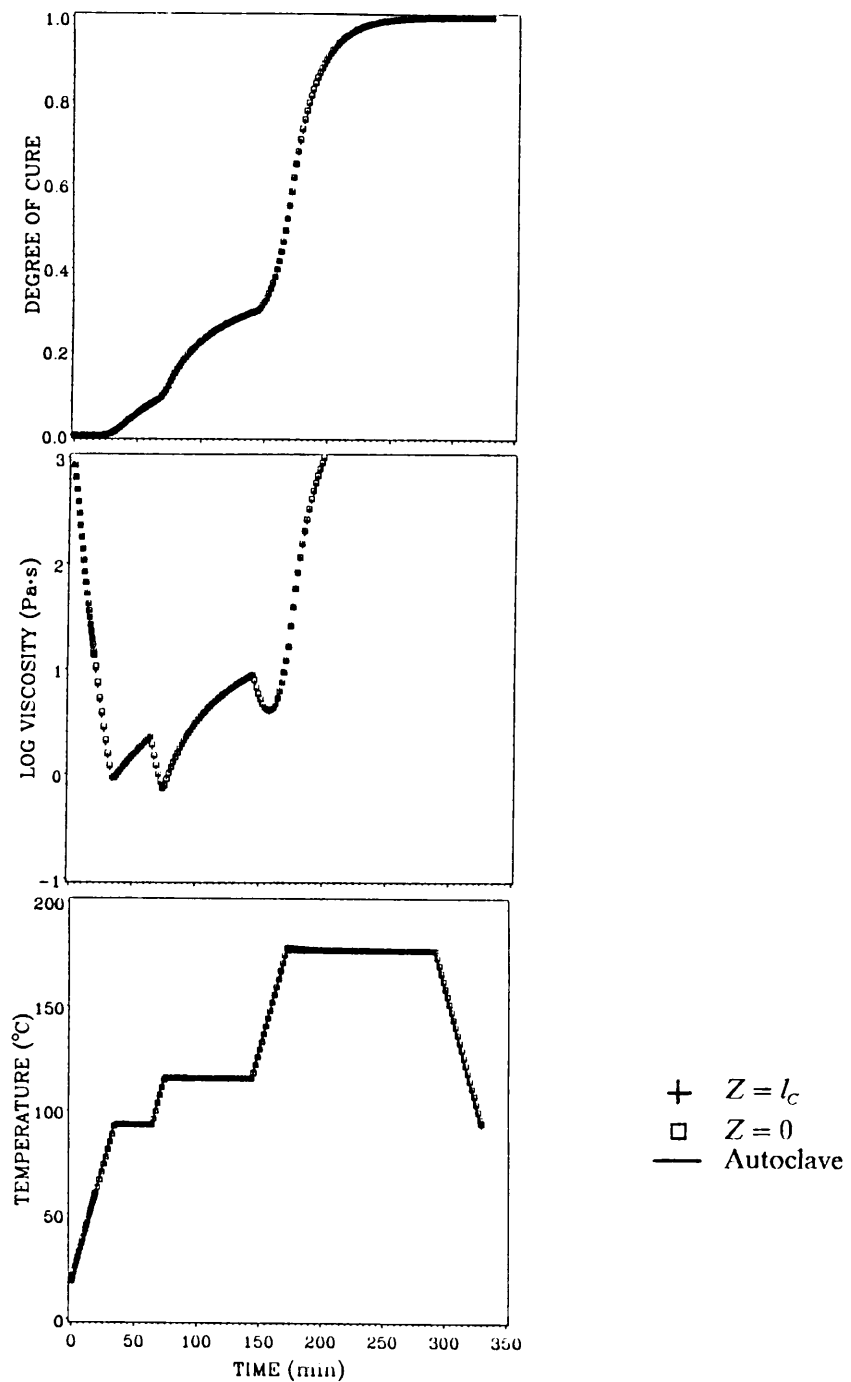


Figure 60. Temperature, viscosity and degree of cure profiles for the simulation of Laminate 4268.

**Table 13.** RTM Processing Model Verification Study.

	Prediction	Experiment
Infiltration Time	18.5 min	< 65 min
Resin Mass	247 g	214 g
Thickness	6.8 mm	6.5 mm
$v_f$	58%	62%

## **9.0 CONCLUSIONS AND FUTURE WORK**

### **9.1 CONCLUSIONS**

This work has shown that it is possible to accurately model the resin transfer molding method of composite materials fabrication. Infiltration can be described, in a quasi-steady state, as the flow of a Newtonian viscous fluid through a porous material. Post-infiltration cure processes can be described with existing models developed for prepregged materials.

Compaction of wet and dry IM7/8HS fabric can be described by a nonlinear polynomial expression which was empirically developed. Deformation is due to motions between and within individual fiber tows. Nesting of individual layers is negligible for the materials studied. The AS4/8HS and IM7/8HS fabrics acquire permanent deformation during repeated compaction cycles with the greatest amount of deformation occurring during the first cycle. Path dependence and multi-cycle loading can be simulated with the compaction model by employing a translational matching scheme at the load re-

versal points. The compaction behavior of IM7/8HS is fundamentally different when saturated with water than when it is dry.

Using the developed compaction model and Gauvin *et al.* [12] expression for material porosity in terms of the fiber bed thickness, the applied pressure was used to accurately predict the porosity of IM7/8HS. Measurements of fiber volume fraction in the cured laminates were within 3 percent of the predicted values.

Flow rate-pressure gradient measurements for IM7/8HS saturated with water, tend to follow D'Arcy's law when liquid-solid surface interactions are neglected. Through-the-thickness permeabilities calculated from the experimental flow rate-pressure gradient data compare favorably with the current literature in magnitude, but exhibit significant data scatter. Permeability values can be described in terms of the porosity by the Kozeny-Carman expression. Inplane permeabilities could not be accurately measured since uniform flow through the fabric could not be established.

Nondestructive examination of cured laminates is very helpful when predicting final fiber volume fractions and mechanical performance. Ultra-sonic gray scale C-scans accurately located a group of voids in Laminate 4228. Through-the-thickness photomicrographs were useful when locating and identifying voids, and predicting relative laminate mechanical performance on the basis of fiber volume fraction. Performance of laminates produced by RTM, based on elastic mechanical measurements, is comparable to laminates produced with current prepreg technology.

Infiltration time is a function of the applied pressure and the time-temperature history of the resin. Proper choice of these parameters can affect the efficiency of the processing cycle. Applied pressures between 0 and 1400 kPa were simulated with the infiltration

model and the infiltration time was estimated to decrease with increasing pressure. Infiltration temperature has a much stronger influence on the infiltration time. An increase of 75°C has been shown to decrease the total infiltration time by two orders of magnitude. The processing model can also identify combinations of temperature and pressure which would result in incomplete infiltration and cure of the composite laminate.

## 9.2 FUTURE WORK

The following areas are recommended for future work:

1. Experimentally determine the position of the infiltration front as a function of time and compare this information with the processing model.
2. Expand and verify the processing model to include unsteady heat transfer during infiltration.
3. Expand and verify the processing model to include applied pressure variations (consolidation) during infiltration.
4. Expand and verify the processing model to describe two-dimensional infiltration.
5. Develop a data base of textile and resin material characteristics.

## 10.0 BIBLIOGRAPHY

1. Lindt, J.T., "Engineering Principles of the Formation of Epoxy Resin Composites", **SAMPE Quarterly**, Vol. 14, No. 1, Oct. 1982, pp. 14-19.
2. Rice, P.A., Fontugne, D.J., Latini, R.G., and Barduhn, A.J., "Anisotropic Permeability in Porous Media", in *Flow Through Porous Media*, American Chemical Society, Washington, 1969, pp. 48-56.
3. Coulter, J.P., Smith, B.F., and Güçeri, S.I., "Experimental and Numerical Analysis of Resin Impregnation During the Manufacturing of Composite Materials", **Proceedings of the American Society for Composites Second Technical Conference**, University of Delaware, Sept. 23-25, 1987, pp. 209-217.
4. Martin, G.Q., and Son, J.S., "Fluid Mechanics of Mold Filling for Fiber Reinforced Plastics", **Advanced Composites: The Latest Developments, Proceedings of the ASM/ESD Second Conference on Advanced Composites**, Dearborn Michigan, Nov. 18-20, 1986, pp. 149-157.
5. Gutowski, T.G., Kingery, J., and Boucher, D., "Experiments in Composites Consolidation: Fiber Deformation", **Society of Plastics Engineers, 44th Annual Technical Conference**, Boston, April 28-May 1, 1986, pp. 1316-1320.
6. Hou, T.H., "A Resin Flow Model for Composite Prepreg Lamination Process", **Society of Plastics Engineers, 44th Annual Technical Conference**, Boston, April 28-May 1, 1986, pp. 1300-1305.
7. Gutowski, T.G., "A Resin Flow/Fiber Deformation Model for Composites" **SAMPE Quarterly**, Vol. 16, No. 4, July, 1985.
8. Dave, R., Kardos, J.L., and Duduković, M.P., "A Model for Resin Flow During Composite Processing: Part 1-General Mathematical Development", **Polymer Composites**, Vol. 8, No. 1, Feb. 1987, pp. 29-38.
9. Davis, E.H., and Raymond, G.P., "A Non-linear Theory of Consolidation", **Geotechnique**, Vol. 15, No. 2, June 1965, pp. 161-173.

10. Williams, J.G., Donnellan, R.E., and Trabocco, R.E., "A Predictive Model for Resin Flow Behavior During Composite Processing", Naval Air Development Center, Final Report, NADC-85164-60.
11. Williams, J.G., Donnellan, R.E., and Trabocco, R.E., "Experimental Verification of the Naval Air Development Center Composite Resin Flow Model", Naval Air Development Center, Final Report, NADC-86048-60.
12. Gauvin, R., Chaibani, M., and LaFontaine, P., "The Modeling of Pressure Distribution in Resin Transfer Molding" 41st Annual Conference Reinforced Plastics/Composites Institute, The Society of the Plastics Industry, Inc., Jan. 27-31, 1986.
13. Adams, K.L., Miller, B., and Rebenfeld, L., "Forced In-Plane Flow of an Epoxy Resin in Fibrous Networks", *Polymer Engineering and Science*, Vol. 26, No. 20, Nov. 1986, pp. 1434-1441.
14. Springer G.S., "A Model of the Curing Process of Epoxy Matrix Composites", in *Progress in Science and Engineering of Composites*, T. Hayashi, K. Kawata, and S. Umekawa Eds., Japan Society of Composite Materials, 1982.
15. Springer G.S., "Resin Flow During the Cure of Fiber Reinforced Composites" *Journal of Composite Materials*, Vol. 16, No. 5, Sept. 1982, pp. 401-410.
16. Loos, A.C., and Springer G.S., "Calculation of Cure Process Variables During Cure of Graphite-Epoxy Composites", in *Composite Materials: Quality Assurance and Processing*, C.E. Browning Ed., ASTM STP 787, 1983.
17. Halpin J.C., Kardos, J.L., and Duduković, M.P., "Processing Science: An Approach for Prepreg Composite Systems", *Pure and Applied Chemistry*, Vol. 55, No. 5, 1983, pp. 893-906.
18. Williams, J.G., Morris, C.E.M., and Ennis, B.C., "Liquid Flow Through Aligned Fiber Beds", *Polymer Engineering and Science*, Vol. 14, No. 6, June 1974, pp. 413-419.
19. Mallow, A.R., Muncaster, F.R., and Campbell, F.C., "Science Based Cure Model for Composites" *Proceedings of the American Society for Composites First Technical Conference*, Dayton, Oct. 7-9, 1986, pp. 171-186.
20. Rajanna, A.V., Nair, N.G., and Subramaniam, R., "Flow of Viscous Fluid Through the Packed Fibres in RTM and RRIM Processes", *Proceedings of the International Conference on Composite Materials and Structures*, Madras India, Jan. 6-9, 1988, pp. 20-28.
21. González-Romero, V.M., and Macosko, C.W., "Design Strategies for Composite Reaction Injection Molding and Resin Transfer Molding" *Society of Plastics Engineers, 44th Annual Technical Conference*, Boston, April 28-May 1, 1986, pp. 1292-1295.
22. Lam, R.C., and Kardos, J.L., "The Permeability of Aligned and Cross-Plied Fiber Beds During Processing of Continuous Fiber Composites", *Proceedings of the American Society for Composites Third Technical Conference, Integrated Composites Technology*, Seattle, Sept. 25-29, 1988, pp. 3-11.

23. Gutowski, T.G., Cai, Z., Bauer, S., Boucher, D., Kingery, J., and Wineman, S., "Consolidation Experiments for Laminate Composites", **Journal of Composite Materials**, Vol. 21, No. 7, July 1987, pp. 650-669.
24. Lee, W.I., Loos A.C., and Springer, G.S., "Heat of Reaction, Degree of Cure, and Viscosity of Hercules 3501-6 Resin", **Journal of Composite Materials**, Vol. 16, No. 6, Nov. 1982, pp. 510-520.
25. Philip, J.R., "Theory of Infiltration", in *Advances in Hydroscience*, Chow, V.T. Ed., Vol. 5, Academic Press, 1969.
26. White, F.M. *Viscous Fluid Flow* McGraw Hill, 1974.
27. Scheidegger, A.E., *The Physics of Flow Through Porous Media, 3rd Edition*, University of Toronto Press, 1974.
28. Loos, A.C., and Springer, G.S., "Curing of Epoxy Matrix Composites" **Journal of Composite Materials**, Vol. 17, No. 2, March 1983, pp. 135-169.
29. Springer, G.S., and Tsai, S.W., "Thermal Conductivities of Unidirectional Materials" **Journal of Composite Materials**, Vol. 1, 1967, pp. 166-173.
30. Loos, A.C. "Curing of Graphite/Epoxy Composites", **Ph.D. Dissertation**, University of Michigan, 1982.
31. ACEE Composites Project Office, compiler, "Standard Tests for Toughened Resin Composites", **NASA RP-1092**, 1983.
32. ACEE Composites Project Office, compiler, "NASA/Aircraft Industry Standard Specification for Graphite Fiber/Toughened Thermoset Resin Composite Material", **NASA RP-1142**, 1985.

**The vita has been removed from  
the scanned document**